

2024-08-12

# Turbulent Combustion Modeling of an Ejector Ramjet Propulsion System

Migadel, Tyson

---

Migadel, T. (2024). Turbulent combustion modeling of an ejector ramjet propulsion system (Master's thesis, University of Calgary, Calgary, Canada). Retrieved from <https://prism.ucalgary.ca>.  
<https://hdl.handle.net/1880/119407>

*Downloaded from PRISM Repository, University of Calgary*

UNIVERSITY OF CALGARY

Turbulent Combustion Modeling of an Ejector Ramjet Propulsion System

by

Tyson Migadel

A THESIS

SUBMITTED TO THE FACULTY OF GRADUATE STUDIES  
IN PARTIAL FULFILMENT OF THE REQUIREMENTS FOR THE  
DEGREE OF MASTER OF SCIENCE

GRADUATE PROGRAM IN MECHANICAL ENGINEERING

CALGARY, ALBERTA

AUGUST, 2024

## Abstract

The Atlantis Intake System (AIS) is a novel design for a ramjet inlet intended to produce thrust through a wide range of flight Mach numbers, including at static conditions, by operating as an ejector-ramjet. A computational fluid dynamics study is performed to assess the change in performance of the AIS due to preheating the fuel jet using heat released from combustion. However, first the computation model is assessed for several combustion-related problems relevant to an ejector ramjet: a one-dimensional laminar flame, a three-dimensional bluff-body stabilized flame, and a ramjet with the AIS operating at static conditions. For an ejector ramjet, preheating the fuel jet is shown to increase the ratio of air to fuel entrained by the AIS and the specific impulse (ISP). Furthermore, if the global equivalence ratio is above unity, preheating the fuel jet while keeping the fuel jet stagnation pressure constant results in an increase in thrust. In contrast, the thrust is lowered as the stagnation temperature of the fuel jet is increased for cases with lean combustion if the stagnation pressure of the fuel is kept constant.

# Preface

Portions of this thesis are based on a previous publication by the author (Migadel et al., 2023).

# Acknowledgements

To my supervisors Dr. Craig Johansen and Dr. Artem Korobenko, as well as my colleague Derek Lastiwka, for your advice and mentorship.

To my partner Mia, whose love and encouragement made this all possible.

And to my friends and family, who provided all the support I could ask for.

# Table of Contents

<b>Abstract</b>	ii
<b>Preface</b>	iii
<b>Acknowledgements</b>	iv
<b>Table of Contents</b>	vi
<b>List of Figures</b>	viii
<b>List of Tables</b>	ix
<b>List of Symbols, Abbreviations, and Nomenclature</b>	x
<b>Epigraph</b>	xiv
<b>1 Introduction</b>	1
<b>2 Literature Review</b>	4
2.1 Previous Investigations of the AIS . . . . .	4
2.2 Previous Study of Ejectors . . . . .	7
2.3 Modelling of Ramjets . . . . .	10
2.3.1 Modelling of Ramjet Combustion with Large-Eddy Simulation . . . . .	12
2.3.2 Modelling of Ramjet Combustion with Reynolds-Averaged Navier Stokes Simulations	13
<b>3 Turbulent Combustion Modeling</b>	16
3.1 Non-Reactive Conservation Equations . . . . .	16
3.2 Extension of Conservation Equations to Reactive Flow . . . . .	17
3.2.1 Mass and Species Conservation . . . . .	18
3.2.2 Momentum Conservation . . . . .	19
3.2.3 Energy Conservation . . . . .	19
3.3 Equation of State and Modelling Fluid Properties . . . . .	20
3.4 Non-dimensional Numbers . . . . .	21
3.5 Cantera Transport Modeling . . . . .	22
3.6 Turbulence Modeling . . . . .	23
3.6.1 RANS Models . . . . .	23
3.6.2 RANS Turbulence Models . . . . .	26
3.7 Chemical Reaction Modeling . . . . .	29
3.7.1 Chemical Reactions and Kinetics . . . . .	30
3.7.2 Turbulence-Chemistry Interaction . . . . .	31
3.7.3 Choice of Combustion Model . . . . .	37
3.8 Chapter Summary . . . . .	38

<b>4 Numerical Model Description</b>	<b>39</b>
4.1 OpenFOAM . . . . .	39
4.2 Discretization . . . . .	40
4.2.1 Temporal Discretization . . . . .	40
4.2.2 Advection Discretization . . . . .	41
4.2.3 Gradient Discretization . . . . .	44
4.2.4 Laplacian Discretization . . . . .	44
4.3 Mesh Sensitivity . . . . .	45
4.4 Chapter Summary . . . . .	46
<b>5 Verification and Validation of Computational Model</b>	<b>47</b>
5.1 One-Dimensional Laminar Flame Speed . . . . .	47
5.2 Bluff-body Stabilized Flame . . . . .	52
5.3 Ejector Ramjet . . . . .	59
5.4 Chapter Summary . . . . .	69
<b>6 Analysis of the Performance Impacts of Preheating the Fuel Jet of an Ejector Ramjet</b>	<b>71</b>
6.1 Changes in Operating Conditions and Performance . . . . .	71
6.2 Chapter Summary . . . . .	76
<b>7 Conclusion</b>	<b>78</b>
<b>References</b>	<b>80</b>
<b>A Mesh Sensitivity Study Uncertainty Plots for the Bluff-body Stabilized Flame Validation Case</b>	<b>91</b>
<b>B Plots Along Centerline of the Ejector Ramjet</b>	<b>95</b>
<b>C Mass Flow Rates of Methane and Air for an Ejector Ramjet at Various Operating Conditions</b>	<b>98</b>

# List of Figures

1.1	Schematic of a ramjet with the Atlantic Intake System (AIS) . . . . .	2
2.1	Schematic of a steam ejector. . . . .	7
2.2	Schematic of research ONERA ramjet. . . . .	11
2.3	Schematic of dual-mode ramjet/scramjet with experimentally observed flame-stabilization locations. . . . .	12
2.4	Mean temperature fields of the PaSR combustion model with and without extinction compared to experimental results. . . . .	14
4.1	Schematic of finite volume cell for computation of fluxes. . . . .	42
5.1	Predictions of reactingPimpleCentralFOAM for methane-air laminar burning velocity for various cell resolution and equivalence ratios with the Z42 reaction mechanism. . . . .	50
5.2	Predictions of reactingPimpleCentralFOAM for methane-air laminar burning velocity with different reaction mechanisms compared to experimental data and Cantera. . . . .	51
5.3	Predictions of reactingPimpleCentralFOAM for propane-air laminar burning velocity with different reaction mechanisms compared to experimental data and Cantera. . . . .	51
5.4	Schematic of the validation apparatus with domain and boundary conditions for CFD analysis. . . . .	53
5.5	Mesh 1 used in the Bluff-body Stabilized Flame Validation Case. . . . .	55
5.6	Time-averaged axial-velocity profiles. . . . .	56
5.7	Time-averaged transverse-velocity profiles. . . . .	57
5.8	Time-averaged axial RMS velocity profiles. . . . .	57
5.9	Time-averaged transverse RMS velocity profiles. . . . .	58
5.10	Time-averaged temperature profiles. . . . .	59
5.11	Schematic of AIS ejector ramjet. . . . .	60
5.12	Domain and boundary conditions for the AIS validation case. . . . .	60
5.13	Mesh 1 used in AIS Validation Case. . . . .	62
5.14	Averaged temperature, pressure, velocity magnitude, and progress variable in the combustion chamber for 200, 400, and 900 kPa fuel jet stagnation pressures. . . . .	65
5.15	Averaged temperature, pressure, velocity magnitude, and progress variable in the combustion chamber for 200 and 400 kPa fuel jet stagnation pressures obtained using the PaSR combustion model with a modified chemical timescale. . . . .	66
5.16	Engine pressure ratio along the length of the AIS ejector ramjet. . . . .	68
5.17	Recirculation zone in the combustion chamber for (a) 400 and (b) 900 kPa jet stagnation pressures. . . . .	69
6.1	Domain and boundary conditions for the AIS when a fraction of the heat from combustion is used to preheat the fuel jet. . . . .	73
6.2	Averaged temperature, pressure, velocity magnitude, and progress variable in the combustion chamber when the fuel jet was heated with a fraction of the heat released during combustion. . . . .	75
A.1	Time-averaged axial-velocity profiles for various meshes and the resulting extrapolated profile. The velocities have been normalized by the free-stream velocity of 17.3 m/s. . . . .	91
A.2	Time-averaged axial-velocity profiles for Mesh 3 with corresponding uncertainty. . . . .	92

A.3	Time-averaged axial-velocity profiles for Mesh 4 with corresponding uncertainty. . . . .	92
A.4	Time-averaged temperature profiles for various meshes and the resulting extrapolated profile. . . . .	93
A.5	Time-averaged temperature profiles for Mesh 3 with corresponding uncertainty. . . . .	93
A.6	Time-averaged temperature profiles for Mesh 4 with corresponding uncertainty. . . . .	94
B.1	Average temperature along centerline of the ejector ramjet for various jet stagnation temperatures and pressures. . . . .	96
B.2	Average pressure along centerline of the ejector ramjet for various jet stagnation temperatures and pressures. . . . .	96
B.3	Average axial velocity along centerline of the ejector ramjet for various jet stagnation temperatures and pressures. . . . .	97
B.4	Average progress variable along centerline of the ejector ramjet for various jet stagnation temperatures and pressures. . . . .	97

# List of Tables

3.1	k- $\omega$ SST Model Coefficients . . . . .	29
5.1	Chemical reaction mechanisms used in current work. . . . .	48
5.2	CFD results for thrust and entrainment for all meshes used in the AIS Mesh Sensitivity Study . . . . .	63
5.3	Extrapolation method, extrapolated value, and resulting uncertainty for thrust and entrainment. . . . .	63
5.4	Comparison of reactingPimpleCentralFOAM results obtained with the default PaSR chemical timescale available in OpenFOAM and a modified chemical timescale from Akerblom (2022) to experiment (Long, 2024) for various jet stagnation pressures. . . . .	68
6.1	Comparison of global equivalence ratio ( $\phi$ ), entrainment ratio ( $\omega$ ), AIS thrust ( $F_{AIS}$ ), total thrust ( $F$ ), ISP, and combustion efficiency ( $\eta_c$ ) for an ejector ramjet when some of the heat from combustion is used to preheat the fuel jet . . . . .	74
C.1	Comparison of global equivalence ratio ( $\phi$ ), mass flow of methane ( $\dot{m}_{jet}$ ), mass flow of air ( $\dot{m}_{air}$ ), and entrainment ratio ( $\omega$ ) for an ejector ramjet when some of the heat from combustion is used to preheat the fuel jet . . . . .	98

# List of Symbols, Abbreviations, and Nomenclature

Symbol	Definition
$A_r$	Arrhenius pre-exponential factor
$A_s$	Sutherland law constant
$B$	CFD Boundary
$c$	Molar concentration, Speed of sound
$C_p$	Specific heat capacity at constant pressure
$C_v$	Specific heat capacity at constant volume
$\mathbf{d}$	Vector connecting adjacent cell centers
$D$	Mass diffusivity, diameter
$e$	Internal energy
$E$	Total energy
$E_a^r$	Activation energy
$()_f$	Value at cell face
$f$	Body force
$F$	Surface force, total engine thrust
$F_{AIS}$	Thrust of the AIS
$h_{k,f}$	Heat of formation of species $k$
$h_{s,k}$	Specific sensible enthalpy of species $k$
$h_t$	Specific total enthalpy
$H$	Height
$k^f$	Forward reaction coefficient
$k^b$	Backward reaction coefficient

$k$	Turbulent kinetic energy
$L$	Length in axial direction
$Le$	Lewis number
$\dot{m}$	Mass flow rate
$M$	Molar mass
$N_k$	Number of modelled species
$N_r$	Number of modelled reactions
$p$	Observed order of convergence
$P$	Pressure
$Pr$	Prandtl number
$q$	Heat flux
$q_r$	Overall heat release from chemical reaction
$Q_H$	Energy source term
$r$	Gradient ratio for flux limiter
$R$	Gas constant
$S$	Sources or sinks
<b>S</b>	Cell face normal vector
$S_{k,arr}$	Laminar reaction rate for species k
$S_{B,i}$	Body force in i-th direction
$S_k$	Mass source term from chemical reaction for species $k$
$S_{k,r}$	Mass source term from chemical reaction for species $k$ for reaction r
$S_L$	Laminar flame speed
$S_T$	Energy source term from chemical reaction
$S_r$	Overall molar reaction rate for reaction $r$
$S_c$	Schmidt number
$t$	Time
$T$	Temperature
$T_s$	Sutherland law reference temperature
$u'$	Turbulent velocity fluctuation
$u$	Velocity
<b>U</b>	Velocity vector
$U_\psi$	Uncertainty of CFD result on flow parameter $\psi$

$V$	Mass diffusion velocity, Volumetric flow rate
$V_c$	Mass diffusion velocity correction
$V^*$	Estimated mass diffusion velocity
$v'$	Stoichiometric coefficient for reactant species
$v''$	Stoichiometric coefficient for product species
$W$	Width
$x$	Axial coordinate
$X$	Molar fraction
$y$	Transverse or radial coordinate
$Y$	Mass fraction
$\alpha$	Thermal diffusivity
$\beta_r$	Arrhenius temperature coefficient
$\delta$	Discretization error
$\Delta h_g$	Average mesh cell size
$\epsilon$	Turbulence dissipation
$\eta_c$	Combustion efficiency
$\gamma$	Ratio of specific heats
$\kappa$	Switching parameter, Partially Stirred Reactor parameter
$\lambda$	Thermal conductivity
$\mu$	Dynamic viscosity
$\mu_t$	Turbulent dynamic viscosity
$\nu$	Kinematic viscosity
$\nu_{eff}$	Sum of turbulent and laminar/molecular kinematic viscosities
$\omega$	Specific turbulence dissipation, entrainment ratio
$\Omega$	Volume
$\psi$	Arbitrary flow property
$\psi_0$	Extrapolated value for grid independence
$\phi$	Equivalence ratio
$\rho$	Density
$\tau_{ij}$	Shear stress tensor
$\tau_c$	Chemical time scale for Partially Stirred Reactor model
$\tau_m$	Mixing time scale for Partially Stirred Reactor model

$\theta$	Flux limiter, Combustion progress variable
$\zeta$	Non-dimensional temperature
$()_0$	Stagnation (or total) value
$()_k$	Value for species $k$
$()_{HX}$	Relaxing to the heat exchanger
$()_r$	Value for reaction $r$
$()_\infty$	Far-field value
$()^{mix}$	Mixture averaged property
$< \phi >$	Average of $\phi$
$ \phi $	Magnitude of $\phi$

# Epigraph

*All models are wrong, but some are useful.*

- George Box

# Chapter 1

## Introduction

Since the Second World War high-speed flight has been a key interest for many industries and researchers, with applications in long-range passenger transport, reusable launch vehicles for space applications, and long-range missiles (Berglund and Fureby, 2007). Of particular interest are air-breathing engines, which offer substantially higher specific impulse than rocket engines. One air-breathing engine capable of supersonic flight is the ramjet, which uses fixed engine components to decelerate and compress incoming air by the ram effect (Fry, 2004). First, the incoming air enters the inlet and diffuser, which provide natural compression. The resulting compression depends on the Mach number and fluid properties and increases dramatically with vehicle speed. Consequently, without modifications to the engine or cycle, a ramjet is unable to produce appreciable thrust at low Mach numbers (Sziroczak and Smith, 2016). Therefore, a typical ramjet requires a secondary propulsion system to accelerate the vehicle to an appropriate high speed, approximately Mach 3, to provide sufficient compression of the incoming air (Berglund et al., 2010). Above Mach 5, this deceleration results in substantial losses and therefore a typical ramjet has an operational range of between Mach 3 and 5.

Existing technologies aimed at extending ramjet operation to low Mach numbers include combined-cycle engines such as the rocket-based combined cycle (RBCC) and the turbine-based combined cycle (TBCC) (Fry, 2004; Sziroczak and Smith, 2016). These propulsion systems capitalize on the performance benefits of various types of engines at different flight Mach numbers (Marshall et al., 2004). However, major challenges for combined-cycle air-breathing engines exist, including the complex design integration required between the airframe and multiple propulsion systems while minimizing drag (Kors, 1991; Daines and Segal, 1998). Additionally, their design is further complicated by the need to consider the flow path for multiple modes of operation. To avoid the complexity of integrated propulsion systems, the University of Calgary in partnership

with Atlantis Research Labs Inc. (ARL) is developing the Atlantis Intake System (AIS), with the aim of enhancing the ramjet cycle to allow for the generation of thrust at flight numbers below Mach 3.

A ramjet with the AIS operates as an ejector ramjet (ERJ), which uses a heated fuel-rich high-speed jet to pressurize and entrain ambient air (Fry, 2004). This provides a means of providing the necessary airflow into the engine to operate the engine statically without introducing any additional moving parts. A schematic of a ramjet with the AIS is shown in Fig. 1.1. Note that the fuel is preheated through a heat exchanger in the combustion chamber.

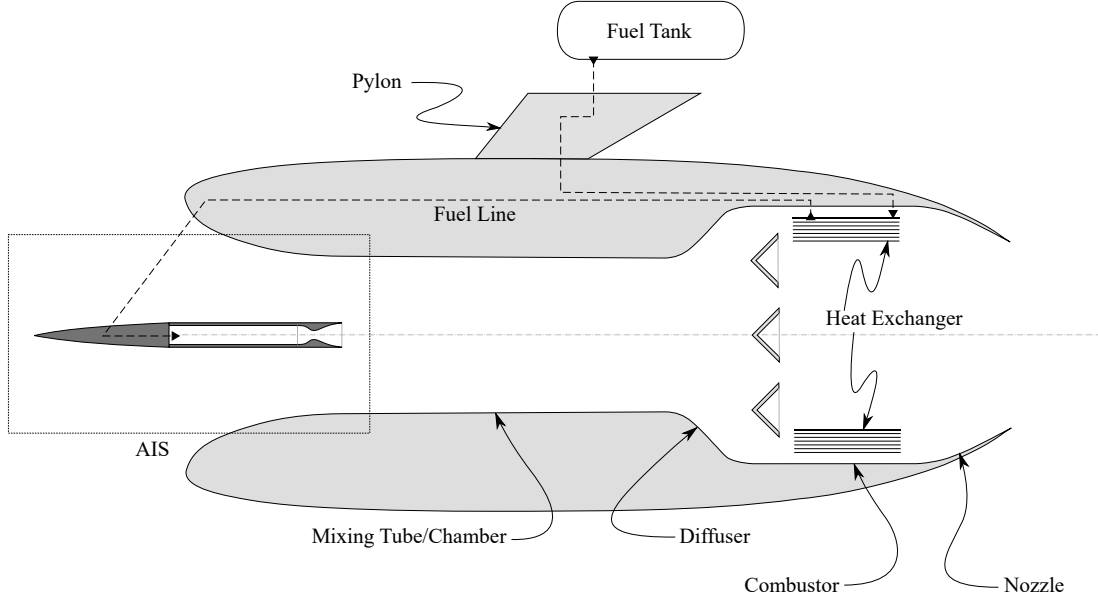


Figure 1.1: Schematic of a ramjet with the Atlantic Intake System (AIS) (Lastiwka et al., 2022). Used with permission.

The AIS ERJ was previously investigated using control-volume (CV) and non-reactive computational fluid dynamics (CFD) simulation tools (Wilson et al., 2015). A simplified ramjet cycle combined with a heat exchanger model was used to close the problem and provide predictions of specific impulse curves over a range of flight Mach numbers. While the investigation provided valuable insight into overall AIS ERJ performance and showed that the CV analysis could accurately capture the tradeoff between entrainment and flow compression, little could be learned about the combustion process. For example, it is unknown how the AIS interface with the combustor affects flame holding, combustion efficiency, pressure losses, thrust levels, and fuel consumption. As a result, there is a clear need for turbulent combustion simulations of AIS ERJ to advance the technology further.

Modeling turbulent combustion for ramjet/scramjet flows has many challenges. Not only must compress-

iblity and turbulence be accurately modeled, chemical reactions, heat release and the interactions between them must be captured (Poinsot et al., 1995). These equations are coupled since the temperature field is controlled by the progress of the chemical reactions. Furthermore, the transport properties and thermodynamic variables depend on temperature and therefore also depend on the chemical reactions taking place.

As available computing power has increased over the past several decades, CFD has seen an increase in use both in industry and in academic research. Consequently, there is a large number of CFD solvers available. These solvers have a large range in scope and applicability, from small in-house academic codes to large commercial software which focuses on robustness and being user-friendly. Generally, open-source CFD solvers are academic and are not widely used. However, one notable exception is OpenFOAM (Weller et al., 1998), which due to significant developer investment offers a wide range of applicability while being more user-friendly than other open-source codes. This code provides researchers and industry users comparable capability to available commercial codes, while not incurring the substantial licensing costs. Furthermore, they have the option to modify or add to the source-code, which offers users the ability to adapt the solvers to a particular application if needed.

The research objectives of this work are as follows: (1) assess the accuracy of OpenFOAM for investigating ERJ concepts, (2) provide the first high-fidelity predictions of engine thrust for an AIS-ERJ, (3) determine the effect of the AIS/combustor interface on fuel-air mixing and combustion efficiency, and (4) assess the effect of fuel preheat on engine performance. To achieve the first objective, the third-party OpenFOAM solver, reactingPimpleCentralFOAM (Kraposhin et al., 2015, 2018), will be assessed using several cases, including a benchmark flame holding turbulent combustion case from the literature. The remaining objectives will be achieved by using reactingPimpleCentralFOAM to investigate an AIS-ERJ over a wide range of conditions, including various preheat levels.

To begin, Chapter 2 will provide a literature review of the previous analyses of the AIS. Additionally, a review of the application of CFD for ejectors and ramjets is included. For the ramjet flows, the focus was on models which included combustion. Following this, a description of the governing equations and discretization schemes is presented in Chapters 3 and 4, respectively. Next, Chapter 5 presents the results of the validation study for the computational model. Lastly, the performance impacts of preheating the fuel jet for the AIS is described in Chapter 6.

# Chapter 2

## Literature Review

A literature review of the main topics of the present work are discussed below. First, an overview of previous work analyzing the AIS using both computational and experimental approaches is provided. Following this, some results in literature for flows relevant to the AIS with a focus on those obtained using CFD are discussed. The relevant flows include ejectors, which feature the jet and entrainment aspects of the AIS, and ramjets which feature the simulation of combustion and the analysis of the performance of an aerospace engine.

### 2.1 Previous Investigations of the AIS

The design of the AIS was based on the Gluhareff pressure jet engine which was developed by Eugene M. Gluhareff for tip propulsion on rotary wing aircraft (Barrett and Gluhareff, 2008). In the original design, pressurized liquid propane would enter the heating coils and be vaporized in the combustion chamber. The preheated fuel would then be ejected through the fuel nozzle, which leads to the entrainment of surrounding air into the engine. The fuel and air mix and then burn in the combustion chamber. Therefore, this engine can be analyzed as a ramjet where the kinetic energy source is the pressurized fuel, rather than the freestream air entering the engine inlet on a moving vehicle. Performance studies of the Gluhareff pressure jet engine have been conducted and show that these engines are capable of generating static thrust (Barrett and Gluhareff, 2008). However, one important note is that the Gluhareff engine is a pulse jet which is different than the continuously operating ramjet engine studied in this work.

As discussed in Chapter 1, the AIS operates as an ejector ramjet in which a high-speed fluid jet (the fuel jet) entrains and pressurizes a secondary fluid stream (the surrounding air). The performance of the AIS was previously investigated using a control-volume approach by Wilson et al. (2015) for a specific design of the AIS proposed by ARL. This analysis included an optimal amount of heat from combustion to preheat

the fuel jet. To determine the performance of the AIS, the properties of the products exiting the AIS (which then enter the diffuser) were determined from the properties of the fuel jet and the surroundings based on an assumed amount of entrainment. Note that entrainment is defined as the ratio of the mass flow rate of the secondary flow (from the surrounding air) to that of the primary flow (the fuel). With the properties at the diffuser known, the overall engine performance was then predicted using an ideal jet-propulsion cycle. The results from this analysis were compared to simplified CFD simulations and a reasonable agreement between analytical and simulation results was obtained. However, as noted in Chapter 1, the CFD analysis only included the intake system and therefore did not include combustion. With no forward velocity of the ramjet the expected specific impulse ( $I_{sp}$ ) was found to be 600s when methane was used as the fuel and 400s when propane was used.

Additional work by Wilson (2017) determined a method for predicting the entrainment of air into the AIS again using a control volume approach. This method required only the properties of the fuel jet and the surroundings. To accomplish this, it was assumed that the static pressure at the exit of the mixture is equal to the ambient pressure of the surrounding air. This approach was the same as one made by Whitley et al. (1996), which allowed for the accurate prediction of the entrainment for a thrust-augmenting ejector. Through comparison to CFD results, Wilson (2017) found that this assumption was valid for one operating condition of the engine, where the static pressure at the exit of the AIS was reasonably close to the ambient pressure. Additionally, it was found through a comparison of the predicted air-to-fuel mass flow rates that the control-volume based method of predicting entrainment agreed reasonably well with CFD results.

Additionally, Wilson (2017) quantified the various losses present in the AIS by analyzing the sources of exergy destruction. It was found that the action of viscosity, heat transfer, and the diffusion of species all contributed significantly to exergy destruction. However, when normalized by the thrust power, the rates of exergy destruction tended to decrease with increasing jet Mach number and increasing stagnation temperature of the fuel jet. This indicates that an increase in the jet stagnation temperature (accomplished by using some the heat from combustion to heat the jet) could lead to reduced engine losses and an improved overall engine performance. This is further supported by a parametric study of various engine operating conditions conducted in the same work by Wilson (2017), which showed that the specific impulse increases with increasing jet stagnation temperature, however a local maxima was found in regards to the jet stagnation pressure. Overall, increasing the jet stagnation temperature was found to increase entrainment, increase specific impulse, and decrease normalized values for exergy destruction.

Lastiwka et al. (2022) continued the analysis of the AIS by developing a one-dimensional ejector ramjet (1D-ERAM) code to aid in design optimization. The 1D-ERAM code models the entrainment and pressurization through the AIS. Additionally, it includes models for combustion and the exhaust nozzle, which

allows for the prediction of the overall engine performance. The code was verified against CFD results for a compressible confined jet and the predicted entrainment was found to agree reasonably well when entrance losses were accounted for in the 1D-ERAM code. Additionally, the predicted pressure ratio (the ratio of pressure in the mixing tube to the ambient air) and entrainment was shown to agree well with experimental results obtained by Kramer et al. (2022) for a compressible confined jet case with variable mixing tube diameter and back pressure. Given the observed agreement between the 1D-ERAM code and experimental and CFD results, it is a valuable tool in the development and optimization of the AIS (Lastiwka et al., 2022). Since each 1D-ERAM case only requires 1 to 5 minutes of run-time, it is capable of iterating over many designs very quickly compared to CFD and experimental approaches.

In addition to the analytical and computational analyses discussed previously, preliminary experimental results for the AIS have been obtained by Long et al. (2022) for a non-optimized ejector. Both flows with and without combustion were studied at static conditions. The goal of the tests without combustion was to determine an appropriate design of the AIS which would remain within the flammability limits of the fuel used, which was methane for these tests. Modular 3D-printed components were used which allowed for an inexpensive method to assess multiple engine designs. With an appropriate engine geometry selected, it was then manufactured using mild steel for the subsequent combustion tests. ‘Blow-down’ style experiments were used for combustion cases in which the fuel jet’s run tank was filled to a higher stagnation pressure and was then allowed to decrease in pressure as the test progressed. Additionally, no preheating of the fuel jet using heat from combustion was implemented. It was found that combustion successfully occurred for fuel-jet stagnation pressures below 775 kPa, but was only stable when below 625 kPa. For the flows with fuel-jet stagnation pressures above 775 kPa, for which combustion did not occur, the entrainment resulted in a flow that was still globally within the flammability limits of methane. This suggests there may be insufficient flame holding or the local air to fuel ratio at the ignition source may be outside of the flammability limits (Long et al., 2022). The peak specific impulse was observed to be 200s when a jet stagnation pressure of 580 kPa was used.

To quantify the various losses of the AIS and ejector ramjet, as well as develop a means to evaluate the overall efficiency, Lastiwka et al. (2023) introduced a real and ideal thermodynamic process for a ramjet with an ejector-based inlet. Both of these cycles were compared to CFD as a means of verification and with reasonable accuracy were able to predict the final state of the ejector-ramjet process. Through the analysis of the non-ideal cycle, the entrainment process was found to be the largest source of entropy in the system. Furthermore, using the 1D-ERAM code discussed previously (Lastiwka et al., 2022), Lastiwka et al. (2023) conducted a performance analysis of the AIS ERAM inlet and found two distinct operating regions: one where the entrainment ratio varies with the mixing tube diameter and the other where it varies with the

orifice diameter ratio. These were referred to as the diffuser- and orifice-loss dominated regions, respectively. Additionally, a line of operating conditions which resulted in the largest entrainment was identified. From this performance and thermodynamic analysis, Lastiwka et al. (2023) concluded that when operating in the diffuser-loss region, the AIS total pressure ratio was high, the isentropic efficiency was largest, and a reduction in the entrainment ratio coincided with an increase in the total pressure ratio. In contrast, if operating in the orifice loss dominated region, the AIS total pressure ratio, entrainment ratio, and isentropic efficiency were all low indicating overall poor performance.

## 2.2 Previous Study of Ejectors

The ejector was invented in the 1901 by Sir Charles Parsons and saw wide usage in air-conditioning of large buildings in the 1930s (Chunnanond and Aphornratana, 2004*a*). They are commonly used in refrigeration systems to either recover the work dissipated in the throttling process to improve system efficiency or to replace the mechanical compressor (Tashtoush et al., 2019). The efficiency of a refrigeration system is often quantified through a measure known as the Coefficient of Performance (COP), which is the ratio of heat out of the cold reservoir to the work put into the system. A schematic of an ejector is shown in Fig. 2.1. It consists of two intake ports for the primary and secondary streams which flow into a common discharge or outlet port. The secondary stream is entrained by the high-speed expanded primary fluid as it exits the converging-diverging nozzle. Both streams are then mixed and then enter the diffuser.

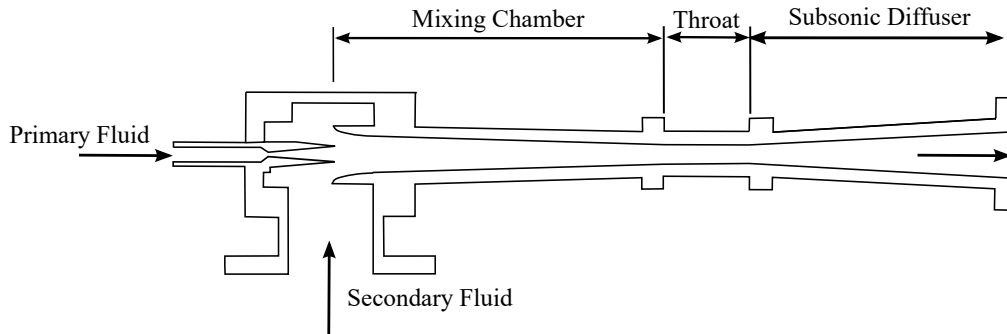


Figure 2.1: Schematic of a steam ejector. Modified from Chunnanond and Aphornratana (2004*a*).

Entrainment is a common metric for the performance of ejectors (Chunnanond and Aphornratana, 2004*a*). It has been found to be a function of the operating conditions as well as the ejector geometry. In addition, its value has been found to be limited by a critical back-pressure, possibly due to the flow choking within the mixing chamber (Munday and Bagster, 1977). The choking is thought to be due the primary fluid

expanding outwards out as it exhausted from the nozzle exit into the mixing chamber, which together with the mixing chamber wall essentially forms a converging duct for the secondary flow (Munday and Bagster, 1977; Chunnanond and Aphornratana, 2004a). Along this converging duct, no significant mixing between the primary and secondary streams occurs and the secondary fluid eventually becomes choked. Mixing of the two streams then begins after this process. At back-pressures below this critical back-pressure, the secondary mass flow rate will remain the same, which causes the COP and cooling capacity to remain constant as well. In contrast, as the back-pressure is increased, it will eventually lead to the secondary flow reversing its flow direction (Chunnanond and Aphornratana, 2004a). An ejector can no longer operate in this flow condition.

Through experimental study, Huang et al. (1985) investigated an ejector's performance characteristics in the context of a design analysis of jet refrigeration systems. The performance of an ejector was found to be heavily dependent on the choking phenomena of the secondary stream. This choking leads to an 'effective area', defined as the area of the secondary flow where it reaches sonic velocity. This effective area was found to vary significantly with operating conditions. Additionally, from their experimental data, Huang et al. (1985) constructed an ejector performance map which enabled a design analysis of jet refrigeration systems.

The performance of an ejector refrigeration system was additionally studied by Chunnanond and Aphornratana (2004b) experimentally. In particular, they examined the influences of the geometry, operating conditions, and the effects of the temperature of the primary fluid. It was observed that using a smaller nozzle and moving the nozzle further outside the mixing chamber reduced the angle of the expansion wave of the oblique shock as the fluid exits the primary nozzle. This allowed larger amounts of secondary fluid to be entrained leading to a higher COP and cooling capacity of the refrigerator. However, higher entrainment was found to result in a lower momentum of the resulting mixed fluid, leading to a lower critical back-pressure. As previously discussed, in order to maintain a high COP and prevent flow reversal the back-pressure must be below this critical value, therefore this could cause difficulties in overall system design by limiting the system's operating pressure.

In addition, Chunnanond and Aphornratana's (2004b) experimental study found that increasing the temperature of the primary fluid led to higher COP values and a higher cooling capacity of the system. This was thought to be due to the lower mass flow rate of primary fluid causing a smaller expansion angle as the fluid exits the primary nozzle. This smaller expansion angle leads to a larger converging duct for the secondary fluid, leading to an increase in entrainment. This larger amount of secondary mass flow rate allows for a higher cooling capacity of the system and a larger COP. However, this again led to lower critical back-pressures.

In addition to experimental investigations, ejectors have been studied analytically. Huang et al. (1999) conducted a 1-D analysis for the prediction of ejector performance at critical-mode (or choked) operation.

This analysis assumed constant-pressure mixing to occur inside a constant-area section of the ejector. However, empirical coefficients were needed to account for various losses in the ejector. These coefficients were determined by matching the analytical predictions to experimental data collected for 11 ejectors in the same work by Huang et al. (1999). They depend on the ejector's design and manufacturing and are functions of system properties such as surface polishing, center-line alignment, the material used, and so on. Therefore, a major challenge when using this analytical approach to assess new ejector designs is the possible need to modify these coefficients to provide accurate results.

One-dimensional analysis and other theoretical approaches are often inadequate when further details of the flow are required (Rusly et al., 2005). Another approach uses CFD, which allows for the prediction of data that is often not available from analytical methods or is difficult to collect experimentally. Sriveerakul et al. (2007) compared results from CFD to experimental data. It was found that the static pressure profiles agreed reasonably well between CFD and experiment. Conversely, the entrainment ratio was found to be under-predicted in operating conditions which resulted in unchoked secondary flow, with differences up to approximately 50%. However, the predicted entrainment ratio agreed better with experiment for operating conditions which resulted in choked flow with a maximum error of approximately 20%. Rusly et al. (2005) also compared the predicted entrainment ratio from CFD to experiment for choked secondary flows but saw better agreement, with the largest difference from experiment being approximately 10%. Additionally, Rusly et al. (2005) used a 1-D model from Huang et al. (1999) to predict the entrainment ratio to compare to the CFD and experimental results. It was found that the CFD model better matched experiment in 10 out of the 13 cases tested. CFD can therefore be a promising method to analyze ejectors and predict performance. Following their comparison of the 1-D, CFD, and experimental results, Rusly et al. (2005) used CFD to determine that the maximum entrainment ratio occurs when the pressure ratio between the ejector primary inlet and the diffuser outlet is just sufficient to choke the secondary flow but avoid a shock in the diffuser. Additionally, the placement of the nozzle was found to affect the overall performance of the ejector.

A major challenge in using CFD is the selection of an appropriate turbulence model. The results for simulating ejectors has been shown to be sensitive to the turbulence model used, highlighting its importance (Mazzelli et al., 2015). Besagni and Inzoli (2017) compared the effects of seven RANS turbulence models, namely the Spalart-Allmaras,  $k - \epsilon$  Standard,  $k - \epsilon$  RNG,  $k - \epsilon$  Realizable,  $k - \omega$  SST, and the RSM models. Additionally, the effects of different near-wall modeling options were assessed. Overall, the  $k - \omega$  SST model showed better agreement with experiment in regards to the entrainment ratio, the shock wave position, the pressure recovery, and the wall static pressure values compared to other RANS turbulence models. Similar results were obtained by Mazzelli et al. (2015), who found that the  $k - \omega$  SST model predicted global parameters, such as the entrainment ratio and inlet mass flow rate, more accurately than the  $k - \epsilon$  Standard,

$k - \epsilon$  RNG, and RSM turbulence models. However, it was noted that at low motive/primary fluid pressures the  $\epsilon$ -based models performed better. Additionally, the RSM model predicted results similar to the  $k - \omega$  SST model, but had a much larger computational cost and suffered from numerical stiffness and convergence issues.

Through analysis using CFD, Bartosiewicz et al. (2006) assessed shock boundary-layer interaction in an ejector. It was observed that strong shocks occurring at the secondary nozzle could significantly decrease the mixing rate and possibly even lead to flow reversal. CFD has also been used to model the condensation of the refrigerant as it is expanded through the primary nozzle and mixing chamber (Biferi et al., 2016). This expansion can alter both the pressure and Mach profiles in the ejector. When this condensation was accounted for in the CFD analysis, it was found that the mass flow rate of the primary fluid was predicted within 5% of the experimental value.

Of particular importance in the study of ejectors is predicting their efficiency. With known efficiencies the sources of primary losses can be determined allowing for system optimization. Varga et al. (2009) assessed the nozzle, mixing, and diffuser efficiencies from their principal definitions using CFD. The primary nozzle and diffuser efficiencies were calculated by comparing their simulated enthalpies to the enthalpies calculated from their corresponding isentropic processes, while the mixing efficiency was calculated using various definitions available in literature. It was found that the nozzle efficiency was independent of the operating conditions and varied only slightly with the nozzle throat diameter. Conversely, the diffuser efficiency was found to be a function of the back pressure with higher back pressures resulting in a higher diffuser efficiency. The mixing efficiencies showed large variation depending on the definition used, but in general the efficiency increased slightly with increasing back pressure until the back pressure reached its critical value. Beyond this pressure the mixing efficiency decreased substantially.

A more comprehensive literature review on ejectors including their applications in refrigeration is provided by Chunnanond et al. (2004a). Furthermore, Tashtoush et al. (2019) provides an overview of ejector research with a focus on several topics, namely: the effect of different geometrical aspects affecting ejector performance, the attempts made to develop a mathematical/computational model to investigate ejectors, and lastly the main ejector refrigeration systems proposed so far.

## 2.3 Modelling of Ramjets

One challenge of developing ramjets is a lack of adequate available experimental data (Pichon and Laverdant, 2016). Experiments are critical in the validation and improvement of CFD and other numerical tools. To remedy this, a ramjet was developed at the French Aerospace Lab (ONERA) with the goal of providing data

for CFD code validation (Ristori et al., 2012; Pichon and Laverdant, 2016). The apparatus (see Fig. 2.2) can be operated as a Liquid-Fueled Ramjet (LFRJ) by injecting liquid fuel into both inlets. Both Reynolds Averaged Navier-Stokes (RANS) and Large Eddy Simulations (LES) computations have been applied to analyze the ONERA research ramjet. The primary results of these studies is discussed in Sections 2.3.2 and 2.3.1, respectively.

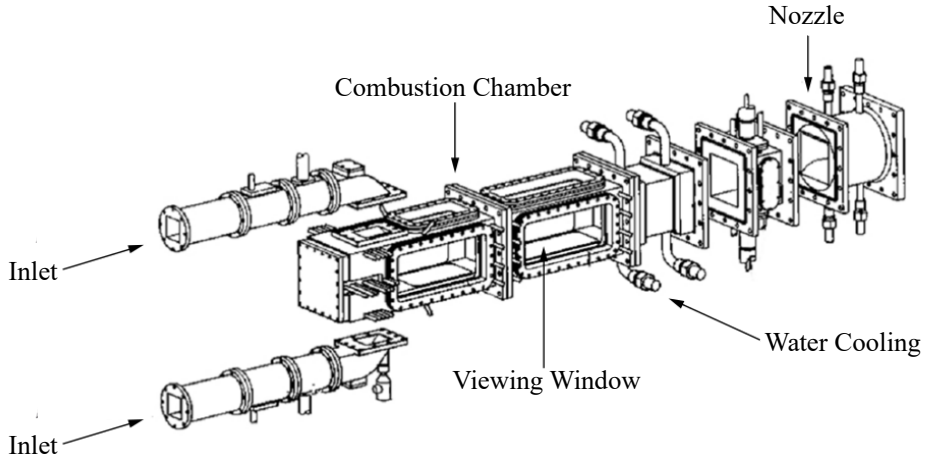


Figure 2.2: Schematic of research ONERA ramjet. Modified from (Pichon and Laverdant, 2016).

In addition to the ONERA ramjet, Micka and Driscoll (2008) studied a dual-mode scramjet/ramjet with a cavity flameholder experimentally. This engine, shown schematically in Fig. 2.3, consists of a Mach 2.2 nozzle followed by a constant area isolator. This isolator extends up to the leading edge of the rectangular-cavity flameholder and would contain a shock-train which decelerates the flow to subsonic velocities before combustion occurs when operating as a ramjet. Following the rear-edge of the flameholder is the diverging section and exhaust. Hydrogen and a hydrogen–ethylene blend were used as the fuel. While operating as a ramjet, two distinct combustion stabilization locations were found. For the first case, described as ‘cavity stabilized combustion’, the flame base is located in the upstream part of the cavity shear layer and is mostly steady. The second case (‘wake stabilized combustion’) was stabilized upstream of the cavity in the wake of the fuel injection jet and was found to be highly unsteady. Both flame stabilization locations are shown schematically in Fig. 2.3. Qualitative comparisons between these experimental observations and CFD results is discussed in Sections 2.3.1 and 2.3.2.

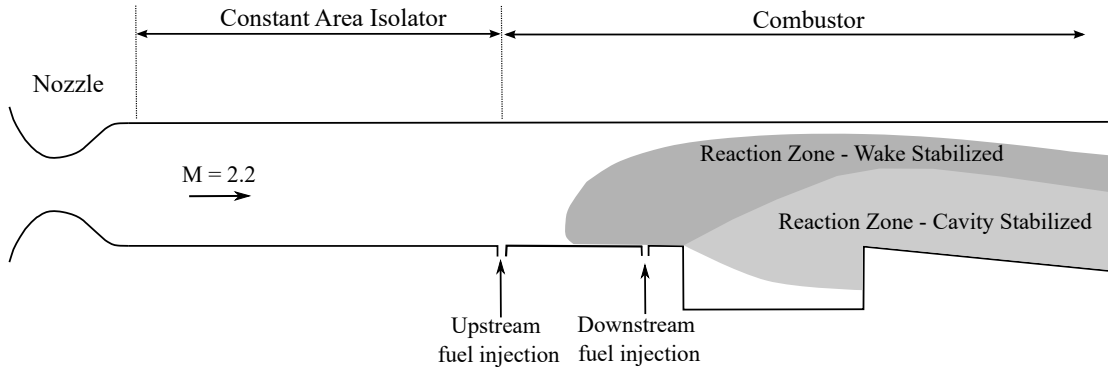


Figure 2.3: Schematic of dual-mode ramjet/scramjet with experimentally observed flame-stabilization locations. Modified from (Micka and Driscoll, 2009).

### 2.3.1 Modelling of Ramjet Combustion with Large-Eddy Simulation

LES has been shown to be more accurate than RANS simulations in predicting mean velocity and fuel concentration profiles in the recirculation zones, as well as the size of these zones (Pichon and Laverdant, 2016). However, due to the need for LES to resolve a significant portion of the turbulent energy, it has a significantly larger computational cost than RANS. Roux et al. (2008) used two LES codes, AVBP and CEDRE, to analyze the predicted mean flow topology and instantaneous results for the ONERA research ramjet. Even though the codes differed significantly in their treatment of combustion and sub-grid mixing, both results matched experimental mean velocity profiles reasonably well. However, there was disagreement in the positions for which combustion occurred. CEDRE predicted combustion near the front of the combustion chamber, which was not observed in experiment or with AVBP. This difference was likely due to the combustion model used. AVBP utilizes the dynamically-thickened flame model, which is able to account for the decrease in laminar flame speed at higher equivalence ratios (Roux et al., 2008). In comparison, the CEDRE code used a ‘transported partially-stirred reactor’ approach model with a global chemical mechanism which allowed for combustion at unrealistically large equivalence ratios.

Another area of ramjet combustion research utilizing LES is the prediction of combustion instabilities. Roux et al. (2010) used LES to study the effect of the chemical mechanism on the observed combustion instabilities. In particular, the authors analyzed the effect on the combustion instabilities for the ONERA research ramjet when a modified one-step chemical mechanism was used compared to the standard one-step mechanism. The standard scheme was an unadjusted mechanism while the other was fitted to better match the laminar flame speed over a wide range of equivalence ratios. Both mechanisms showed good agreement when compared to the axial velocity profiles, however only the fitted scheme matched experiment in terms of

unsteady effects. One such effect was the frequency of the oscillations in the combustor. When the standard scheme was used, the combustor was found to exhibit non-physical high frequency self-sustained oscillations. In contrast, a lower, damped frequency was observed for the fitted scheme. In addition to analysis, LES has been used to develop a control strategy to actively control combustion instabilities (Menon, 1992). In this case, in both experiment and with LES, two types of instability were observed: a small-amplitude high-frequency instability and a large-amplitude, low-frequency instability. Both were able to be controlled using acoustic feedback.

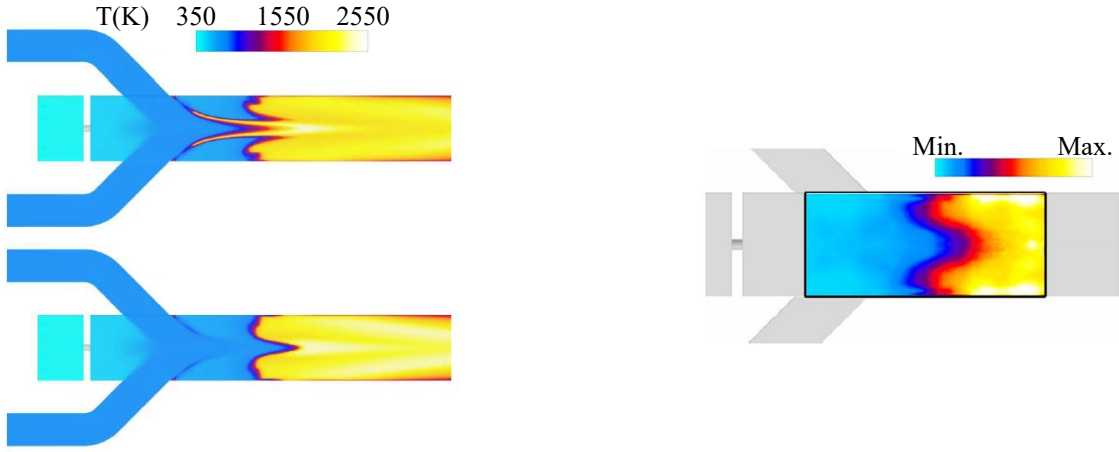
In regards to the simulation of combustion, another area in which LES is a valuable tool is the analysis of mixing. Mixing in the combustion chamber has important effects on the stability and efficiency of a combustor. Reichstadt et al. (2007) studied the ONERA research ramjet without combustion to predict the velocity and fuel concentrations using both RANS and LES methods. It was observed that LES performed significantly better at predicting species profiles. This was likely due to the RANS model not accurately capturing the strength of recirculation vortices in the flow, leading to inaccurate mixing and consequently inaccurate species profiles.

In addition to species profiles, mixing has important ramifications on fuel injection and flame stability. Zetterval and Fureby (2018) used LES to analyze the University of Michigan laboratory dual-mode ramjet/scramjet combustor studied experimentally by Micka and Driscoll (2008). Using the Partially-Stirred Reactor (PaSR) finite-rate chemistry combustion model, the dual-mode ramjet was simulated for stagnation temperatures ranging from 1130 to 1500K. These cases all resulted in subsonic combustion. As previously discussed, experimentally it was observed there were two modes of flame-stabilization, both of which are shown in Fig. 2.3. LES was able to qualitatively match both of these observed flame stabilization mechanisms in the combustion chamber (Zettervall and Fureby, 2018). Additionally, it was found that the ignition delay time of the chosen chemical mechanism played a vital role in accurately predicting flame-stabilization.

### 2.3.2 Modelling of Ramjet Combustion with Reynolds-Averaged Navier Stokes Simulations

Due to turbulence being entirely modelled (compared to LES where the largest eddies are resolved), RANS turbulence modelling has a significantly lower computational cost than LES. However, because it is not able to resolve the large turbulence eddies, RANS is less suitable in describing flows in which large-scale unsteadiness is significant, such as vortex shedding (Pope, 2000). However, when only the overall features and topology of the flow is desired, RANS is often sufficient (Pichon and Laverdant, 2016). One such case is determining the blow-off at fuel-lean conditions, referred to as lean blow-out (LBO) limit. Pichon et al. (2012) used RANS

CFD to determine the LBO of the ONERA ramjet which was found to agree very well with experiment. This was accomplished using the PaSR combustion model integrated into the in-house code CEDRE. To account for flame extinction, a critical residence time was computed for a range of operating conditions. When this residence time became smaller than a typical chemical time scale, extinction occurred. By incorporating this flame extinction criterion, the accuracy of the predicted LBO improved significantly, from an equivalence ratio of 0.25 for the standard PaSR model to 0.30 for the model with extinction (compared to a range of 0.28 to 0.32 from experiment). Fig. 2.4 shows the mean temperature field for both the default PaSR combustion model and the PaSR modified with the extinction model, as well as experimental results for comparison. Clearly, the modified PaSR more accurately captures the overall flow field.



(a) Mean temperature field from RANS, top is with the default PaSR combustion model, bottom is the PaSR model with flame extinction added.

(b) Experimental visualization of OH\* radical emission (arbitrary levels)

Figure 2.4: Mean temperature fields of the PaSR combustion model with and without extinction compared to experimental results. Modified from (Pichon et al., 2012).

Using RANS turbulence modelling, Tuncer (2012) predicted the overall flow-field of the Micka and Driscoll ramjet. This was accomplished using Mentors  $k - \omega$  shear-stress transport model with detailed chemical kinetics. The flame was found to be cavity-stabilized (see Fig. 2.3) when the Mach number was 3.3 with a stagnation temperature of 702 K. However, to anchor the flame, additional fuel injection at the rear-wall of the cavity was required. This agrees with experimental observations (Micka and Driscoll, 2009). Other main features of the flow, such as a bow shock upstream of the cavity and a expansion shock at the cavity trailing edge were captured and reasonably matched experiment.

A major overall goal of CFD analysis is to aid in the design process. This is also true for ramjets and other high-speed engines. Ma et al. (2020) used theoretical analysis as well as CFD simulations to study

the thrust performance of shock-induced combustion ramjet engines (shcramjets). A shcramjet differs from a conventional ramjet in that the reactants are heated from oblique shocks and therefore no ignition source is needed. Using the  $k - \omega$  SST RANS turbulence model with a detailed chemical mechanism, CFD results were first validated with measurements from ground-based testing of the HyShot II scramjet in the High Enthalpy Shock Tunnel Göttingen of the German Aerospace Center (Hannemann et al., 2010). It was found that the CFD results reasonably matched experiment. The CFD model as well as results from theoretical analysis were then used to assess the performance of a simplified design for a shcramjet (Ma et al., 2020).

CFD has also been utilized in the preliminary design of a dual-mode scramjet/ramjet. These engines have the potential to provide air-breathing propulsion up to hypersonic Mach numbers (Micka and Driscoll, 2009). Various engine configurations have been proposed to achieve this. One potential design consists of sealing the ramjet inlets during high-altitude scramjet flight to prevent shockwaves on the ramjet fore-body causing excessive drag (Neill and Pesyridis, 2017). Baidya et al. (2018) used RANS CFD to complete a geometric study on the optimal configuration for the nozzle of such a engine operating in the ramjet regime. This nozzle would need to provide sufficient thrust to accelerate the aircraft until scramjet operation could begin. CFD was used to perform a parametric study over various flight conditions for three nozzles of interest: conical, bell, and dual-bell. Furthermore, the computational results were validated against published experimental and CFD data. Overall it was found that the dual-bell nozzle provided the highest thrust and would therefore be the most suitable choice for a dual-mode scramjet/ramjet operating over a range of flight conditions.

# Chapter 3

## Turbulent Combustion Modeling

This chapter details the main conservation equations describing chemically reacting flow. First, the compressible non-reactive equations are presented, followed by the modifications which extend them to multi-species reactive flow. Lastly, turbulence and reaction rate closure is discussed.

### 3.1 Non-Reactive Conservation Equations

A conservation equation can be expressed for any conserved fluid variable  $\psi$  by the following equation, written in tensor notation:

$$\frac{\partial \psi}{\partial t} + \frac{\partial}{\partial x_j}(\psi u_j) = S \quad (3.1)$$

Here  $S$  refers to any sources or sinks of  $\psi$ , and  $u$  the fluid velocity. In regards to the finite volume method, Eq. 3.1 can be expressed as the balance of the sum of the accumulation of  $\psi$  over time within a control volume and the transfer of  $\psi$  through the volume's surface (the first two terms), to the sources and sinks of  $\psi$  within the volume (the term on the right-hand side).

The properties of a fluid flow are completely defined by the conservation equations of three quantities: mass, momentum, and energy (Hirsh, 2007). The equation for mass conservation (continuity) is derived by setting  $\psi = \rho$  in Eq. 3.1 and by assuming there are no sources or sinks of mass, resulting in:

$$\frac{\partial \rho}{\partial t} + \frac{\partial}{\partial x_j}(\rho u_j) = 0 \quad (3.2)$$

Next, the conservation of momentum is derived by setting  $\psi = \rho u_i$  (momentum per unit volume). From Newton's second law, the source or sink of momentum for a control volume is equal to the net force acting

on that control volume. These include both body ( $S_B$ ) and surface forces. Surface forces include the effect of pressure ( $P$ ) and viscous stresses ( $\tau$ ). Body forces can include gravity, electromagnetic effects, as well as others. The conservation equation for momentum is given in Eq. 3.3.

$$\frac{\partial \rho u_i}{\partial t} + \frac{\partial}{\partial x_j}(\rho u_i u_j) = -\frac{\partial P}{\partial x_i} + \frac{\partial \tau_{ij}}{\partial x_j} + \rho S_{B,i} \quad (3.3)$$

The energy equation is obtained through the application of the first law of thermodynamics, commonly referred to as the conservation of energy. It can be expressed in various forms depending on the choice of variable. One such form is defined in terms of the total energy, given by:

$$E = e + \frac{u_i u_i}{2} \quad (3.4)$$

Where  $E$  is the total energy and  $e$  is the internal energy, both per unit mass. Setting  $\psi$  equal to  $\rho E$  (total energy per unit volume), the energy equation can be obtained as:

$$\frac{\partial \rho E}{\partial t} + \frac{\partial}{\partial x_j}(\rho u_j E) = -\frac{\partial P u_j}{\partial x_j} + \frac{\partial u_i \tau_{ij}}{\partial x_j} - \frac{\partial q_j}{\partial x_j} + \rho u_j S_{B,j} + Q_H \quad (3.5)$$

$Q_H$  is a volume heat source term (such as due to radiation heat transfer or an ignition electric spark), and  $\rho u_j S_{B,j}$  is the work done by body forces. The term  $q_i$  is the energy flux and represents the effect of heat conduction. For multi-species fluids it will also include the diffusion of species with different enthalpies (Poinsot and Veynante, 2011). Note that additional source terms are included, which account for the work of pressure and viscosity. Eqs. 3.2, 3.3, and 3.5 together are the compressible Navier-Stokes equations. To fully close the above equations, an equation of state and constitutive equations must be specified. Additionally, modifications are needed to extend these equations to multiple-species reactive flow. These will be introduced in the following section.

## 3.2 Extension of Conservation Equations to Reactive Flow

Eqs. 3.2, 3.3, and 3.5 govern the fluid flow for a single species. However, in reactive flows multiple species are present with varying properties. Additionally, constitutive equations will need to be introduced to close the set of equations. The modifications and the required constitutive equations for each conservation equation are discussed below.

### 3.2.1 Mass and Species Conservation

In addition to overall mass conservation, additional equations are needed for each species. These equations track the overall changes in the mass of a particular chemical species as it is formed or lost to chemical reaction throughout the flow. A continuity expression for species  $k$  is therefore introduced (Poinsot and Veynante, 2011):

$$\frac{\partial \rho Y_k}{\partial t} + \frac{\partial}{\partial x_j} (\rho Y_k (u_j + V_{k,j})) = S_k \quad (3.6)$$

Here  $k$  ranges from 1 to  $N_k$ , where  $N_k$  is the number of chemical species.  $Y_k$  is the mass fraction of species  $k$  (which can be defined as the ratio of the density of species  $k$  to that of the overall mixture). The source term  $S_k$  represents the production (or loss) of species  $k$  due to chemical reaction. Lastly,  $V_{k,j}$  is the  $j$ th-component of the diffusion velocity for species  $k$ . It is important to note that when Eq. 3.6 is summed over all species, it results in Eq. 3.2 (which requires the sum of  $S_k$  over all species to equal zero). Therefore, overall mass is still conserved. This condition can be expressed as (Kuo and Acharya, 2012):

$$\sum_{k=1}^{N_k} Y_k V_{k,j} = 0 \quad (3.7)$$

In this work cross-diffusion, where a gradient in the concentration of one species induces a flux of another chemical species, is neglected. Furthermore, the Soret effect, where small light molecules and large heavy molecules separate under a temperature gradient, is also neglected. Due to these approximations, to satisfy the above condition there is a need for a correction velocity  $V_{c,j}$  (Kuo and Acharya, 2012). The diffusion velocity is therefore defined as:

$$V_{k,j} = V_{k,j}^* + V_{c,j} \quad (3.8)$$

This correction velocity is calculated such that mass conservation is recovered if all species equations are summed, as shown (Kuo and Acharya, 2012):

$$V_{c,j} = - \sum_{k=1}^{N_k} Y_k V_{k,j}^* \quad (3.9)$$

A common assumption for multi-species gas flows for the molecular diffusion term  $Y_k V_{k,j}$  is Fick's Law, given by (Poinsot and Veynante, 2011):

$$Y_k V_{k,j} = -D_k \frac{\partial Y_k}{\partial x_j} \quad (3.10)$$

where  $D_k$  is a diffusion constant for species  $k$ .

### 3.2.2 Momentum Conservation

The conservation of momentum for a reactive flow is the same as for a non-reactive flow (Eq. 3.3). However, a constitutive equation is needed for the viscous stress tensor. Assuming the fluid to be Newtonian and using Stoke's hypothesis, this is given by:

$$\tau_{ij} = \mu \left( \frac{\partial u_i}{\partial x_j} + \frac{\partial u_j}{\partial x_i} - \frac{2}{3} \frac{\partial u_k}{\partial x_k} \delta_{ij} \right) \quad (3.11)$$

where  $\mu$  is the dynamic viscosity.

### 3.2.3 Energy Conservation

Starting from Eq. 3.5, the first modification required for reactive multi-species flow is the need to account for the effects of body forces on each species and the diffusion velocity. Consequently, the body force term  $\rho S_{B,i} u_i$  is replaced with  $\rho \sum_{k=1}^N S_{B,i}(u_i + V_{k,i})$ . Additionally, a constitutive equation is required for the energy flux term  $q_i$ . For multi-species gas, this term is equal to the diffusion of heat due to conduction as well as the diffusion of species with varying enthalpies. Therefore, using Fourier's Law this term can be expressed as:

$$q_i = -\lambda \frac{\partial T}{\partial x_i} + \rho \sum_{k=1}^{N_k} h_k Y_k V_{k,i} \quad (3.12)$$

with  $\lambda$  being the thermal conductivity. Additionally, an alternative form of Eq. 3.5 often used in CFD codes is expressed in terms of sensible enthalpy ( $h_s$ ) (Poinsot and Veynante, 2011). The relation between sensible enthalpy, total enthalpy ( $h_t$ ), and chemical enthalpy ( $h_{f,k}^0$ ) per unit mass is defined below.

$$h_t = h_s + \Delta h_{f,k}^0 = \int_{T_0}^T C_{pk} dT + \Delta h_{f,k}^0 \quad (3.13)$$

As seen in Eq. 3.13, the total enthalpy is the sum of the chemical enthalpy and sensible enthalpy, both of which are defined relative to a reference temperature  $T_0$ , usually taken as 298.15 K (Turns, 2000). Chemical enthalpy reflects the potential chemical enthalpy in chemical bonds in the reactive species, while the sensible enthalpy accounts for enthalpy changes associated with the temperature. Rewriting Eq. 3.5 in terms of  $h_s$  gives (Poinsot and Veynante, 2011):

$$\rho \frac{D h_s}{Dt} = \frac{DP}{Dt} + \tau_{ij} \frac{\partial u_i}{\partial x_j} + \frac{\partial}{\partial x_i} \left( \lambda \frac{\partial T}{\partial x_i} \right) - \frac{\partial}{\partial x_i} \left( \rho \sum_{k=1}^{N_k} h_{s,k} Y_k V_{k,i} \right) + S_T + Q_H + \rho u_j S_{B,j} \quad (3.14)$$

Note that  $\frac{D}{Dt}$  refers to the substantial or material derivative. Additionally, here  $S_T$  is the heat of combustion:

$$S_T = - \sum_{k=1}^{N_k} \Delta h_{f,k}^0 S_k \quad (3.15)$$

The above equations describe the necessary modifications to the standard compressible Navier-Stokes equations to allow for multi-species reactive flow. However, to fully close and be able to solve this system of equations, relations for the turbulence and chemical reaction rate must be introduced. These relations are discussed in Sections 3.6 and 3.7, respectively. However, first Section 3.3 discusses the equation of state and thermodynamic models used throughout this work.

### 3.3 Equation of State and Modelling Fluid Properties

In this work only gaseous products and reactants at low pressure are considered. Therefore, all species are assumed to obey the ideal gas law, which provides the following equation of state:

$$\rho = \frac{P}{RT \sum_{k=1}^{N_k} \frac{Y_k}{M_k}} \quad (3.16)$$

here  $R$  is the universal gas constant, and  $M_k$  is the molecular weight of species  $k$ . For the dynamic viscosity, for all OpenFOAM simulations in this work it is estimated using Sutherland's formula (Sutherland, 1893):

$$\mu = A_s \frac{\sqrt{T}}{1 + \frac{T_s}{T}} \quad (3.17)$$

where  $A_s$  and  $T_s$  are model constants. In this work they were determined for each species by first calculating the viscosities over a temperature range of 200 to 2500 K using the standard kinetic theory of gases (Hirschfelder et al., 1954). The coefficients were then calculated from a least-squares polynomial fit over the calculated viscosities. This resulted in a unique set of  $A_s$  and  $T_s$  for each species.

For all OpenFOAM simulations thermodynamics properties were calculated using the NASA JANAF polynomial model. The polynomials for the specific heat capacity and sensible enthalpy are given by Eqs. 3.18 and 3.19, respectively. The values of the coefficients ( $a_1$  to  $a_6$ ) for both the high and low temperature ranges were provided with the GRI-Mech 3.0 mechanism and are valid over the range of 200 to 3500 K (Smith

et al., 1999). The overall mixture thermodynamic properties are calculated based on a mass-weighted average of the individual species properties.

$$\frac{C_p}{R} = a_1 + a_2 T + a_3 T^2 + a_4 T^3 + a_5 T^4 \quad (3.18)$$

$$\frac{h_s}{RT} = a_1 + a_2 \frac{T}{2} + a_3 \frac{T^2}{3} + a_4 \frac{T^3}{4} + a_5 \frac{T^4}{5} + \frac{a_6}{T} \quad (3.19)$$

Lastly, the modified Eucken method was used to calculate the thermal conductivity for all OpenFOAM simulations:

$$\lambda = \mu C_v \left( 1.32 + \frac{1.77R}{C_v} \right) \quad (3.20)$$

### 3.4 Non-dimensional Numbers

Before continuing it is worthwhile to define some non-dimensional numbers commonly used in combustion.

First is the Schmidt number  $Sc$ , which is the ratio of momentum to mass transport:

$$Sc = \frac{\mu}{\rho D_k} \quad (3.21)$$

The Prandtl number is the ratio of momentum and thermal transport:

$$Pr = \frac{\mu C_p}{\lambda} \quad (3.22)$$

And lastly is the Lewis number, which is the ratio of thermal and mass diffusivity:

$$Le = \frac{Sc}{Pr} = \frac{\lambda}{\rho D_k C_p} \quad (3.23)$$

The Lewis number is a local quantity in a flow, but it has been observed to be mostly constant and changes only a few percent in the flame (Poinsot and Veynante, 2011). Additionally, the Prandtl number is often set to be constant in many combustion analyses, with values typically ranging from 0.7-1. In this work it has been set to a constant value of 1. Furthermore, the Lewis number has been assumed to equal 1, which sets the Schmidt number equal to 1 as well. From this, along with Fick's law, the following simplifications can be made:

$$\rho Y_k V_{k,j}^* = -\rho D \frac{\partial Y_k}{\partial x_j} = -\mu \frac{\partial Y_k}{\partial x_j} \quad (3.24)$$

$$V_{c,j} = - \sum_{k=1}^{N_k} Y_k V_{k,j}^* = \sum_{k=1}^{N_k} D \frac{\partial Y_k}{\partial x_j} = \frac{\lambda}{\rho C_p} \sum_{k=1}^{N_k} \frac{\partial Y_k}{\partial x_j} = 0 \quad (3.25)$$

An additional dimensionless number used extensively in combustion modelling is the Damköhler number ( $Da$ ), defined in Eq. 3.26. This number is the ratio of the flow timescale ( $\tau_f$ ) to the chemical timescale ( $\tau_c$ ). When  $Da$  is large, the chemical timescales are much smaller than the mechanical timescales, and the reaction rate will be limited by the mixing rate.

$$Da = \frac{\tau_f}{\tau_c} \quad (3.26)$$

### 3.5 Cantera Transport Modeling

To compare the effects of the mass, momentum, and energy transfer assumptions previously discussed, some of the results of this work are compared to results obtained with version 2.5.1 of the Cantera software package (Goodwin et al., 2021). For species diffusion in Cantera, rather than using a unity Schmidt number assumption, in this work the Hirschfelder-Curtis-Bird approximation was used along with Fick's law as described by Kee et al. (2017). This mixture-averaged approach is shown in Eq. 3.27, where  $D_k^{mix}$  represents the diffusion of species  $k$  into the mixture of other gasses.  $D_{kj}$  is the binary diffusion coefficient and is determined from molecular theory (Kee et al., 2017).

$$D_k^{mix} = \frac{1 - X_k}{\sum_{j \neq k}^{N_k} \frac{X_j}{D_{kj}}} \quad (3.27)$$

For the viscosity, Wilke's method was used as follows (Wilke, 1950):

$$\mu^{mix} = \sum_{k=1}^{N_k} \frac{X_k \mu_k}{\sum_{j=1}^{N_k} X_j \Phi_{kj}} \quad (3.28)$$

where  $\mu_k$  is the viscosity of species  $k$  and  $\Phi$  is given by:

$$\Phi_{kj} = \frac{\left[ 1 + (\mu_k / \mu_j)^{1/2} (M_j / M_k)^{1/4} \right]^2}{\sqrt{2} (1 + M_k / M_j)^{1/2}} \quad (3.29)$$

Lastly, the mixture-averaged approach used in Cantera to calculate the thermal conductivity in this work uses the rule proposed by Mathur et al. (1967) as shown in Eq. 3.30. Here  $\lambda_k$  is the thermal conductivity

of the individual species which can again be derived from molecular theory. Further details are provided by Kee et al. (2017).

$$\lambda^{mix} = \frac{1}{2} \left( \sum_{k=1}^{N_k} X_k \lambda_k + \frac{1}{\sum_{k=1}^{N_k} X_k / \lambda_k} \right) \quad (3.30)$$

## 3.6 Turbulence Modeling

The reactive Navier-Stokes equations, along with the closures discussed previously, can be directly solved for a given problem provided the mesh and time refinement used are fine enough to resolve all turbulent and chemical scales. However, for turbulent flows the computational cost scales non-linearly with the Reynolds number. In particular, if  $n$  points are desired per unit length for the smallest eddy in homogeneous turbulence, the resulting number of mesh points scales with  $n^3 Re^{\frac{9}{4}}$  for the required spatial resolution and  $Re^{\frac{3}{4}}$  for adequate time resolution (Hirsh, 2007). As a result, the computational cost for direct simulation scales with  $Re^3$  for turbulent flows. Consequently, the required mesh and time resolution for most engineering flows, such as those in aerospace, is not feasible given the large computational requirement (Slotnick et al., 2014). To reduce the computational cost of these flows, statistical methods such as RANS and LES have been developed. In this work only RANS turbulence modelling was used, so this method will be briefly discussed in Section 3.6.1.

### 3.6.1 RANS Models

For many applications of CFD, time-averaged flow properties (such as average velocity, average pressure, etc.) are sufficient. Additionally, low computational cost models are often sought which limit the time and resources needed to solve a given flow field. For these reasons, the most common procedures in turbulent flow computations are based on the RANS turbulence equations, and likely will continue to be for some time (Versteeg and Malaasekera, 2007). These equations are derived by time-averaging the Navier-Stokes equations, with the goal of eliminating the temporal fluctuations.

#### Reynolds and Favre Averaging

When the flow is turbulent, local flow properties fluctuate in time. Therefore, any quantity  $\phi$  can be decomposed into an average ( $\bar{\phi}$ ) and fluctuating ( $\phi'$ ) component as shown in Eq. 3.31. This is known as Reynolds decomposition.

$$\phi = \bar{\phi} + \phi' \quad (3.31)$$

The average quantity  $\bar{\phi}$  can be defined as a time average:

$$\bar{\phi} = \frac{1}{\Delta t} \int_t^{t+\Delta t} \phi(x_i, t) dt' \quad (3.32)$$

When density is not constant, time-averaging will result in terms containing the correlation of  $\rho'$  and other flow properties. These are often neglected in variable density flows and are assumed to be negligible (Bilger, 1975). However, for flows with combustion, this is not the case and due to large variations in density they cannot be neglected. Therefore, approximations would be needed for each of these correlations. Instead, a density-based averaging known as Favre averaging is used instead of Reynolds averaging, which is shown below:

$$\tilde{\phi} = \frac{\overline{\rho\phi}}{\overline{\rho}} \quad (3.33)$$

Favre averaging does not lead to terms containing the correlation of  $\rho'$  and other flow properties like in RANS averaging. Additionally, flow properties can be still be decomposed into a mean and fluctuating part, as shown:

$$\phi = \tilde{\phi} + \phi'' \quad (3.34)$$

It is worth noting that this fluctuating quantity also includes the effects of density fluctuations.

### Favre Averaged Navier-Stokes Equations

In order to Favre-average the Navier-Stokes equations, the pressure, density, and source terms (such as those due to chemical reactions) are split into a mean and fluctuating component through Reynolds decomposition as shown in Eq. 3.31 (Wilcox, 2006). In contrast, the velocity, enthalpy, species mass fraction, and temperature are decomposed in a mass-averaged manner (Eq. 3.34). After making these substitutions and applying Favre-averaging operations, the resulting equations for mass, momentum, chemical species, and sensible enthalpy are shown in Eqs. 3.35, 3.36, 3.37, and 3.38, respectively (Poinsot and Veynante, 2011).

$$\frac{\partial \overline{\rho}}{\partial t} + \frac{\partial}{\partial x_j} (\overline{\rho} \tilde{u}_j) = 0 \quad (3.35)$$

$$\frac{\partial \overline{\rho} \tilde{u}_i}{\partial t} + \frac{\partial}{\partial x_j} (\overline{\rho} \tilde{u}_i \tilde{u}_j) + \frac{\partial \overline{P}}{\partial x_j} = \frac{\partial}{\partial x_j} \left( \overline{\tau}_{ij} - \widetilde{\overline{\rho} u_i'' u_j''} \right) + \overline{S_{B,i}} \quad (3.36)$$

$$\frac{\partial \bar{\rho} \tilde{Y}_k}{\partial t} + \frac{\partial}{\partial x_j} (\bar{\rho} \tilde{u}_j \tilde{Y}_k) = - \frac{\partial}{\partial x_j} \left( \overline{V_{k,j} Y_k} + \widetilde{\bar{\rho} u''_j Y''_k} \right) + \overline{S_k} \quad \text{for } k = 1 \text{ to } N_k \quad (3.37)$$

$$\frac{\partial \bar{\rho} \tilde{h}_s}{\partial t} + \frac{\partial}{\partial x_j} (\bar{\rho} \tilde{u}_j \tilde{h}_s) = \overline{S_T} + \overline{\frac{DP}{Dt}} + \frac{\partial}{\partial x_j} \left( \lambda \overline{\frac{\partial T}{\partial x_j}} - \overline{\rho u''_j h''_s} \right) + \overline{\tau_{ij} \frac{\partial u_j}{\partial x_i}} - \frac{\partial}{\partial x_j} \left( \overline{\rho \sum_{k=1}^{N_k} V_{k,j} Y_k h_{s,k}} \right) + \overline{Q_H} + \overline{\rho u_j S_{B,j}} \quad (3.38)$$

where

$$\overline{\frac{DP}{Dt}} = \frac{\partial \bar{P}}{\partial t} + \tilde{u}_j \frac{\partial \bar{P}}{\partial x_j} + \overline{u''_j \frac{\partial P}{\partial x_j}} \quad (3.39)$$

In Eqs. 3.35 to 3.38 several terms require additional modelling assumptions, namely: the Reynolds stress term ( $\widetilde{u''_i u''_j}$ ), the chemical reaction rates ( $\overline{S_k}$ , and consequently  $\overline{S_T}$  through Eq. 3.15), the species turbulent flux ( $\widetilde{u''_i Y''_k}$ ), the enthalpy turbulent flux ( $\widetilde{u''_i h''_s}$ ), the laminar species flux ( $\overline{V_{k,j} Y_k}$ ), the laminar energy flux ( $\overline{\lambda \frac{\partial T}{\partial x_i}}$ ), and lastly the pressure velocity correlation ( $\overline{u''_i \frac{\partial p}{\partial x_i}}$ ). The model for the Reynolds stress depends on the turbulence model used and is discussed in Section 3.6.2. Additionally, the modelling of the chemical reaction rate is an important objective for most studies of turbulent combustion, and is discussed in Section 3.7.

In regards to the species and enthalpy turbulent fluxes, it is common to close these terms using a gradient assumption, as follows (Poinsot and Veynante, 2011):

$$\widetilde{\bar{\rho} u''_j Y''_k} = - \frac{\mu_t}{Sc_t} \frac{\partial \widetilde{Y}_k}{\partial x_j} \quad (3.40)$$

$$\widetilde{\bar{\rho} u''_j h''_s} = - \frac{\mu_t}{Pr_t} \frac{\partial \widetilde{h}_s}{\partial x_j} \quad (3.41)$$

The turbulent viscosity  $\mu_t$  represents the additional viscosity due to turbulence and it estimated from the turbulence model.  $Sc_t$  is the turbulent Schmidt number, which compares momentum and molecular diffusion for the species  $k$ , while  $Pr_t$  is the turbulent Prandtl number which compares momentum and heat diffusion. As discussed in Section 3.4, both are set to 1 for this work.

Next, the laminar diffusive fluxes for species and enthalpy need to be addressed. In large Reynolds number flows, these terms are often neglected and assumed to be negligible compared to the corresponding turbulent terms (Poinsot and Veynante, 2011). However, one approach in modelling the species laminar diffusion flux is:

$$\overline{V_{k,j} Y_k} = -\bar{\rho} \overline{D_k} \frac{\partial \tilde{Y}_k}{\partial x_j} \quad (3.42)$$

Note here that  $\overline{D_k}$  is a mean species molecular diffusion coefficient. Additionally, the laminar heat diffusion term can be rewritten using a mean thermal diffusivity, as shown in Eq. 3.43.

$$\overline{\lambda \frac{\partial T}{\partial x_i}} = \bar{\lambda} \frac{\partial \tilde{T}}{\partial x_i} \quad (3.43)$$

However, even with modelling options available, to reduce computational cost in this work both laminar fluxes are assumed negligible compared to the turbulent transport and are therefore neglected. Lastly, there is the pressure-velocity correlation ( $\overline{u_i'' \frac{\partial P}{\partial x_i}}$ ). This term is neglected, as it done in many RANS codes (Poinsot and Veynante, 2011).

### 3.6.2 RANS Turbulence Models

As stated previously, in the process of Reynolds or Favre averaging the Navier-Stokes equations, an additional non-linear term appears, known as the Reynolds stress ( $\widetilde{u_i'' u_j''}$ ). This term is calculated from a turbulence model, which are often based on the turbulent viscosity hypothesis or from Reynolds Stress transport equations (Pope, 2000). The Boussinesq hypothesis states that the Reynolds stress term is given by:

$$\widetilde{\rho u_i'' u_j''} = \frac{2}{3} \bar{\rho} k \delta_{ij} - \mu_t \left( \frac{\partial \tilde{u}_j}{\partial x_i} + \frac{\partial \tilde{u}_i}{\partial x_j} - \frac{2}{3} \frac{\partial \tilde{u}_k}{\partial x_k} \delta_{ij} \right) \quad (3.44)$$

where  $\mu_t$  is the turbulent dynamic viscosity, and  $k$  is the turbulent kinetic energy. Note that the turbulent viscosity hypothesis is analogous to the viscous tensor  $\tau_{ij}$  for a Newtonian fluid. However, an equation for  $\mu_t$  is still required. The form of this equation depends on the turbulence model used. Three common models are discussed in this work, namely the  $k - \epsilon$  model, the  $k - \omega$  model, and the  $k - \omega$  SST model. These models are all two-equation models, meaning they introduce two additional transport equations to the set of Navier-Stokes equations which need to be solved.

#### Standard $k-\epsilon$ Turbulence Model

The  $k-\epsilon$  model, proposed by Launder and Spalding, introduces one equation for the turbulent kinetic energy  $k$  and one for the turbulence dissipation rate  $\epsilon$  (Launder and Spalding, 1974). The transport equations for  $k$  and  $\epsilon$  are shown in Eqs. 3.45 and 3.46, respectively.

$$\frac{D}{Dt} (\rho k) = \frac{\partial}{\partial x_j} \left[ \left( \mu + \frac{\mu_t}{\sigma_{k2}} \right) \frac{\partial k}{\partial x_j} \right] + P_k - \rho \epsilon \quad (3.45)$$

$$\frac{D}{Dt} (\rho \epsilon) = \frac{\partial}{\partial x_j} \left[ \left( \mu + \frac{\mu_t}{\sigma_\epsilon} \right) \frac{\partial \epsilon}{\partial x_j} \right] + \frac{C_1 \epsilon}{k} P_k - C_2 \rho \frac{\epsilon^2}{k} \quad (3.46)$$

$C_1$ ,  $C_2$ ,  $\sigma_\epsilon$ , and  $\sigma_{k2}$  are all model constants.  $P_k$  is a source term for turbulent kinetic energy and is given by:

$$P_k = -\bar{\rho} \widetilde{u_i'' u_j''} \frac{\partial \widetilde{u}_i}{\partial x_j} \quad (3.47)$$

where the Reynolds stresses  $-\bar{\rho} \widetilde{u_i'' u_j''}$  are calculated using Eq. 3.44. The turbulent viscosity  $\mu_t$  is calculated from  $k$  and  $\epsilon$ , as shown:

$$\mu_t = C_\mu \frac{\rho k^2}{\epsilon} \quad (3.48)$$

where  $C_\mu$  is a model constant set to 0.09.

### k- $\omega$ Model

The Wilcox k- $\omega$  turbulence model uses the specific turbulence dissipation rate  $\omega$  in place of  $\epsilon$  (Wilcox, 2006).

The transport equation for  $k$  is:

$$\frac{D}{Dt} (\rho k) = \frac{\partial}{\partial x_j} \left[ (\mu + \sigma_k \mu_t) \frac{\partial k}{\partial x_j} \right] + P_k - \beta^* \rho \omega k \quad (3.49)$$

And the transport equation for  $\omega$  is:

$$\frac{D}{Dt} (\rho \omega) = \frac{\gamma \omega}{k} P_k - \beta \rho \omega^2 + \frac{\partial}{\partial x_j} \left[ (\mu + \sigma_{\omega1} \mu_t) \frac{\partial \omega}{\partial x_j} \right] + \frac{\rho \sigma_d}{\omega} \frac{\partial k}{\partial x_j} \frac{\partial \omega}{\partial x_j} \quad (3.50)$$

where  $\sigma_k$ ,  $\beta^*$ ,  $\gamma$ ,  $\beta$ ,  $\sigma_{\omega1}$ , and  $\sigma_d$  are all model constants. The turbulent viscosity is then calculated as:

$$\mu_t = \frac{\rho k}{\omega} \quad (3.51)$$

A complete description of the model constants and auxiliary functions is given by Wilcox (2006).

### k- $\omega$ SST Model

The previous two turbulence models suffer from known deficiencies. In particular, the k- $\epsilon$  model is not suitable to simulate the behaviour of turbulent boundary layers up to separation (Wilcox, 2006). Conversely, the k- $\omega$

model is significantly more accurate in the near-wall region, and has been successful in flows with adverse pressure gradients including those with separation (Menter, 1993). However, outside the boundary-layer, the  $k-\omega$  model has shown a sensitivity to the values of  $\omega$  (Menter, 1992). To overcome the deficiencies in these models, the Menter BSL (or baseline) model was created (Menter, 1994). This model is a blend or hybridization of the  $k-\epsilon$  and  $k-\omega$  models, with the  $k-\epsilon$  model being prominent in the free-stream and the  $k-\omega$  model being used near the wall.

In addition to the baseline model, the  $k-\omega$  SST model was created which added limiters to the eddy viscosity and the production of turbulent kinetic energy (Menter, 1994). This was done to improve the results in flows with adverse pressure gradients. The transport equations for  $k$  and  $\omega$  are shown in Eqs. 3.52 and 3.53, respectively.

$$\frac{D}{Dt}(\rho k) = P_{k,min} - \beta^* \rho \omega k + \frac{\partial}{\partial x_j} \left[ (\mu + \sigma_k \mu_t) \frac{\partial k}{\partial x_j} \right] \quad (3.52)$$

$$\frac{D}{Dt}(\rho \omega) = \frac{\alpha}{\nu_t} P_{k,min} - \beta \rho \omega^2 k \frac{\partial}{\partial x_j} \left[ (\mu + \sigma_\omega \mu_t) \frac{\partial \omega}{\partial x_j} \right] + 2(1 - F_1) \frac{\rho \sigma_{\omega 2}}{\omega} \frac{\partial k}{\partial x_j} \frac{\partial \omega}{\partial x_j} \quad (3.53)$$

Here the production term ( $P_{k,min}$ ) has been limited as shown:

$$P_{k,min} = \min(P_k, 10\beta^* \rho k \omega) \quad (3.54)$$

$F_1$  is the blending function, and its role is to control the relative contribution of each model based on the distance to the nearest wall. The value of this function is designed to be one through the viscous and logarithmic sub-layers of the boundary layer but tends towards zero gradually in the wake or free stream region (Menter, 1994). Its form is shown in Eq. 3.55.

$$F_1 = \tanh \left( \left[ \min \left( \max \left[ \frac{\sqrt{k}}{\beta^* \omega y}, \frac{500\nu}{y^2 \omega} \right], \frac{4\rho \sigma_{\omega 2} k}{CD_{k\omega} y^2} \right) \right]^4 \right) \quad (3.55)$$

$CD_{k\omega}$  is a cross-diffusion term, calculated as shown in Eq. 3.56, and  $y$  is the distance to the closest wall.

$$CD_{k\omega} = \max \left( 2\rho \sigma_{\omega 2} \frac{1}{\omega} \frac{\partial k}{\partial x_i} \frac{\partial \omega}{\partial x_i}, 10^{-10} \right) \quad (3.56)$$

The turbulent viscosity is calculated as shown in Eq. 3.57.  $F_2$  is another blending function, shown in Eq. 3.58. Lastly,  $W_{ij}$  is the rotation tensor, with its definition given in Eq. 3.59.

$$\mu_t = \frac{\rho a k}{\max(a\omega, \sqrt{2W_{ij}W_{ij}}F_2)} \quad (3.57)$$

$$F_2 = \tanh \left[ \left( \max \left[ \frac{2\sqrt{k}}{\beta^* \omega y}, \frac{500\nu}{y^2 \omega} \right] \right)^2 \right] \quad (3.58)$$

$$W_{ij} = \frac{1}{2} \left( \frac{\partial u_i}{\partial x_j} - \frac{\partial u_j}{\partial x_i} \right) \quad (3.59)$$

The model constants (such as  $\sigma_k$ ) were determined by blending the constants from the  $k - \epsilon$  and  $k - \omega$  models as shown in Eq. 3.60 for a general constant  $\phi$ . Note that  $\phi_1$  refers to the value from the  $k - \omega$  model and  $\phi_2$  refers to one from the  $k - \epsilon$  model. A summary of the default model constants used in OpenFOAM are shown in Table 3.1. These constants were not modified in this work.

$$\phi = F_1\phi_1 + (1 - F_1)\phi_2 \quad (3.60)$$

Table 3.1:  $k-\omega$  SST Model Coefficients

Constant	Value
$\sigma_{k1}$	0.85
$\sigma_{k2}$	1
$\gamma_1$	0.555
$\gamma_2$	0.44
$\sigma_{\omega1}$	0.5
$\sigma_{\omega2}$	0.856
$\beta_1$	0.075
$\beta_2$	0.0828
$\beta^*$	0.09
a	0.31

## 3.7 Chemical Reaction Modeling

As previously mentioned, a combustion model is used to close the mean reaction rate in the RANS equations. Various models are available for this purpose. In this work, the Partially Stirred Reactor combustion model is used, described in Section 3.7.2. Details of the model selection is given in Section 3.7.3. However, first information regarding chemical kinetics are given in Section 3.7.1.

### 3.7.1 Chemical Reactions and Kinetics

Chemical mechanisms generally contain a large number of elementary reactions. These elementary reactions capture the formation of intermediate species and radicals, and are necessary to accurately represent combustion. For a mechanism of  $N_k$  species undergoing  $N_r$  reactions, the complete system can be represented by (Poinsot and Veynante, 2011):

$$\sum_{k=1}^{N_k} v'_{kr}[X_k] \rightleftharpoons \sum_{k=1}^{N_k} v''_{kr}[X_k] \quad \text{for } r = 1 \text{ to } N_r \quad (3.61)$$

where  $v'_{kr}$  and  $v''_{kr}$  are the molar stoichiometric coefficients of the  $k$ -th species in reaction  $r$  and  $[X_k]$  is the molar concentration of species  $k$ . The “progress rate”  $R_r$  (in mol/m<sup>3</sup>-s) compares the rates of the forward and reverse reactions for a reversible reaction  $r$ . It is written as shown in Eq. 3.62.

$$R_r = K_{fr} \prod_{k=1}^{N_k} [X_k]^{\nu'_{kj}} - K_{br} \prod_{k=1}^{N_k} [X_k]^{\nu''_{kj}} \quad (3.62)$$

Here  $K_{fr}$  and  $K_{br}$  are the forward and reverse rate constants for reaction  $r$ , respectively. If the reaction is non-reversible,  $K_{br}$  is set to zero. The rate constants are modelled using an empirical Arrhenius law, shown in Eq. 3.63. Here  $A_{fr}$  is the pre-exponential constant for the forward reaction,  $\beta_j$  is the temperature exponent, and  $T_{aj}$  is the activation temperature.

$$K_{fr} = A_{fr} T^{\beta_j} \exp\left(-\frac{T_{aj}}{T}\right) \quad (3.63)$$

For a given reaction  $r$ , the production of species  $k$  is expressed as shown in Eq. 3.64. The overall Arrhenius (or laminar) reaction rate for species  $k$  ( $S_{k,arr}$ ) is simply the sum of Eq. 3.64 over all reactions, as shown in Eq. 3.65.

$$S_{k,r} = M_k \left( v''_{kr} - v'_{kr} \right) R_r \quad (3.64)$$

$$S_{k,arr} = \sum_{r=1}^{N_r} S_{k,r} \quad (3.65)$$

An ordinary differential equation (ODE) solver is needed to calculate the reaction rate  $S_{k,arr}$ . For all simulations in this work, the implicit Euler chemistry solver was used with an initial chemical time step of  $1\times 10^{-7}$ s. This solver was observed to be stable for all chemical mechanisms at all equivalence ratios used throughout this work.

Clearly the Arrhenius law is highly non-linear. Consequently, it is challenging to accurately express this

term as a function of the Favre-averaged variables discussed earlier. One approach is to use a Taylor series expansion for the average reaction rate, however this results in additional unknown correlations which would require modelling (Versteeg and Malaasekera, 2007). Additionally, this modelling is only possible for single-step reactions, and therefore this approach is not useful if complex or multi-step chemical mechanisms are used.

Another approach is to assume the flame is laminar and neglect turbulent fluctuations. The source term for each species ( $S_k$ ) will therefore be equal to  $S_{k,arr}$ . This is known as the Quasi-Laminar or Arrhenius Reaction Rate Model, and is sometimes used in low  $Da$  number flows (Poinsot and Veynante, 2011). Furthermore, it has been used successfully by researchers for ramjet and scramjet applications (Pichon et al., 2012; Choi et al., 2005; Candler et al., 2012). However, it does not take into account the effects of turbulence on combustion and is therefore not suitable for most turbulent flames (Fureby, 2012).

Lastly, another method is to model the interaction between turbulence and combustion. There are a wide range of models available, some of which are discussed in Section 3.7.2. This is the approach taken in this work. Consequently,  $S_k$  is the result of the combustion model, which modifies  $S_{k,arr}$  depending on the form of the chosen model. With  $S_k$  known,  $S_T$  is calculated from Eq. 3.15.

### 3.7.2 Turbulence-Chemistry Interaction

As discussed in Section 3.7.1, simple mean values are insufficient to describe turbulent combustion in most cases. Most combustion models therefore are developed from physical analysis such as comparing physical and chemical timescales (Poinsot and Veynante, 2011). Veynante and Vervisch described three common types of combustion models (Veynante and Vervisch, 2002):

1. Geometric Analysis:

The flame front is treated as a geometric surface which is often linked to an iso-surface of a mixture/mass fraction. This surface will then evolve in the turbulent flow. To estimate the mean reaction rate, the product of the flame area per unit volume and the mean reaction rate per unit flame area is often used. Lastly, often a “flamelet” assumption is used which leads to each flame element being treated as a laminar flame.

2. Turbulent Mixing:

This approach assumes that turbulent mixing controls the reaction rate (therefore, the  $Da$  number is high). How to model the mixing rate (often expressed as a “scalar dissipation rate”) is the main difficulty of this class of model. The Eddy Break-Up Model and Eddy Dissipation Concept Model are popular models based on this type of analysis.

### 3. One-Point Statistics:

Mean values and correlations are determined using a kinetic scheme and the joint probability density function (PDF) for species and enthalpy. Due to this, these models are referred to as ‘PDF’ models. Although this third approach requires no assumptions regarding flamelets or mixing-controlled combustion, additional assumptions are required to model unknown quantities (Poinsot and Veynante, 2011).

This work focuses on models which utilize “Turbulent Mixing” analysis. These models were selected primarily due to their low computational cost compared to other types of models. Additionally, some mixing models allow for the inclusion of detailed chemistry without requiring any modifications. Below three commonly used models of this type are described, namely the eddy break up, the eddy dissipation concept, and partially-stirred reactor models. All three models are available in the default distribution of OpenFOAM.

### Eddy Break Up Model

Originally proposed by Spalding (Spalding, 1971), the Eddy-Break Up (EBU) Model is based on analysis of high  $Re$  and  $Da$  number flows (Poinsot and Veynante, 2011). In this model, the reaction rate is controlled by turbulent mixing rather than chemistry. Consequently, a single step, infinitely fast chemical reaction is generally assumed. The mean reaction rate ( $\overline{S_\zeta}$ ) is given by Eq. 3.66 (Kuo and Acharya, 2012). This equation is written in terms of a non-dimensional flame temperature, which is defined in Eq. 3.67. Note that  $\overline{S_\zeta}$  is the source term in the temperature equation after it has been non-dimensionalised. More details are available in Poinsot and Veynante (2011).

$$\overline{S_\zeta} = C_{EBU} \bar{\rho} \frac{\epsilon}{k} \tilde{\zeta} (1 - \tilde{\zeta}) \quad (3.66)$$

$$\zeta = \frac{T - T_u}{T_b - T_u} \quad (3.67)$$

In these equations  $C_{EBU}$  is a model constant,  $T_u$  is the temperature in the unburned gases, and  $T_b$  is the temperature in the burnt gases. The EBU model is commonly used in combustion codes due to its simplicity (Poinsot and Veynante, 2011). However, the biggest limitation is the exclusion of the effects of chemical kinetics. Furthermore, due to the dependence of the fuel reaction rate on the turbulence timescale, the results will depend on the performance of the turbulence model (Versteeg and Malaasekera, 2007). Therefore, regions or flows where the turbulence model is inaccurate will also lead to inaccurate reaction rate predictions. One example of this shortcoming is the overestimation of the reaction rates in flows with

high turbulence, particularly in highly-strained regions (Poinsot and Veynante, 2011).

### Eddy Dissipation Concept Model

An extension of the EBU model was developed by Magnussen and Hjertager (1977; 1981), known as the Eddy Dissipation Concept (EDC) model. A major difference between the EBU and EDC models is the EDC is a finite rate chemistry model, and therefore can be applied when chemistry has a comparable or larger effect than mixing (Magnussen and Hjertager, 2005). It is based on a turbulence energy cascade model, where energy is transferred from larger to smaller eddies until the smallest energies dissipate the kinetic energy as heat. These small-scale structures responsible for energy dissipation are also critical for the mixing of reactants at a molecular level. These “fine structures” are highly localized and therefore only occupy a small fraction of the total volume of the flow.

The EDC model assumes that most of the chemical reactions occur in these fine structures (Magnussen and Hjertager, 2005). In particular, reactions will occur when the reactants are mixed at a molecular scale at a large enough temperature. It is therefore necessary to model the mass transfer rate between the fine structures and surrounding fluid, as well as the mass fraction of the fine structures in the computational cell. The resulting mean reaction rate proposed by Magnussen and Hjertager (2005) is:

$$\overline{S_k} = \frac{\bar{\rho}\gamma\chi}{\tau^*(1-\gamma\chi)} \left( Y_k^* - \widetilde{Y}_k \right) \quad (3.68)$$

Note that  $\widetilde{Y}_k - Y_k^*$  is the difference in mass fraction between the surrounding fluid and inside the fine structures (the superscript \* refers to properties in the fine structures). The proportion of the flow occupied by fine structures is represented by  $\gamma$ . It can be modelled as shown in Eq. 3.69. Additionally,  $\tau^*$  is the fine structure residence time, calculated as shown in Eq. 3.70.  $C_\gamma$  and  $C_\tau$  are model constants with default values of 4.6 and 0.41, respectively (Magnussen and Hjertager, 2005).

$$\gamma = C_\gamma \left( \frac{\nu \tilde{\epsilon}}{\tilde{k}^2} \right)^{\frac{1}{2}} \quad (3.69)$$

$$\tau^* = C_\tau \left( \frac{\nu}{\tilde{\epsilon}} \right)^{\frac{1}{2}} \quad (3.70)$$

The value of  $\chi$  represents the fraction of fine structures which react. According to Magnussen and Gran (1996), setting the value of  $\chi$  to 1 does not alter the results appreciably. The mean mass fraction,  $\widetilde{Y}_k$ , is obtained by the species transport equation (Li, 2019). Lastly, the mass fraction of each species inside the fine structures,  $Y_k^*$ , needs to be determined. When using detailed chemistry, the EDC model assumes the

fine structures act as constant pressure, adiabatic, homogeneous reactors. Originally, Magnussen proposed assuming a perfectly stirred reactor (PSR) (Magnussen and Hjertager, 2005). This leads to the following set of equations (Gran and Magnussen, 1996):

$$\frac{S_{k,arr}}{\rho^*} = \frac{1}{\tau^*} (Y_k^* - Y_0) \quad (3.71)$$

In Eq. 3.71, the subscript ‘0’ refers to fluid entering the reactor. However, this set of equations is numerically expensive to solve. Additionally, due to chemical kinetic effects, oscillating states may occur in PSRs even with steady input parameters (Bösenhofer et al., 2018). To reduce these oscillations as well as the computation cost, it is common to use a plug flow reactor (PFR) in place of a PSR. A PFR neglects the mixing between the fine structures and the surrounding fluid, resulting in the following equation (Li, 2019):

$$\frac{dY_s^*}{dt} = \frac{S_{k,arr}}{\rho} \quad (3.72)$$

The EDC model has been widely applied in industry for the simulation of turbulent combustion. Furthermore, alternative formulations of the model have been proposed to better handle non-classical combustion cases, such as Moderate and Intense Low-oxygen Dilution (MILD) combustion (Parente et al., 2016). Its success is largely due to its ability to incorporate detailed chemical mechanisms at a more reasonable computational cost compared to other models.

### Partially Stirred Reactor Model

Similar to the EDC model, the Partially Stirred Reactor (PaSR) model splits each computational cell into two locally uniform regions: one where reactions take place and one characterized by mixing where no reactions occur (Nordin, 2001; Golovitchev et al., 2000). The PaSR model assumes the reaction zone is a PSR, and therefore any fluctuations within the reacting zone are assumed to be negligible when determining the chemical source terms. Since reactions only occur in the reaction zone regions, the composition of the cell changes due to the mass exchange between the non-reacting and reacting zones. The mass fraction of the reaction zone is given by the parameter  $\kappa$ , estimated as (Nordin, 2001):

$$\kappa = \frac{\tau_c}{\tau_c + \tau_m} \quad (3.73)$$

where  $\tau_c$  and  $\tau_m$  are the characteristic chemical and mixing timescales, respectively. The mean source term is then expressed as (Nordin, 2001; Chomiak and Karlsson, 1996):

$$\overline{S_k} = \kappa S_{k,arr} \quad (3.74)$$

To determine the chemical timescale, several options are available. As recommended by Fox (2003), one possibility is to use the inverse of the magnitude of the eigenvalues ( $\lambda_k$ ) of the Jacobian matrix of the chemical source terms. The Jacobian matrix has dimensions of  $k \times k$ , where  $k$  is the number of chemical species in the mechanism. Once the eigenvalues are determined, the chemical timescale is estimated as shown:

$$\tau_{c,k} = \frac{1}{|\lambda_k|} \quad (3.75)$$

where  $\tau_{c,k}$  is the chemical timescale of species  $k$ . Once  $\tau_{c,k}$  is found for each species (and the non-reactive species are removed, characterized by an infinite chemical timescale), the maximum value of  $\tau_{c,k}$  is chosen as the chemical timescale. This approach has been found to be more accurate than other chemical timescales, but is much more time consuming, particularly when large chemical mechanisms are used (Li et al., 2018). A simplified approach is estimated based on reaction rates, as shown in Eq. 3.76 (Li et al., 2018; Wartha et al., 2021). Note that for mechanisms with more than one reaction, the ratios of all reactions are summed.

$$\tau_c = \sum_{r=1}^{N_r} \frac{C_{tot}^*}{\sum_{m=1}^{N_{s,RHS}} \left( \frac{dc_{r,f}^*}{dt} v_{m,r} \right)} \quad (3.76)$$

where  $N_{s,RHS}$  is the number of product species for equation  $r$ ,  $C_{tot}^*$  is the total concentration (number of moles of all species per unit volume), and  $v_{m,r}$  is the product stoichiometric coefficient for species  $m$  in reaction  $r$ . The term  $\frac{dc_{r,f}^*}{dt}$  is the forward reaction rate for reaction  $r$ . This method is used as the default chemical timescale in OpenFOAM. It has a relatively low computational cost while still providing comparable accuracy to the eigenvalue approach (Li et al., 2018).

However, this formulation calculates a single  $\tau_c$  value for all reactions (leading to a single  $\kappa$  value) even though many reactions in a given chemical mechanism have significantly different timescales. Additionally, it only considers the forward reaction rate, which may not capture the correct reaction rate for reversible reactions. An alternative approach by Akerblom (2022) attempts to correct these deficiencies. This is accomplished by computing a separate chemical timescale for each reaction, which includes accounting for reversible reactions. This leads to a mass fraction of the reaction zone being calculated for each reaction ( $\kappa_r$ ). In this work both the default method shown in Eq. 3.76 and the approach by Akerblom (2022) was used to calculate the chemical timescale to assess the accuracy of both methods.

Akerblom (2022) originally proposed calculating the residence time for all the reactant species in each

reaction and then selecting the shortest residence time as the chemical timescale for that reaction. This is shown in Eq. 3.77, noting that  $S_{k,r}$  is the consumption rate of species  $k$  due to reaction  $r$ . However, when Eq. 3.77 was used to calculate the chemical timescale, no combustion was observed to occur. This is likely due to the mass fraction of many species ( $Y_k$ ) in many reactions for a given chemical mechanism beginning with an initial value of zero before combustion occurs. This would lead to a value of zero for  $\tau_{c,r}$  for many reactions, leading to zero values for  $\kappa_r$  and therefore a zero reaction rate for those chemical reactions.

$$\tau_{c,r} = \min \left( \frac{\rho Y_k}{|S_{k,r}|} \right) \quad (3.77)$$

An alternative approach used in this work is to calculate the chemical timescale for each reaction as shown in Eq. 3.78 (Wartha et al., 2021), where  $S_r$  is the reaction rate of reaction  $r$  (in kg/s). Following this,  $\kappa_r$  was calculated for each reaction as shown in Eq. 3.79.

$$\tau_{c,r} = \frac{1}{|S_r|} \quad (3.78)$$

$$\kappa_r = \frac{\tau_{c,r}}{\tau_{c,r} + \tau_m} \quad (3.79)$$

For the determination of the mixing timescale ( $\tau_m$ ), several expressions have been proposed. In conventional combustion systems, since reactions are usually assumed to occur at the smallest scales, a natural choice would be to estimate a mixing timescale on the order of the Kolmogorov timescale (Golovitchev et al., 2000). Alternatively, another option is to use the eddy break-up time from large scale non-uniformities (Chomiak and Karlsson, 1996). To achieve a more accurate mixing timescale however, Borghi and Gonzalez (1991) proposed that the mixing timescale should consider the complete spectrum of timescales. To achieve this in a straight-forward manner, the geometric mean of the eddy break-up and Kolmogorov timescales is taken, resulting in (Chomiak and Karlsson, 1996):

$$\tau_{m,mod} = \sqrt{\frac{k}{\epsilon} \left( \frac{\nu}{\epsilon} \right)^{\frac{1}{2}}} \quad (3.80)$$

Another method to calculate the mixing timescale uses the parameter  $C_{mix}$ , as shown:

$$\tau_{m,orig} = C_{mix} \sqrt{\frac{\nu_{eff}}{\epsilon}} \quad (3.81)$$

The constant  $C_{mix}$  is given by Eq. 3.82. It has typical values ranging from 0.001 to 0.3 (Nordin, 2001). Note that  $Re_t$  is the turbulent Reynolds number defined in Eq. 3.83 and  $C_\mu$  is a constant (equal to 0.09). The

value of  $C_{mix}$  must be chosen before the simulation.

$$C_{mix} = \sqrt{\frac{1}{1 + C_\mu Re_t}} \quad (3.82)$$

$$Re_t = \frac{k^2}{\epsilon\nu} \quad (3.83)$$

Eq. 3.81 is the default definition used in OpenFOAM. To calculate  $\tau_{m,mod}$ , a new function was written and implemented into OpenFOAM. In this work, both definitions of  $\tau_m$  were used and compared.

Since the PaSR model explicitly accounts for the mixing and chemical timescales, it allows for a more accurate description of turbulence and chemistry interaction (Li et al., 2018). It will therefore be used as the combustion model for all simulations in this work, with more details on its selection provided in Section 3.7.3.

### 3.7.3 Choice of Combustion Model

In this work, three turbulent mixing models were discussed, namely the EBU, EDC, and PaSR models. However, as noted in Section 3.7.2, a major limitation of the EBU model is the neglection of chemical kinetics. Chemical kinetics can have large effects on combustion simulations, with the choice of chemical mechanism having large effects on flame speed, flame structure, product species concentrations, among other properties (Zettervall et al., 2017; Duwig et al., 2011; Zettervall et al., 2021). The EBU model was therefore not used in this work. However, the other two mixing models discussed are capable of modelling detailed chemistry. To ultimately decide between them, their previous use in simulating ramjet/scramjet combustion and other combustion devices was assessed. In particular, it was found that the PaSR model has been validated for combustors (Nogenmyr et al., 2009; Fedina and Fureby, 2011), including scramjet combustors (Fureby et al., 2015; Nordin-Bates et al., 2017). Furthermore, it has been used to predict the lean blow-out limit of a ramjet (Pichon et al., 2012), as well as provide reasonable agreement between simulation and experimental values for dual mode scramjet/ramjet combustors (Zettervall and Fureby, 2018; Vincent-Randonnier et al., 2018). On the other hand, over-predictions of temperature were observed using the EDC model for ethylene jet flames (Shabanian et al., 2013). Additionally, for a methane jet flame Li et al. (2021) observed the EDC model underestimated the temperature and CO<sub>2</sub> mole fractions compared to experiment, while the PaSR model provided better agreement. A possible reason for the errors in the predictions of the EDC model is a sensitivity to the constants used in the model (Labahn et al., 2015). Therefore, given its success in simulating scramjet and ramjet combustion, and not relying on model constants in its formulation,

the PaSR combustion model will be used as the combustion model for this work.

### 3.8 Chapter Summary

In this chapter a high-level overview of the mathematical foundation to model turbulent combustion was presented. This includes the governing equations as well as some common simplifications that are used to reduce complexity and computational time. For turbulence, RANS models were discussed as feasible methods for modelling turbulence, with the  $k-\omega$  SST Model being used in this work. The modelling of the chemical reaction rate was discussed in Section 3.7. Basic chemistry kinetics was presented, as well as three mixing models which are commonly used to model turbulence-chemistry interaction. Of these three, the Partially Stirred Reactor Model was chosen as the chemistry model used here due its success in modelling high-speed combustion (such as in ramjets) and its ability to account for chemistry and mixing timescales effectively in turbulent combustion modelling.

# Chapter 4

## Numerical Model Description

This chapter contains a description of the methods used to obtain the results presented in this work. First, a brief description of the open-source software OpenFOAM, which was used here, is presented. Next, the methods of discretization for the various terms in the Navier-Stokes equations are presented. This includes the details of the implementation of the OpenFOAM solver used which allows the simulation of supersonic, multi-species, and reactive flows. Lastly, how mesh-sensitivity was assessed and quantified is discussed.

### 4.1 OpenFOAM

OpenFOAM (Open-source Field Operation and Manipulation) is a C++ software used for constructing numerical solvers to solve partial differential equations using the finite volume method. It was developed by Henry Weller and Hrvoje Jasak at Imperial College (Weller et al., 1998; Jasak, 1996), before becoming open-source in 2004. OpenFOAM features a wide range of numerical solvers for various applications including compressible/incompressible flow, reactive flows, and multi-phase flows. Furthermore, the code is structured to allow the user to modify or create a new solver if needed.

OpenFOAM includes many turbulence models and numerical schemes, allowing the user a significant amount of control throughout the simulation process. Additionally, it uses a face-based approach for the mesh structure and discretization methods, which allows for arbitrary polyhedral meshes. This makes the meshing of complex geometry easier, including ramjets and other aerospace engines. OpenFOAM also features many useful pre- and post-processing utilities and functions, which make the set-up and analysis of simulations more straight-forward. In this work, version v2012 of OpenFOAM was used for all cases.

## 4.2 Discretization

This section details the discretization schemes used in OpenFOAM in this work. The objective of discretization is transforming the governing conservation equations (detailed in Section 3.2) into a set of algebraic equations that can be solved (Moukalled et al., 2016). Each of these equations represents one of the cells/volumes in the computational domain. The discretization methods for each of the terms in the governing equations (such as the temporal, advective, and gradient terms) requires a different approach to model accurately and in a stable manner, and therefore each will be discussed in turn.

### 4.2.1 Temporal Discretization

Temporal discretization is required to model the transient terms in the governing equations and is responsible for the time evolution of the solution (Moukalled et al., 2016). If the user is interested in a steady-state solution this discretization is only required to maintain stability, while for unsteady problems the accurate solution at each time-step is required. In this work for transient unsteady simulations the implicit second-order backward scheme was used:

$$\frac{\partial \psi}{\partial t} \approx \frac{1}{\Delta t} \left( \frac{3}{2} \psi - 2\psi^0 + \frac{1}{2} \psi^{00} \right) \quad (4.1)$$

Note here that  $\psi^0$  refers to the value of a flow parameter at the previous time-step and  $\psi^{00}$  refers to the value at two previous time-steps. Additionally, time discretization schemes can be divided into explicit or implicit methods (Hirsh, 2007). In explicit methods the unknown flow variables at the new time are solved entirely from the values at previous times. This leads to a solution algorithm with a minimal number of arithmetic operations for each time-step, and therefore is easier to implement and takes less computational resources per time-step. However, explicit schemes have restrictions on the maximum time-step they can take while still remaining stable. In contrast, for implicit schemes the unknown flow variables at the new time depend on both the current unknown flow variables and the previously determined values. Consequently, implicit methods require more computational time to compute a single time-step but can take much larger time-steps than explicit methods.

For steady-state simulations, the first order implicit Euler method shown in Eq. 4.2 was used. Additionally, to accelerate convergence, local time stepping (LTS) was utilized. This method takes time steps of different sizes in different parts of the domain based on the local Courant-Friedrich-Levy (CFL) number, with larger time-steps being taken where the local CFL number is smaller.

$$\frac{\partial \psi}{\partial t} \approx \frac{1}{\Delta t} (\psi - \psi^0) \quad (4.2)$$

#### 4.2.2 Advection Discretization

A commonly-used compressible solver ‘rhoCentralFoam’ has been shown to accurately and efficiently model supersonic flows (Stoldt et al., 2021). However, it is incapable of simulating multiple species and reactions (Greenshields et al., 2009). In comparison, a third-party solver reactingPimpleCentralFOAM is able to simulate supersonic flows with multiple species and combustion and was therefore chosen for this work (Kraposhin et al., 2015, 2018). This solver is an extension of the hybrid-scheme solver pimpleCentralFoam which allows for combustion and multiple species (Kraposhin et al., 2015, 2018). Validation for pimpleCentralFOAM was conducted previously for two jet cases with compressibility effects and entrainment and was found to reasonably match experiment (Lastiwka et al., 2022). For the advective terms, these solvers use an incompressible flux formulation in regions of low Mach numbers (Kraposhin et al., 2015), while in regions of high compressibility the Kurganov-Tadmor (KT) (Kurganov and Tadmor, 2000) or the Kurganov-Noelle-Petrova (KNP) (Kurganov et al., 2001) algorithms are used. The properties of these algorithms are combined using a switch function, which chooses the flux calculation scheme based on the local Mach number (Kraposhin et al., 2015). This approach allows for the simulation of a flow containing a wide range of Mach numbers. The properties and definitions used in this approach are defined below.

As stated previously, reactingPimpleCentralFOAM uses a hybrid incompressible and KT/KNP scheme for the evaluation of the advective terms. The properties of these schemes are combined using a switch parameter shown in Eq. 4.3. This parameter is defined in terms of the local Mach number ( $M_f$ ) and the CFL number at a given face:

$$\kappa_f = \min \left( \frac{M_f}{CFL}, 1 \right) \quad (4.3)$$

The value of  $\kappa_f$  ranges from 0, in which the flux is calculated using an incompressible approach, and 1 in which the flow shows significant compressibility effects. Beginning with the incompressible approach, the advective flux calculation is given by:

$$\int_{\Omega} \nabla \cdot (\mathbf{U} \psi) dV \approx \sum_f (\mathbf{S}_f \cdot \mathbf{U}) \psi_f = \sum_f V_f \psi_f \quad (4.4)$$

where  $\psi$  is a flow parameter,  $f$  is the index for each face of a cell, and  $S_f$  is the product of a face normal vector and the face area as shown in Fig. 4.1. The calculation of the value of  $\psi_f$  is discussed in Section

#### 4.2.2.

When using a KT/KNP scheme, the flux of field  $\psi$  through a face can be represented as a weighted sum of the fluxes in the positive (in the direction of  $\mathbf{S}_f$ ) and negative directions (Kurganov and Tadmor, 2000; Kurganov et al., 2001). This flux must include the acoustic speed of disturbances as well as the velocity of the fluid (Kraposhin et al., 2015). The discretization is therefore (Greenshields et al., 2009):

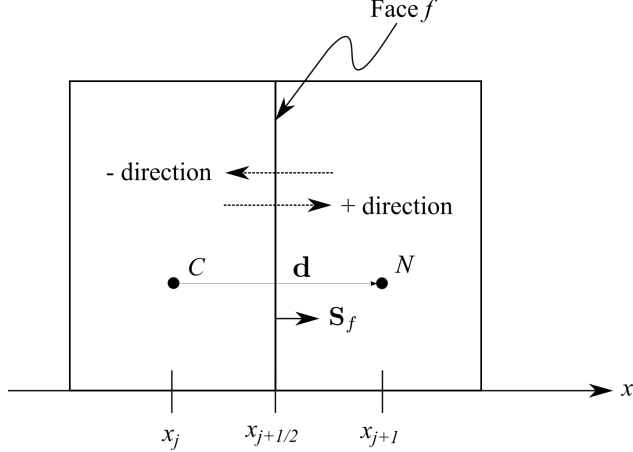


Figure 4.1: Schematic of finite volume cell for computation of fluxes (Lastiwka et al., 2022). Used with permission.

$$\sum_f V_f \psi_f = \sum_f [\alpha V_{f+} \psi_{f+} + (1 - \alpha) V_{f-} \psi_{f-} + \xi_f (\psi_{f-} - \psi_{f+})] \quad (4.5)$$

The KT method is a central scheme which applies equal weighting in the  $f_+$  and  $f_-$  directions and therefore uses a value of 1/2 for  $\alpha$  (Greenshields et al., 2009). In contrast, the KNP method is a central-upwind scheme that calculates  $\alpha$  from the one-sided local speeds of propagation as shown in Eq. 4.6. In this work only the KNP method was used. The value of  $\xi_f$  for the KNP scheme is given by Eq. 4.7.

$$\alpha = \frac{a_{f+}}{a_{f+} + a_{f-}} \quad (4.6)$$

$$\xi_f = \alpha (1 - \alpha) (a_{f+} + a_{f-}) \quad (4.7)$$

where  $a_{f+}$  and  $a_{f-}$  are the volumetric fluxes associated with the local speeds of propagation and are given by (Kraposhin et al., 2015):

$$a_{f+} = \max (c_{f+} |\mathbf{S}_f| + V_{f+}, c_{f-} |\mathbf{S}_f| + V_{f-}, 0) \quad (4.8)$$

$$a_{f-} = -\min (-c_{f+} |\mathbf{S}_f| + V_{f+}, -c_{f-} |\mathbf{S}_f| + V_{f-}, 0)$$

where  $c_{f\pm}$  are the speeds of sound at face  $f$  based on the flow entering or exiting the owner cell, and for an ideal gas is calculated as  $c_{\pm} = \sqrt{\gamma_{\pm}RT_{\pm}}$ . The mass fluxes in the hybrid scheme with the switching parameter  $\kappa_f$  are given by (Kraposhin et al., 2015):

$$\begin{aligned}\Phi_{f-} &= \kappa_f \alpha \rho_{f+} (V_{f+} + a_{f-}) \\ \Phi_{f+} &= (1 - \kappa_f) \alpha \rho_{f+} (V_{f+} + a_{f-}) + \rho_{f-} [(1 - \alpha) V_f - \alpha a_{f-}]\end{aligned}\tag{4.9}$$

### Interpolation of Cell-Center Values to Cell-Faces

For the KNP and incompressible schemes described previously, the values at the cell faces are required. In OpenFOAM, flow properties are stored at the cell-centers. Therefore, an interpolation scheme is needed to reconstruct the one-sided cell values on each side of the cell faces. This is often accomplished using a Monotonic Upstream-centered Scheme for Conservation Laws (MUSCL) type approach, which maintains second-order in smooth regions of the flow but will be first order near discontinuities such as shock-waves (van Leer, 1979). The flux on a cell face  $f$  is therefore, assuming flow is from cell  $C$  to cell  $N$  in Fig. 4.1, given by (Greenshields et al., 2009):

$$\psi_{f+} = (1 - g_{f+}) \psi_C + g_{f+} \psi_N\tag{4.10}$$

$$g_{f+} = \theta(r) (1 - \xi_f)\tag{4.11}$$

It is common to define the flux limiter  $\theta(r)$  such that it is total variation diminishing (TVD) (Greenshields et al., 2009). The aim of this is to reduce the spurious oscillations that can occur in higher-order schemes when convection is significant. This is accomplished by a blending between a central ( $\theta(r) = 1$ ) and a upwind/downwind ( $\theta(r) = 0$  or  $2$ , depending on the flow direction) interpolation. In this work, the van Albada interpolation scheme was used due to its satisfactory performance for high-speed aircraft (Stoldt et al., 2021). The flux limiter  $\theta(r)$  is therefore given by Eq. 4.12 (Stoldt, 2021), and the parameter  $r$  is defined in Eq. 4.13 (Greenshields et al., 2009). The vector  $\mathbf{d}$  connects cells  $C$  and  $N$  as shown in Fig. 4.1,  $(\nabla\psi)_C$  is the gradient of  $\psi$  at cell  $C$ , and  $(\nabla_{\mathbf{d}}\psi)_f$  is the difference between  $\psi_C$  and  $\psi_N$  scaled by the magnitude of  $\mathbf{d}$ .

$$\theta(r) = \frac{r + r^2}{1 + r^2}\tag{4.12}$$

$$r = 2 \frac{\mathbf{d} \cdot (\nabla \psi)_C}{(\nabla_{\mathbf{d}} \psi)_f} - 1 \quad (4.13)$$

### 4.2.3 Gradient Discretization

In OpenFOAM, there are two options for gradient discretization: the Green-Gauss or weighted least-squares method. When the Green-Gauss method is used, the first step is to transform the volume integral into a surface integral using the Divergence Theorem. This surface integral is approximated as the interpolated values of the fluid property  $\psi$  at each face centroid ( $\psi_f$ ), multiplied by their respective area vectors, as shown in Eq. 4.14. To obtain the final cell center gradient value, the result is then divided by the cell volume. For arbitrary meshes, the Green-Gauss method is zeroth-order accurate (Syrakos et al., 2017). However, for uniform Cartesian meshes it obtains second-order accuracy.

$$\int_{\Omega} \nabla \psi dV \approx \sum_f \mathbf{S}_f \psi_f \quad (4.14)$$

The least-squares method minimizes the following function to determine the gradient at each cell center (Moukalled et al., 2016):

$$G_c = \sum_f w_f [\psi_{N,f} - (\psi_C + \nabla \psi_C \cdot \mathbf{d}_f)]^2 \quad (4.15)$$

where  $w_f$  is a weighting function which is often chosen as the inverse of the distance to neighboring cell centers (Stoldt, 2021). The least-squares method is in general first-order for arbitrary meshes, but obtains second-order accuracy for locally-distorted grids (Syrakos et al., 2017). Due to its higher order, the weighted least-squares method was used in this work. Additionally, the cell-gradients were limited to ensure the final values of the gradient at the cell faces were bounded by the lower and upper limits of the neighbouring cells.

### 4.2.4 Laplacian Discretization

The Laplacian terms are discretized by first converting the volume integral to a sum of the gradient values at each face centroid multiplied by their respective areas (Stoldt, 2021; Lastiwka et al., 2022) as shown in Eq. 4.16. Note here that  $\Gamma$  refers to the diffusion constant for flow property  $\psi$ .

$$\int_{\Omega} \nabla \cdot (\rho \Gamma \nabla \psi) dV \approx \sum_f (\rho \Gamma \mathbf{S} \cdot \nabla \psi)_f \quad (4.16)$$

Following this, the product of the gradient and surface normal vector in Eq. 4.16 is approximated by two

terms: an orthogonal component and a non-orthogonal correction component (only the first component is needed for an orthogonal mesh), which are given by (Greenshields et al., 2009):

$$(\mathbf{S} \cdot \nabla \psi)_f \approx A_{ortho} (\psi_N - \psi_C) + \mathbf{a} \cdot (\nabla \psi)_f \quad (4.17)$$

$$A_{ortho} = \frac{|\mathbf{S}_f|^2}{\mathbf{S}_f \cdot \mathbf{d}} \quad (4.18)$$

$$\mathbf{a} = \mathbf{S} - A_{ortho} \mathbf{d} \quad (4.19)$$

### 4.3 Mesh Sensitivity

To assess mesh sensitivity, a least-squares procedure described by Eça and Hoekstra (2014) was used. For this method a series of at least three grids is used to determine an extrapolated value ( $\psi_0$ ) and a corresponding uncertainty. The method used for extrapolation to estimate the discretization error ( $\delta$ ) depends on the observed order of convergence ( $p$ ). In particular, the method selects an extrapolation method based on the following criteria:

1. If  $0.5 \leq p \leq 2$ , then  $\delta_{RE} = \alpha \Delta h_g^p$  is fit to the CFD results using both a weighted and non-weighted approach, where  $\Delta h_g$  is the typical cell size for the mesh and  $\alpha$  is a constant to be determined. Weighting applies larger value to the solutions obtained on finer meshes than coarser ones.
2. If  $p > 2$ , then  $\delta_1 = \alpha \Delta h_g$  and  $\delta_2 = \alpha \Delta h_g^2$  are fit to the CFD results using both a weighted and non-weighted approach.
3. If  $p < 0.5$  or not defined, then  $\delta_1 = \alpha \Delta h_g$ ,  $\delta_2 = \alpha \Delta h_g^2$ , and  $\delta_{12} = \alpha_1 \Delta h_g + \alpha_2 \Delta h_g^2$  are fit to the CFD results using both a weighted and non-weighted approach.

To select between the weighted and unweighted approach, as well as which fit is used between  $\delta_1$ ,  $\delta_2$ , and  $\delta_{12}$  in Cases 2 and 3, the fit resulting in the smallest standard deviation is used.

A benefit of this approach is it allows the estimation of uncertainty even when data is not in the asymptotic range, which can often only be achieved with impractical grid refinement (Eça and Hoekstra, 2014). Additionally, it is able to accommodate scatter present in the data which often occurs in practical problems due to sources such as the lack of geometrical symmetry for unstructured grids, damping functions, among others (Eça and Hoekstra, 2014). Therefore, this procedure was used for assessing mesh sensitivity in all cases.

## 4.4 Chapter Summary

This chapter outlined the discretization methods used for the temporal, advective, gradient, and Laplacian terms in the Navier-Stokes equations which were detailed in Chapter 3. A second-order accurate discretization scheme was used for all terms, with the exception of a first-order time discretization being used for LTS simulations. Additionally, a description of the implementation of the third-party OpenFOAM solver used in this work, reactingPimpleCentralFOAM (Kraposhin et al., 2015, 2018), was presented. Lastly, the method used to assess mesh sensitivity was discussed. This method applies a least-squares approach to determine an appropriate fit to the computational results, allowing for the determination of an uncertainty without necessarily reaching the asymptotic range of mesh convergence.

# Chapter 5

## Verification and Validation of Computational Model

This chapter details the verification and validation of the computational model when analyzing cases with combustion and multiple species. Since the motivation for this work is to understand turbulent combustion in an ejector-ramjet, three validation cases were considered, starting with simplicity and moving to complexity. In particular, these cases were a one-dimensional laminar flame, a bluff-body stabilized flame, and the AIS when operating under static conditions. The main objective here was to assess the accuracy and robustness of this solver when using the partially stirred reactor turbulence combustion model. These validation cases were chosen specifically to assess the effect of mixture composition and turbulence on the rate of reaction for cases relevant to an ejector ramjet.

### 5.1 One-Dimensional Laminar Flame Speed

The first case considered was a 1D premixed laminar flame. This case was chosen to verify that the solver is able to accurately model the chemistry and transport phenomena required for combustion given the assumptions detailed in Section 3.4 to reduce computational cost. Using a procedure similar to Cloney et al. (2018), the initial conditions were calculated using the Cantera package. The results were then mapped onto the domain used in OpenFOAM. Simulations were completed for both methane and propane combustion with equivalence ratios ( $\phi$ ) ranging from 0.6 to 1.3 with air with an assumed oxygen to nitrogen molar ratio of 1 to 3.76, respectively. The results from reactingPimpleCentralFOAM were then compared with Cantera and experimental data for assessment. Cantera is expected to be more accurate than reactingPimpleCentralFOAM

due its more detailed treatment of transport properties (see Section 3.5).

A detailed reaction mechanism which includes all intermediate reaction steps is expected to produce the most accurate results but with the largest computational cost. In this work, the most detailed reaction mechanisms used were the GRI-Mech 3.0 (GRI325) (Smith et al., 1999) and San Diego (SanDiego235, 2012) mechanisms for methane and propane combustion, respectively. These detailed mechanisms are computational feasible when applied to a one-dimensional flame implemented in Cantera. However, it is not computational feasible to include these detailed mechanisms when performing a large number of three-dimensional unsteady simulations. Therefore, one goal from this case study is to determine an acceptable level of error of the laminar flame speed when implemented in reactingPimpleCentralFOAM.

Skeletal mechanisms aim to provide similar accuracy to detailed mechanisms for key flame properties while reducing their computational cost. This is done by only including the most important reaction steps. The Z42 methane (Ehn et al., 2017) and Z66 propane (Zettervall et al., 2017) skeletal mechanisms were used in this validation study. Lastly, global mechanisms include a limited number of reactions and species but can predict flame properties such as the laminar flame speed with careful parametrization (Zettervall et al., 2017). These mechanisms have the lowest computational cost and are therefore commonly used in CFD. Two global mechanisms were used for methane combustion in this work: the one-step mechanism available with Cantera (MP1) (CERFACS, 2017) and the two-step mechanism developed by Franzelli et al. (2012) (BFER2). For propane combustion, the global Westbrook and Dryer two-step (WD2) (Westbrook and Dryer, 1981) mechanism was used. The chemical mechanisms used are summarized in Table 5.1.

Table 5.1: Chemical reaction mechanisms used in current work.

Fuel	Mechanism	Species	Reactions	Reference
Methane	MP1	5	1	CERFACS (2017)
Methane	BFER2	6	2	Franzelli et al. (2012)
Methane	Z42	18	42	Ehn et al. (2017)
Methane	GRI325	53	325	Smith et al. (1999)
Propane	WD2	6	2	Westbrook and Dryer (1981)
Propane	Z66	24	66	Zettervall et al. (2017)
Propane	SanDiego268	58	268	San Diego mechanism (2012)

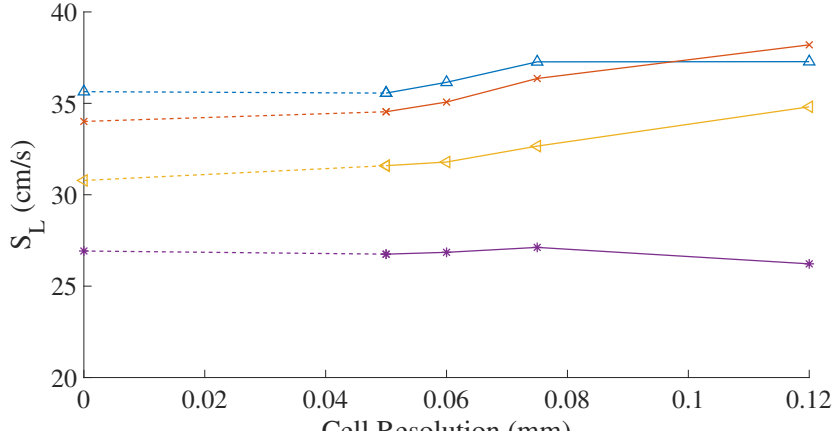
At the inlet, the species, velocity, and temperature were set with Dirichlet boundary conditions. The unburnt temperature was 300 K for all simulations and the Cantera results were used for the velocity and species inlet values. At the outlet, to prevent reflections a characteristic boundary condition ('waveTransmissive' in OpenFOAM, for more details see Poinsot & Lele, 1992) was used for pressure with a far-field value

of 100 kPa. All other boundary conditions were specified with a gradient equal to zero. Each simulation was a transient simulation modelling the flow for 0.03 s with a 6 cm domain length. The time-step chosen corresponded to a max CFL number of 0.1.

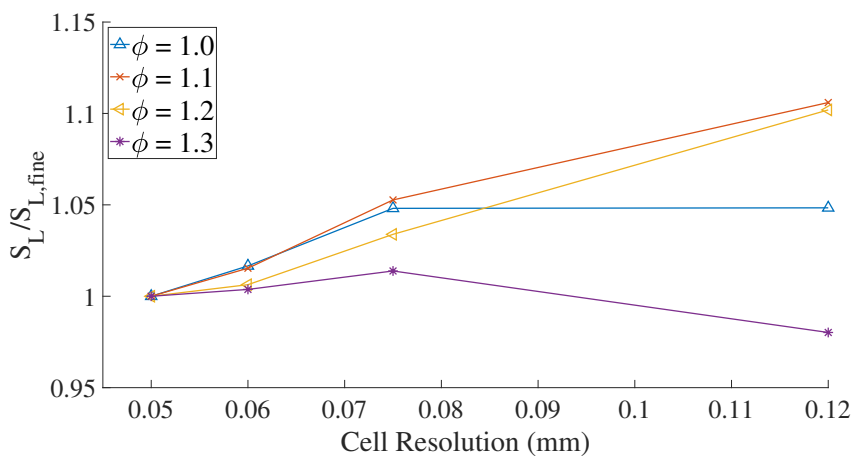
The laminar flame speeds ( $S_L$ ) were determined by measuring the distance the flame front (taken as the point in the flame with a temperature of 1000 K) travelled from 0.005 s to 0.03 s divided by the time elapsed (0.025 s). To assess mesh sensitivity, the results obtained using the Z42 mechanism at four equivalence ratios ranging from 1.0 to 1.3 were analyzed as various levels of mesh refinement. Only the Z42 mechanism was used for the mesh sensitivity study since as a skeletal mechanism it accounts for the most important chemical reactions and species while still maintaining a reasonable computational cost. It is therefore expected to be representative of the other chemical mechanisms and any effect chemistry has on mesh sensitivity should be captured. Fig. 5.1a shows the non-normalized flame speeds as well as the extrapolated value for each equivalence ratio. As seen in Fig. 5.1b, the flame speeds became reasonably mesh-independent when a cell resolution of 60  $\mu\text{m}$  was used (corresponding to 1000 uniform cells) and only differed by a maximum of around 2% upon further mesh refinement. A 60  $\mu\text{m}$  cell resolution was therefore used for all simulations. At this level of mesh refinement the largest uncertainty out of the four equivalence ratios was 6.2%.

The reactingPimpleCentralFOAM simulation results for methane and air combustion are shown in Fig. 5.2 along with results from Cantera simulations. When the GRI325 and Z42 mechanisms were used, Cantera was able to accurately predict the laminar burning velocity over the entire range of equivalence ratios. However, the one and two step mechanisms (MP1 and BFER2, respectively) were found to over-predict the burning velocity at higher equivalence ratios (above 1.1). The reactingPimpleCentralFOAM results were found to differ from the Cantera results. This is most apparent in the results for the GRI325 mechanism, which was found to be significantly lower than the Cantera and experimental results for stoichiometric and rich equivalence ratios. A reason for this discrepancy is likely the determination of transport properties in a global manner based on the temperature of the mixture of gases in reactingPimpleCentralFOAM compared to the mixture-averaged approach used in Cantera (see Sections 3.2 and 3.5). By comparing the effects of the simplifications for each transport property individually, Cloney (2018) found that the global approach used to calculate the mass diffusion constant, which uses a unity Schmidt number assumption, produced the largest error. Additionally, it resulted in a significant underestimation of the flame speed when skeletal and detailed mechanisms were used, which was observed here as well.

The results for propane and air combustion are shown in Fig. 5.3. Similar to the case for methane, when the Z66 or the SanDiego268 mechanism was used with Cantera the laminar burning velocity was generally accurately predicted. However, one notable difference is the burning velocity was over-predicted at lean equivalence ratios. The two step mechanism WD2 was found to under-predict the burning velocity at rich



(a)



(b)

Figure 5.1: Predictions of reactingPimpleCentralFOAM for methane-air laminar burning velocity for various cell resolution and equivalence ratios with the Z42 reaction mechanism. Fig. (a) shows the non-normalized results with the extrapolated values and (b) shows the normalized flame speeds (normalized with respect to the results from the finest mesh).

equivalence ratios, the opposite of what was observed for methane.

The results from both reactingPimpleCentralFOAM and Cantera shown here demonstrate that when one-step global or two-step mechanisms are used, only a portion of the burning velocity curve is accurately determined. Additionally, a significant qualitative feature, namely a maximum burning velocity occurring slightly above stoichiometric conditions, was not captured for methane or propane flames using these mechanisms. However, when using reactingPimpleCentralFOAM, increasing the complexity of the chemical mechanism was also shown to not necessarily provide more accurate results, as seen from the results of the GRI325 mechanism for methane and the SanDiego268 mechanism for propane. This suggests that a more detailed treatment of transport properties in addition to a more detailed chemical mechanism is needed to

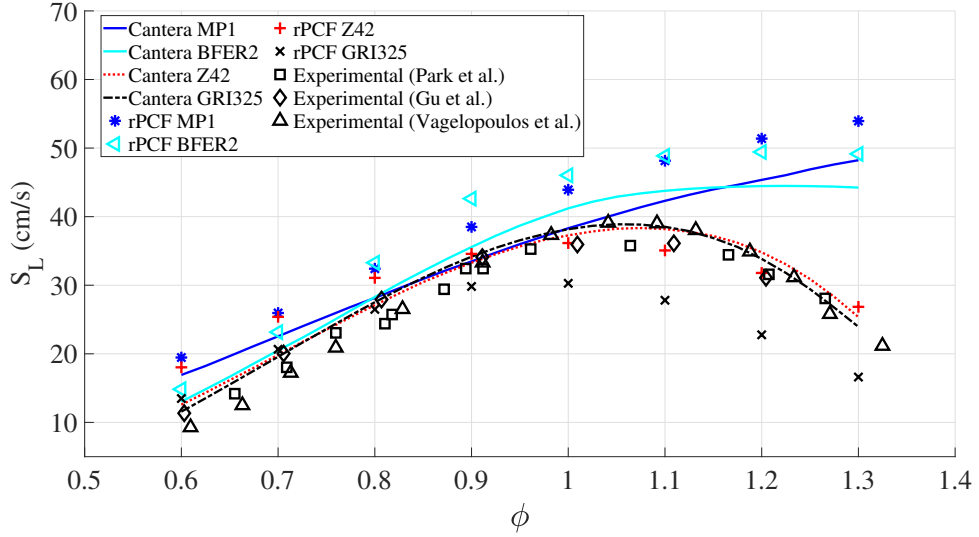


Figure 5.2: Predictions of reactingPimpleCentralFOAM (rPCF) for methane-air laminar burning velocity with different reaction mechanisms compared to experimental data and Cantera. Experimental data from Park et al. (2011), Gu et al. (2000), and Vagelopoulos et al. (1994).

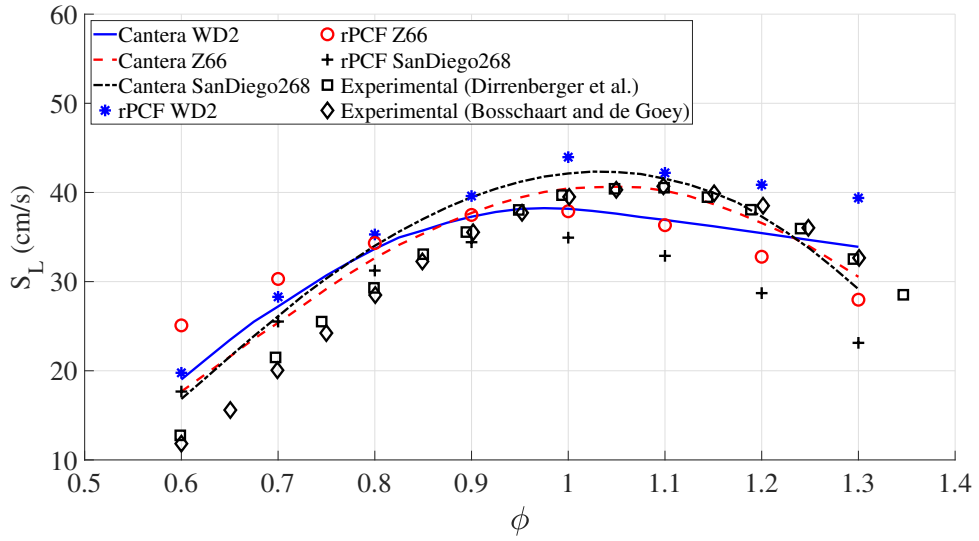


Figure 5.3: Predictions of reactingPimpleCentralFOAM (rPCF) for propane-air laminar burning velocity with different reaction mechanisms compared to experimental data and Cantera. Experimental data from Bosschaart and de Goey (2004) and Dirrenberger et al. (2011).

provide an accurate determination of the flame speed. However, this would likely lead to a prohibitive computational cost (Cloney, 2018). Similar results were obtained by Cloney et al. (2018), who used a modified version of the OpenFOAM solver coalChemistryFOAM to determine the laminar burning velocity and the structure of methane-air flames. Therefore, reactingPimpleCentralFOAM shows similar deficiencies to other available combustion solvers in OpenFOAM.

The bluff-body stabilized flame validation case which will be discussed in Section 5.2 consists of propane and air combustion at an equivalence ratio of 0.65. As seen in Fig. 5.3, at this equivalence ratio all three chemical mechanisms resulted in similar flame speeds in both reactingPimpleCentralFOAM and Cantera which were all higher than those observed experimentally. Therefore, due to providing similar accuracy at a substantially reduced computational cost, the WD2 chemical mechanism will be used for the bluff-body stabilized flame validation case. By comparing the reactingPimpleCentralFOAM results to experiment, the error for this mechanism at an equivalence ratio of 0.65 was estimated to be 52%.

While the bluff-body stabilized flame validation case consists of combustion at a single equivalence ratio, the AIS validation case (to be discussed in Section 5.3) will consider methane-air combustion over a wide range of equivalence ratios including both lean and rich combustion. As seen in Fig. 5.2, for the results obtained with reactingPimpleCentralFOAM only the Z42 chemical mechanism reasonably matched experiment at stoichiometric and rich equivalence ratios. It will therefore be used in this work for all AIS simulations. Again by comparing the reactingPimpleCentralFOAM results to experiment, the error for this mechanism was largest at an equivalence ratio of 0.6 with a value of 56%, however it decreases to 5% and 12% at equivalence ratios of 1.0 and 1.3, respectively.

## 5.2 Bluff-body Stabilized Flame

Flameholders are a key component of the combustor section in many propulsion systems, including ramjets, scramjets, and turbojets (Ebrahimi, 2006). The aim of a flameholder is to provide a robust region of recirculation, thus anchoring the flame in place in the combustor (Lovett et al., 2004). Additionally, they increase the combustion efficiency by uniformly spreading the flame. Given their importance to achieve efficient combustion in propulsion systems, in this work the capability of reactingPimpleCentralFOAM to capture flameholding behaviour accurately was assessed. This was accomplished by comparing simulation to experimental results obtained for a bluff-body stabilized flame studied by Sjunnesson et al. (1991; 1992) with data available online (APAN, 2018).

The experimental apparatus consists of a straight channel with a rectangular cross-section, divided into three sections: an inlet section, a combustor section, and a round exhaust as shown in Fig. 5.4. Gaseous propane was injected in the inlet section and mixed with air, resulting in premixed fuel and air entering the combustor section with an equivalence ratio of 0.65. A honeycomb screen was used to control the turbulence level. Following this screen the turbulence intensity from the experiments was estimated to be 3% (Zettervall et al., 2017). The domain and boundary conditions used can be seen in Fig. 5.4. Transient Reynolds-Averaged Navier-Stokes (RANS) simulations were used with the  $k - \omega$  SST turbulence model.

Transient simulations were used rather than steady-state due to the unsteady vortex shedding and acoustic behaviour observed both experimentally (Sjunnesson et al., 1991, 1992) and numerically (Ghani et al., 2015).

Each simulation was divided into three phases: a cold-flow run to develop the flow field, an ignition run which used an enthalpy source behind the bluff-body to initiate combustion, and a combustion run for which the ignition enthalpy source was turned off. The combustion run was used to develop the flame front, and once it was stable data was averaged over approximately four flow through times. This corresponds to 0.26 s, which was observed to be enough time for the average flow variables to become constant. The time step was limited to ensure the max CFL number was 0.25.

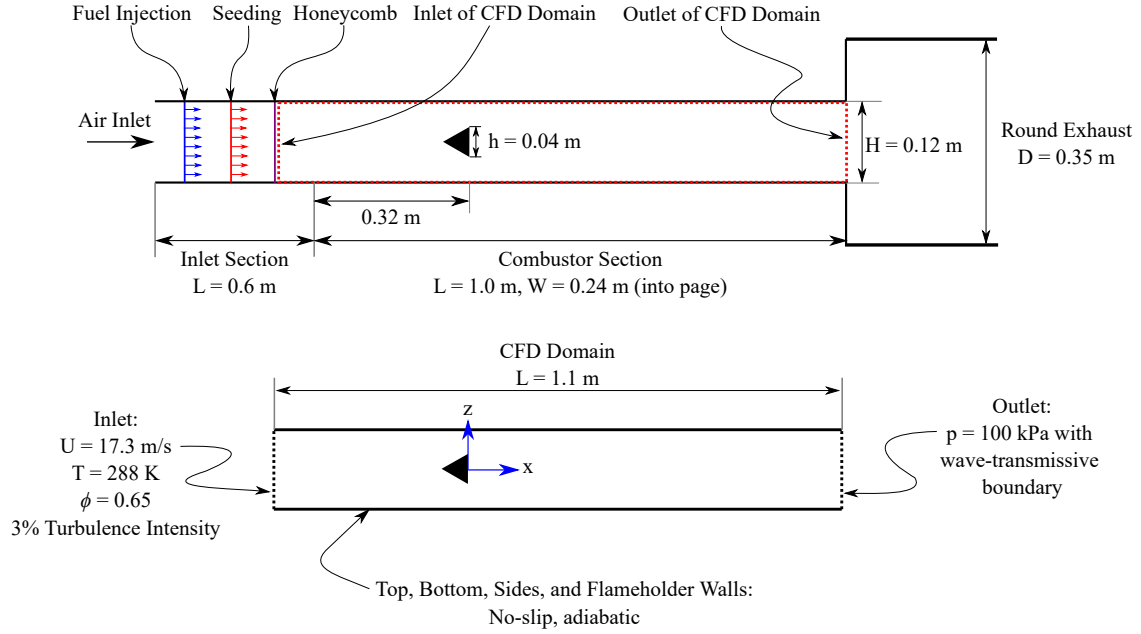


Figure 5.4: Schematic of the validation apparatus with domain and boundary conditions for CFD analysis. Modified from (Zettervall et al., 2017)

As discussed in Section 5.1, the WD2 two-step mechanism was used due to its low computational cost while still providing comparable results to more detailed mechanisms for the laminar burning velocity at an equivalence ratio of 0.65 (see Fig. 5.3). The error for this mechanism at this equivalence ratio was estimated to be 52%. Turbulence-chemistry interaction was modelled using the PaSR model defined in Eq. 3.74. Two cases were examined, one used the mixing time-constant  $\tau_{m,orig}$  defined in Eq. 3.81 and the other used  $\tau_{m,mod}$  defined in Eq. 3.80. The value of  $C_{mix}$  for  $\tau_{m,orig}$  was estimated to be 0.36 based on the properties in the recirculation zone behind the bluff-body. These properties were found from a simulation of this case

without combustion.

To reduce computational cost, the boundary layer on the duct and flameholder was not resolved and instead used a Launder-Spalding wall-modelled approach (Bredberg, 2000). This allows for much larger cells in the near-wall region. While the flow separates on the downstream side of the flame holder, there are fixed separation points dictated by the flameholder geometry. Therefore, the simplification of using wall functions does not affect the separation location and is expected to have a minimum effect on the overall results. The Launder-Spalding wall-modelled method can be summarized as: first solving the momentum equation with a modified effective viscosity, then solving the turbulent kinetic energy with a modified production and dissipation term, and lastly  $\omega$  is set using the calculated value of  $k$ . More details of the wall-modelled approach are available in Bredberg (2000).

To assess mesh sensitivity, the averaged axial velocity and temperature results obtained using four three-dimensional unstructured meshes were used. The number of elements ranged from 4,168,173 elements for the coarsest mesh ('Mesh 1') to 11,235,896 for the finest mesh ('Mesh 4'), with a refinement ratio of approximately 1.4 between meshes. Fig. 5.5 shows Mesh 1 along the center-line of the duct. The results for axial velocity and temperature of all four meshes including the extrapolated values are shown in Figs. A.1 and A.4, respectively. The resulting uncertainty for the averaged axial velocity for Meshes 3 and 4 are shown in Figs. A.2 and A.3, respectively. Note that the origin is located on the down-stream face of the bluff-body and the distances are normalized by the length of one side of the triangular bluff body ( $h$ , equal to 0.04 m). It can be seen that further mesh refinement narrowed the uncertainty band slightly for the first three-stations, but did not significantly affect the uncertainty for the last two stations. Figs. A.5 and A.6 show the uncertainty for the averaged temperature profiles. Again we see only a slight reduction in uncertainty with mesh refinement. Given that the uncertainty did not significantly change between Meshes 3 and 4, Mesh 4 was selected for further analysis.

The averaged results obtained using reactingPimpleCentralFOAM as well those from experiment are shown in Figs. 5.6 to 5.10. Additionally, results obtained by Ghani et al. (2015) using a two-step reaction mechanism with LES are shown for the axial and transverse average and RMS velocities. These LES results were obtained for a mesh with 20,919,678 elements using the AVBP LES solver (Schonfeld and Rudgyard, 1999) with the Sigma model being used to model the sub-grid stress tensor. For combustion and turbulence interaction, the dynamic thickened flame model was used.

When the results from the simulations using the two mixing timescales are compared, clear differences are observed. For the averaged axial velocity profiles shown in Fig. 5.6, the modified mixing timescale produced more accurate results further downstream from the bluff-body. At an  $x/h$  position of 9.4, the default OpenFOAM mixing scale resulted in a significant over-prediction of the velocity magnitude and the

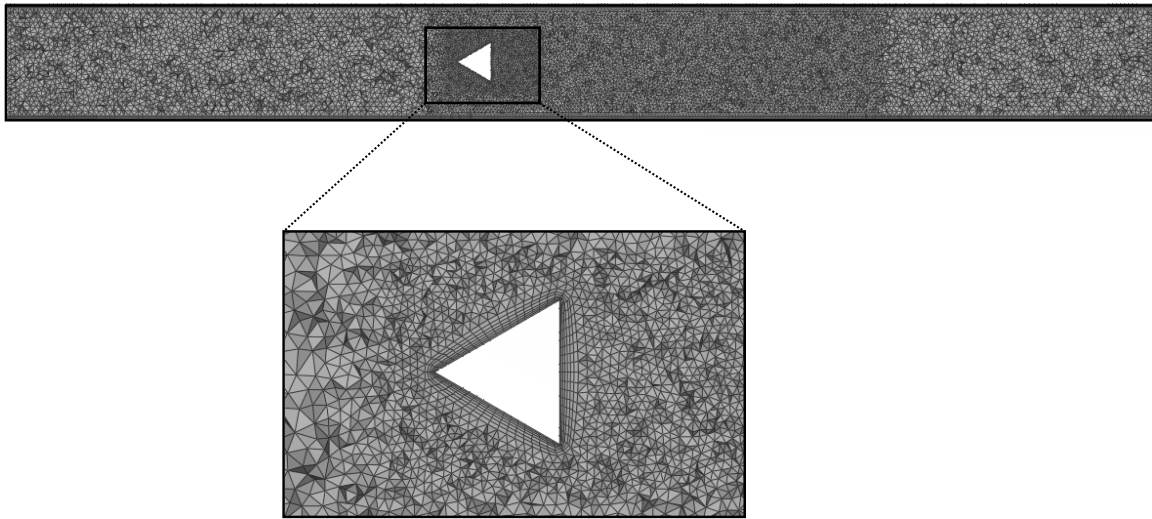


Figure 5.5: Mesh 1 used in the Bluff-body Stabilized Flame Validation Case.

profile did not agree with experiment. In contrast, the modified mixing scale resulted in a reasonable match in velocity magnitude and profile at an  $x/h$  position of 9.4. Furthermore, at axial positions of 1.53 and 3.75 the results of both simulations over-predicted the velocity along the center of the channel (near a  $y/h$  of 0), but this difference was larger when the default mixing timescale was used. In comparison, the LES predictions from Ghani et al. (2015) more closely matched experiment at  $x/h$  of 3.75, but was similar to the RANS results with the modified mixing scale at the other axial locations.

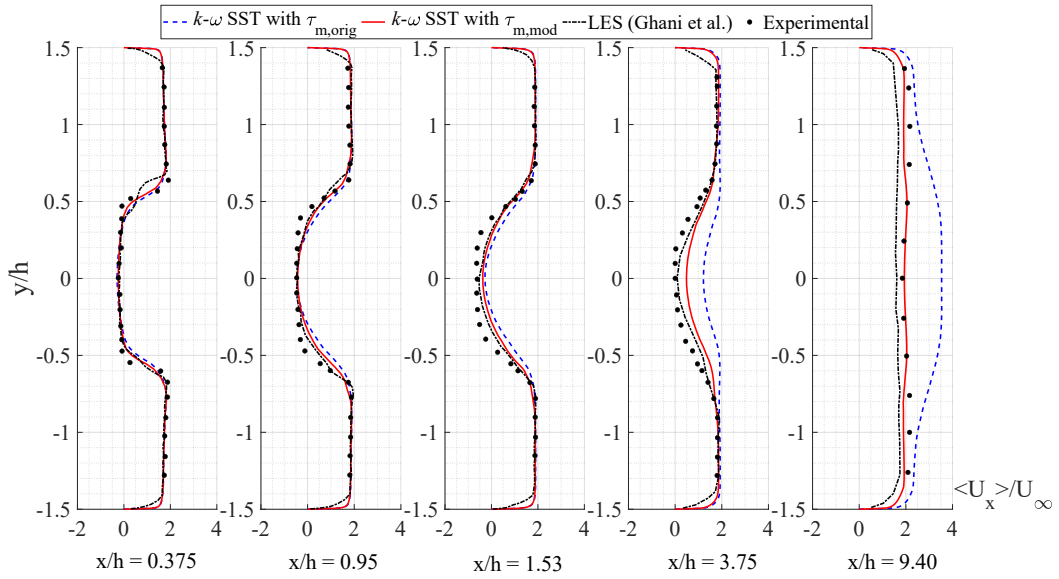


Figure 5.6: Time-averaged axial-velocity profiles. The velocities have been normalized by the free-stream velocity of 17.3 m/s. LES results obtained by Ghani et al. (2015) are shown for comparison.

While the reactingPimpleCentralFOAM and experimental results generally matched well for the axial velocity, the averaged transverse velocity profiles shown in Fig. 5.7 show less favourable agreement. The transverse locations which differed the most were at  $x/h$  positions of 0.95 and 1.53. This is likely due to the recirculation zone behind the bluff body being incorrectly predicted. Furthermore, as seen in Figs. 5.8 and 5.9, comparison with the experimental axial and transverse RMS values shows that the velocity fluctuations are generally over-predicted using reactingPimpleCentralFOAM with the  $k - \omega$  SST turbulence model. This differs from previous RANS results obtained by Olovsson (1992) using the  $k - \epsilon$  turbulence model which under-predicted the axial velocity RMS values. In contrast, the LES results from Ghani et al. (2015) show closer agreement to experiment particularly near the center-line. However, some notable exceptions are the significant over-prediction of the axial RMS values at a  $x/h$  position of 9.40, as well as the over-prediction of the RMS values near the wall (at  $y/h$  values around  $\pm 1$ ).

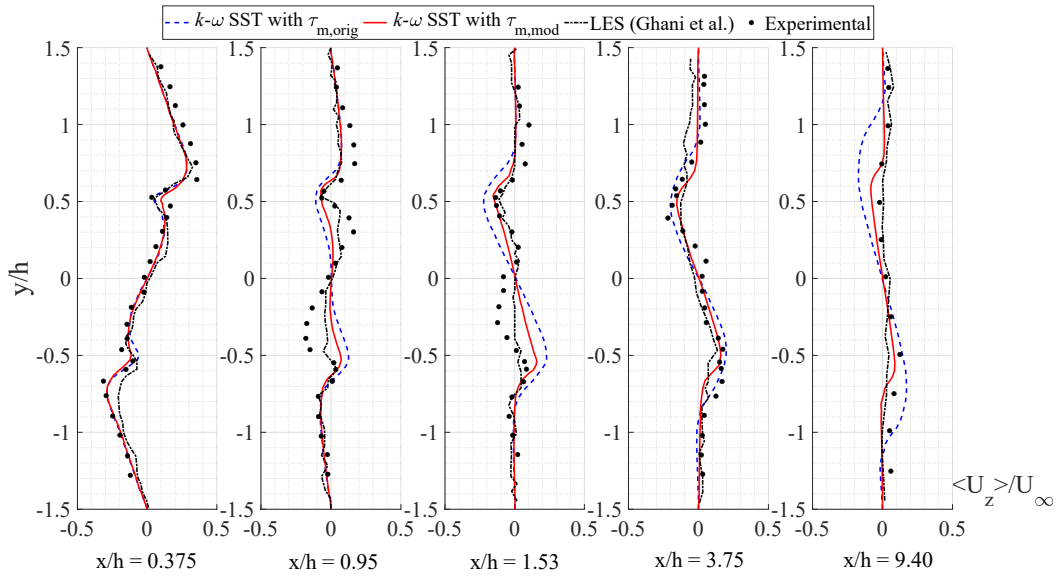


Figure 5.7: Time-averaged transverse-velocity profiles. The velocities have been normalized by the free-stream velocity of 17.3 m/s. LES results obtained by Ghani et al. (2015) are shown for comparison.

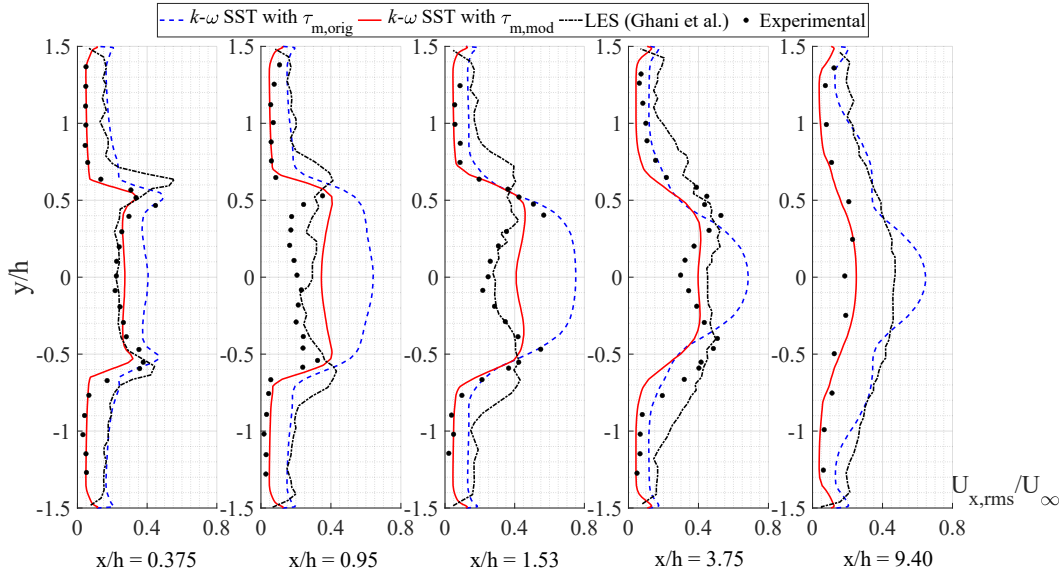


Figure 5.8: Time-averaged axial RMS velocity profiles. The velocities have been normalized by the free-stream velocity of 17.3 m/s. LES results obtained by Ghani et al. (2015) are shown for comparison.

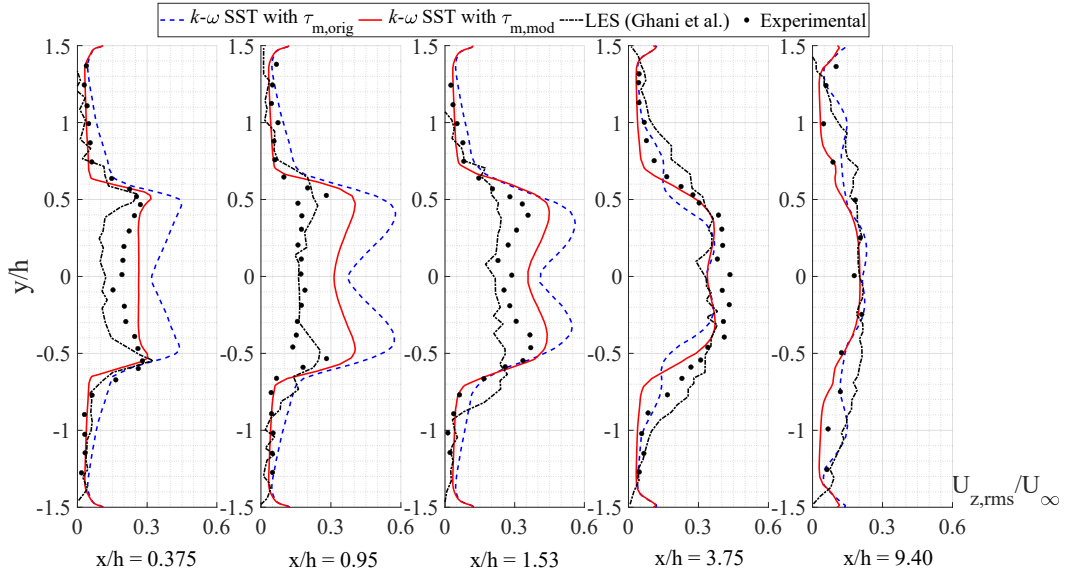


Figure 5.9: Time-averaged transverse RMS velocity profiles. The velocities have been normalized by the free-stream velocity of 17.3 m/s. LES results obtained by Ghani et al. (2015) are shown for comparison.

Fig. 5.10 shows the averaged temperature profiles at three axial locations including experimental results. Unfortunately, Ghani et al. (2015) did not report temperature profiles from their LES results. In the ultimate goal of assessing reactingPimpleCentralFOAM for predicting turbulent combustion in ramjets, the temperature predictions are key. The temperature profiles at  $x/h$  positions of 8.75 and 13.75 show the width of the flame brush is under-predicted with reactingPimpleCentralFOAM when the modified-mixing timescale was used. Conversely, the default timescale resulted in a flame brush wider than what was observed experimentally. Additionally, while the flame temperature matches well with experiment at  $x/h$  of 3.75, further downstream the reactingPimpleCentralFOAM results are higher than those from experiment. A possible reason for this difference is the WD2 mechanism not capturing intermediate reaction species and radical formation as the reaction progresses over time (Zettervall et al., 2017).

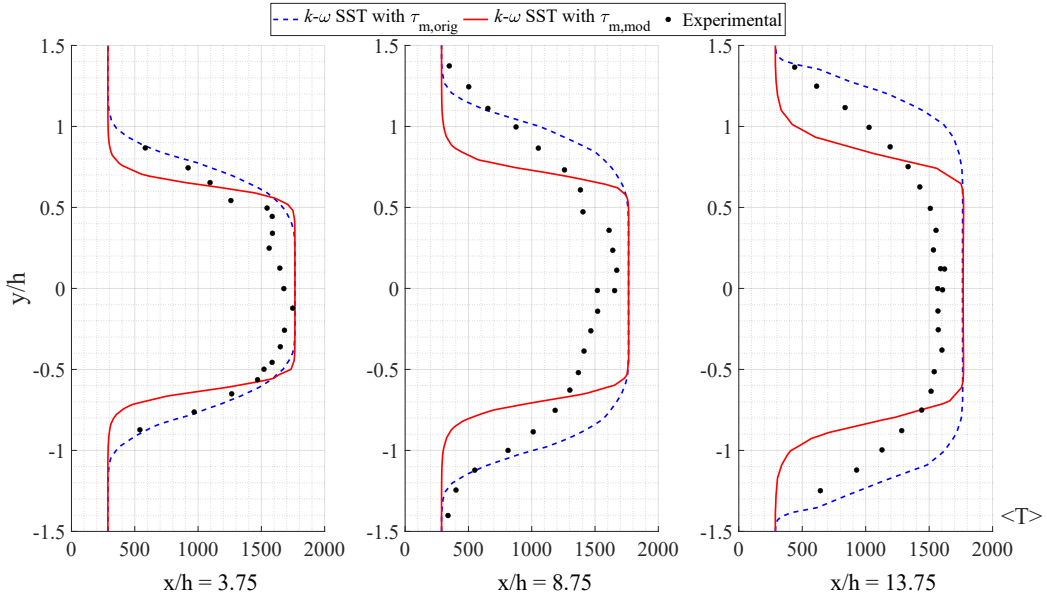


Figure 5.10: Time-averaged temperature profiles.

### 5.3 Ejector Ramjet

The final validation case in this work compares results from reactingPimpleCentralFOAM to those obtained experimentally for an ejector ramjet (Long et al., 2022). These results were obtained at the Rothney Advanced Propulsion Technology Research (RAPTOR) Laboratory, which was developed to experimentally investigate novel high-speed propulsion systems. The goal of these tests were to assess the feasibility of the AIS ejector ramjet at static conditions including its ability to produce thrust.

The geometry of the AIS ejector ramjet is shown in Fig. 5.11. The diameter of the jet ( $D_j$ ) was equal to 0.00635 m (0.25 inch), the mixing chamber diameter ratio ( $D_m/D_j$ ) was equal to 8, the diffuser half-angle was 3 degrees, the combustion chamber diameter ratio ( $D_c/D_j$ ) was equal to 32, and the nozzle exit diameter ( $D_n$ ) was equal to 0.154 m. The domain and boundary conditions are shown in Fig. 5.12. The jet exits the nozzle at approximately Mach 2 with a stagnation temperature of 293 K. This jet is responsible for entraining ambient air. Due to the axi-symmetry of the domain, only a 5 degree wedge was used for all simulations. No preheating of the fuel jet (shown schematically in Fig. 1.1) was considered for this case.

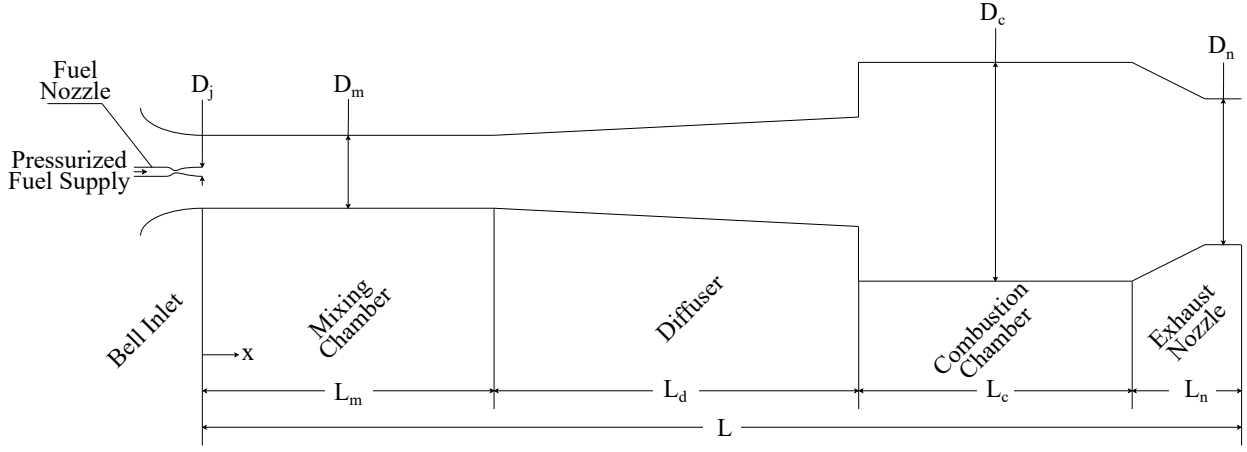


Figure 5.11: Schematic of AIS ejector ramjet. From (Long et al., 2022).

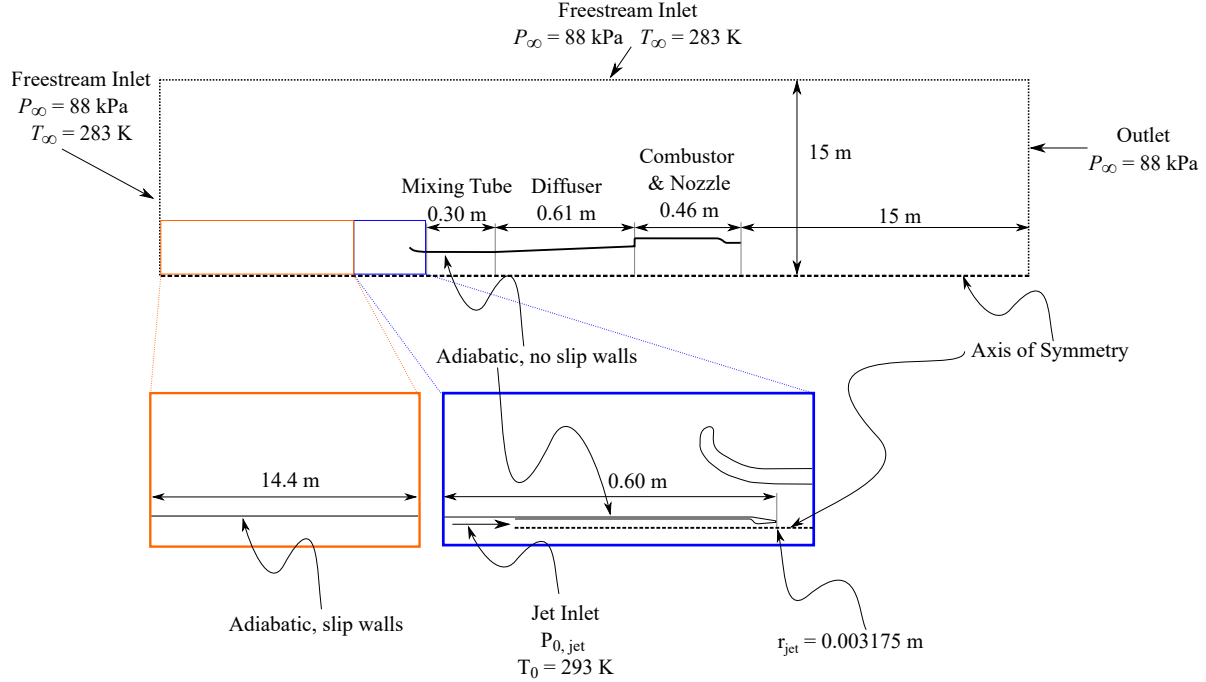


Figure 5.12: Domain and boundary conditions for the AIS validation case (Long et al., 2022), not to scale.

As seen in Fig. 5.12, at the free-stream inlet the total pressure and temperature were set to values of 88 kPa and 283 K, respectively. These conditions match those from experiment (Long et al., 2022). At the outlet, pressure again had a total pressure of 88 kPa but the gradient for temperature was set to zero. Three values of the stagnation pressure of the jet ( $P_{0,jet}$  in Fig. 5.12) were considered: 200, 400, and 900 kPa. These values were chosen to verify that the computational model is able to accurately capture the

performance of the AIS under a range of operating conditions.

The domain was extended 15 m from the engine in all directions, corresponding to approximately 100 times the size of the engine outlet diameter. Spalart and Rumsey (2007) recommend a domain size of at least 50 times the characteristic length for three-dimensional wing simulations. However, this recommendation was not devised for cases with combustion, so the domain size was doubled compared to this recommended value.

Adiabatic, no-slip walls were used for the interior of the engine, as well as the inlet and the interior of the fuel-nozzle. However, the no-slip wall for the lower section of the inlet (the exterior wall of the fuel-nozzle) only extended 0.60m upstream from the nozzle exit (as shown in the blue box in Fig. 5.12) which matches the length of the inlet section used in experiment. From the end of the no-slip wall upstream to the bottom-left corner of the domain a slip wall was used. The length of this slip wall was therefore 14.4 m, as shown in the orange box in Fig. 5.12. A slip wall was used to prevent unrealistic vertical flow upstream of the engine (which would not match experimental conditions) without causing excessive frictional losses. Throughout the inside of the engine the boundary layer was resolved with an average  $y+$  value of 0.37. This was done to improve the accuracy of the prediction of viscous and pressure forces on the engine, particularly in regions of recirculation. In contrast, wall-functions can be significantly inaccurate in predicting these forces particularly in flows with recirculation (Bredberg, 2000). However, on the outside of the engine a wall-modelled approach was used to reduce computational cost. Given the low ambient air velocity for the static engine case this was not expected to affect the results significantly.

Turbulence was again modelled using the  $k - \omega$  SST turbulence model. For combustion, given the wide range of equivalence ratios expected as the jet stagnation pressure is varied from 200 to 900 kPa, the Z42 mechanism for methane-air combustion was used. This reaction model was chosen due to its reasonable match to the laminar burning velocity at both lean and rich equivalence ratios (see Fig. 5.2). Turbulence-chemistry interaction was again modelled using the PaSR model. Given its better performance for the bluff-body stabilized flame validation case (see Section 5.2), the mixing timescale  $\tau_{m,mod}$  defined in Eq. 3.80 was used.

To reduce simulation time, local time-stepping (LTS) was first used for time discretization. However, large variations in thrust and entrainment were observed, indicating significant transient effects. Therefore, each simulation was divided into three stages: a cold flow run with no reactions, an ignition run which used an enthalpy source in the combustion chamber to simulate the spark which was used in the experiment, and a run with no enthalpy source to develop the combustion flow field and collect data. LTS was used for the cold run and it was ran until the mass flow rates of the inlets/outlets reached a steady or clear repeating cycle. In previous work by the author, LTS was also used during the ignition run (Migadel et al., 2023).

However, it was later found that this led to an nonphysical flame front and a significant under-prediction of the thrust. Therefore in this work the ignition run used a fully transient time discretization rather than LTS. After the ignition run, all simulations were then ran transiently until a clear repeating pattern in the variables of interest (thrust, entrainment, mass flow rates, etc.) were observed and the values were averaged over 10 periods of the observed pattern. This resulted in an averaging period of approximately 0.04 to 0.06s, depending on the mesh and jet stagnation pressure, which corresponds to approximately 3 flow through times.

A hybrid structured-unstructured mesh was used for all AIS cases. A structured mesh was used inside the engine and near the inlet, while an unstructured mesh was used on the external side of the engine and towards the far-field. This was done to increase the refinement in regions of interest without requiring an excessive number of elements. Mesh 1 (the coarsest mesh used in the mesh-sensitivity study) is shown as an example in Fig. 5.13. All other meshes were of the same form with uniform refinement in all directions.

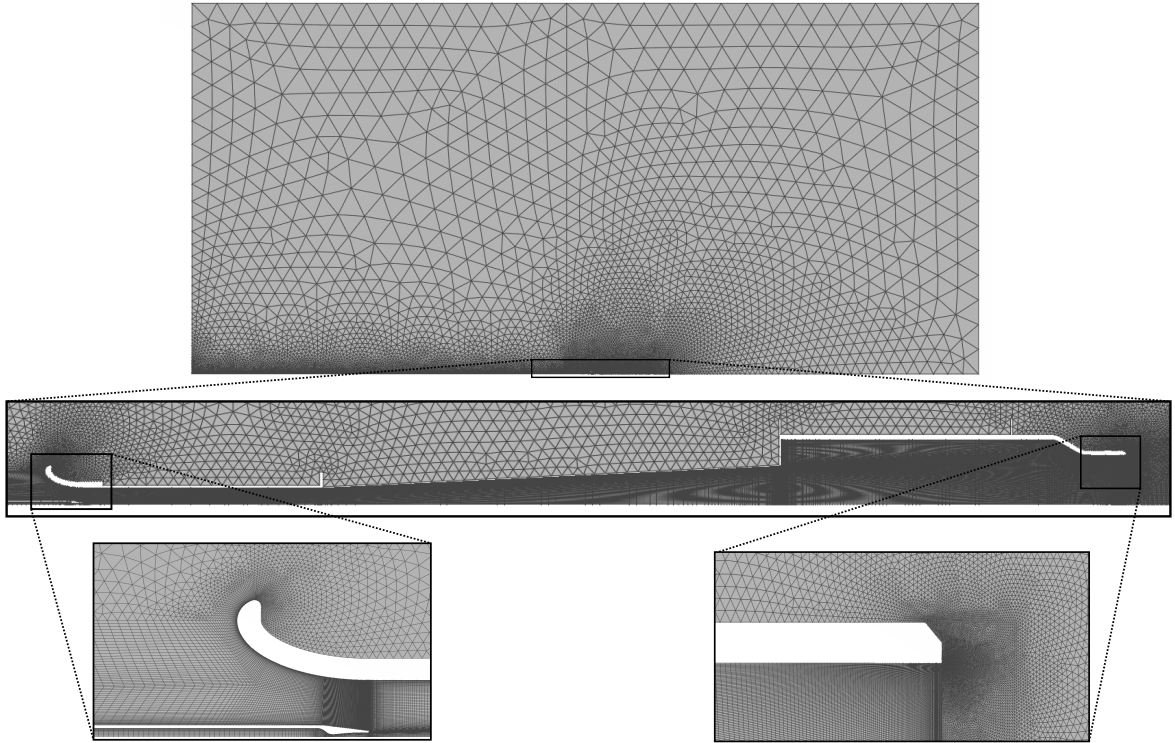


Figure 5.13: Mesh 1 used in AIS Validation Case.

To assess mesh sensitivity, four meshes were used with a mesh refinement ratio of approximately 1.5, as shown in Table 5.2. Additionally, the PaSR model with the modified mixing timescale ( $\tau_{m,mod}$ , defined in Eq. 3.80) and the default chemical timescale used in OpenFOAM (given in Eq. 3.76) was used for all four meshes. For the mesh sensitivity study, only the 400 kPa jet stagnation pressure was considered. As can be

seen, entrainment was found to increase with mesh refinement, while the thrust for the AIS ( $F_{AIS}$ ) increased until Mesh 3 and then decreased with Mesh 4. The AIS thrust consists of only the sum of the net viscous and pressure forces on the body of the engine. It does not include the thrust produced from the fuel jet.

Table 5.2: CFD results for thrust and entrainment for all meshes used in the AIS mesh sensitivity study. The thrust includes only the pressure and viscous forces on the body of the engine and does not include the thrust produced from the fuel jet.

Mesh Attribute or $\psi$	$\psi_1$	$\psi_2$	$\psi_3$	$\psi_4$
Number of Elements	231,422	338,379	504,117	755,531
$\omega$	17.8	18.5	20.8	23.1
$F_{AIS}$ (N)	7.7	9.7	10.9	10.6

The results of the mesh sensitivity study including the estimated uncertainties are shown in Table 5.3. It can be seen there is a continual reduction in uncertainty in entrainment with mesh refinement. However, for the AIS thrust there is a slight increase in uncertainty when Mesh 4 is used compared to Mesh 3. Therefore, given that the uncertainty in thrust did not decrease with further mesh refinement, and given the substantial increase in computational cost required for Mesh 4, Mesh 3 will be used for all further analysis of the AIS.

Table 5.3: Extrapolation method, extrapolated value, and resulting uncertainty for thrust and entrainment.

$\psi$	Extrapolation Method	$\psi_0$	$U_\psi(\psi_1)$	$U_\psi(\psi_2)$	$U_\psi(\psi_3)$	$U_\psi(\psi_4)$
$\omega$	$\delta_{RE,w}$	25.3	11.6	10.9	7.5	4.7
$F_{AIS}$ (N)	$\delta_{2,w}$	12.3	7.9	4.8	3.3	3.6

In this work, both the default ( $\tau_c$ , defined in Eq. 3.76) and modified expressions ( $\tau_{c,r}$ , defined in Eq. 3.78) for the chemical timescale were used and compared. This was done to determine which provides results that better match experiment. Figure 5.14 shows the averaged temperature, pressure, velocity magnitude, and progress variable ( $\theta$ ) in the combustion chamber when the default chemical timescale was used. In this work, the progress variable was calculated as shown in Eq. 5.1. Here  $Y_{CO_2}$  is the mass fraction of CO<sub>2</sub> and  $Y_{CO_2,max}$  is a constant determined for each simulation equal to the mass fraction of CO<sub>2</sub> when the reaction is complete. This constant is therefore given by the maximum value of  $Y_{CO_2}$  in the flow following combustion.

$$\theta = \frac{Y_{CO_2}}{Y_{CO_2,max}} \quad (5.1)$$

When the jet stagnation pressure was 900 kPa, combustion was not sustained in the combustion chamber which also occurred in the experiment (Long et al., 2022). For both the 200 and 400 kPa cases combustion was not observed along the center-line of the engine, with the 400 kPa case having a larger region where combustion did not occur. Due to this larger non-combustion region, the velocity magnitude for the 400 kPa case is much higher near the engine walls where combustion occurred compared to the 200 kPa case which had a more uniform velocity field at the engine's exit. Additionally, as expected from the higher jet stagnation pressure, a higher pressure was observed in the combustion chamber for the 400 kPa case compared to the 200 kPa one.

For comparison, Fig. 5.15 shows the results when the modified chemical timescale was used with jet stagnation pressures of 200 and 400 kPa (the cases with combustion). In running these cases, a similar method was used as for the default timescale. Namely, the same boundary conditions were applied as shown in Fig. 5.12, and as discussed previously each case was split into a cold flow stage with no reactions, an ignition stage which used an enthalpy source in the combustion chamber, and a stage with no enthalpy source to develop the combustion flow field and collect data. However, it was observed that during the stage with no enthalpy source following ignition the flame began to travel through the diffuser and eventually reached the mixing tube. This was not observed experimentally. Since the steady-state operation was of interest, a method of preventing this unwanted startup transient was devised. Following ignition, the reaction rates were artificially suppressed by a factor of 0.5 until the simulation reached steady state. At that point, the suppression of reaction rates was deactivated and then the simulation was continued until steady operation was observed again. Following this collection of statistics were performed. It was found that the reaction did not progress upstream into the mixing tube when following this method. However, the unwanted transient behavior observed during startup indicates that the chemical timescales could be underpredicted by the modified model during ignition.

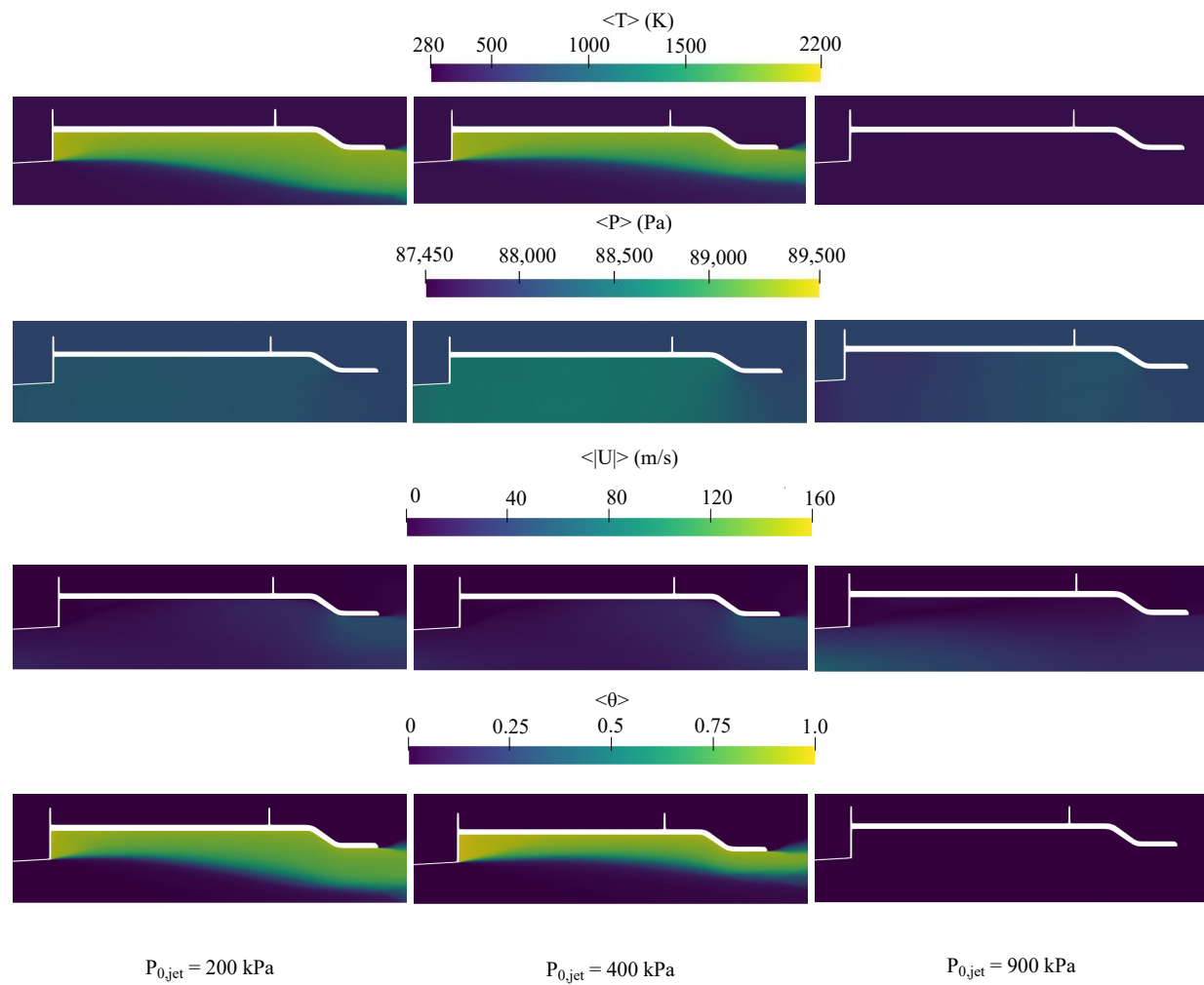


Figure 5.14: Averaged temperature, pressure, velocity magnitude, and progress variable in the combustion chamber for 200, 400, and 900 kPa fuel jet stagnation pressures. Results were obtained using the PaSR combustion model with the default chemical timescale.

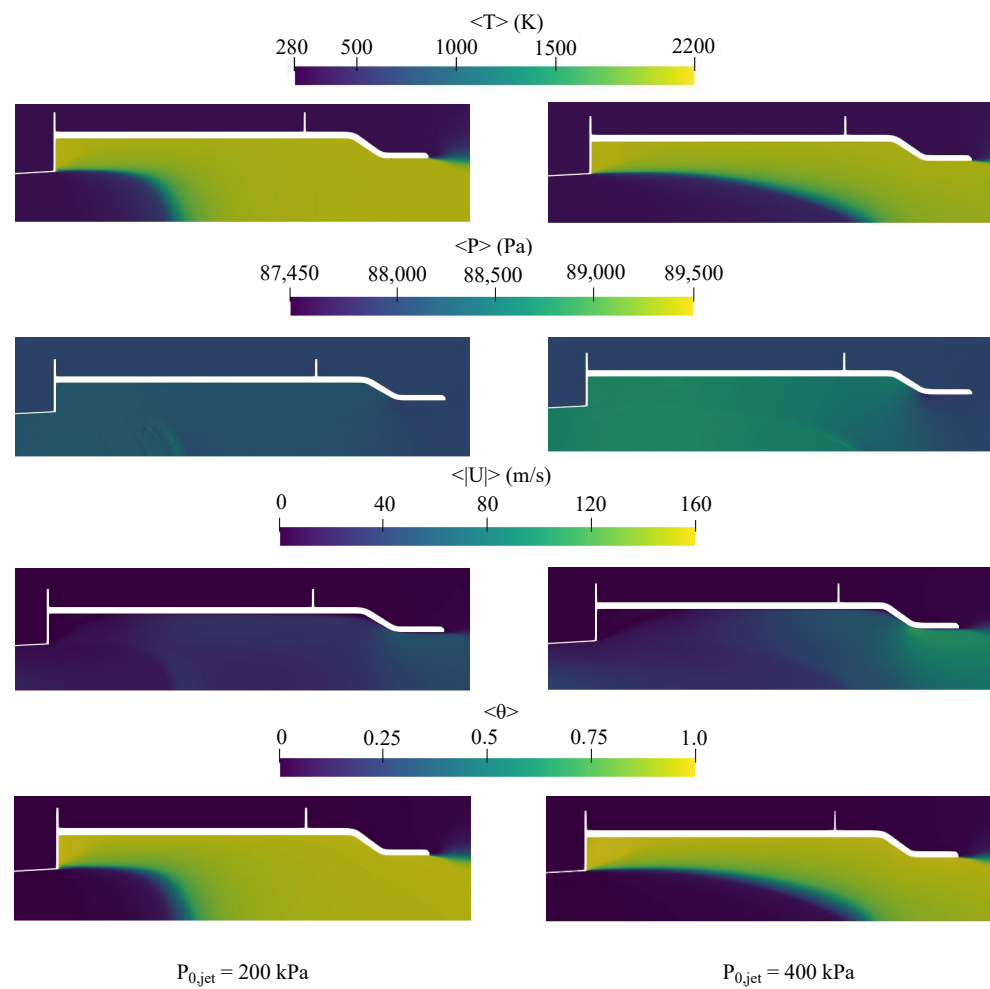


Figure 5.15: Averaged temperature, pressure, velocity magnitude, and progress variable in the combustion chamber for 200 and 400 kPa fuel jet stagnation pressures obtained using the PaSR combustion model with a modified chemical timescale.

By comparing Fig. 5.15 to Fig. 5.14, a major difference between results of the modified and default chemical timescales is the size of the region near the center-line of the engine where combustion did not occur. In both the 200 and 400 kPa cases, this region was much smaller for the modified timescale compared to when the default one was used and all incoming fuel and air combusted before leaving the engine. This also resulted in the velocity magnitude being much more uniform at the engine exit for both pressures. Another difference is the averaged pressure, which was slightly larger in the combustion chamber when the modified chemical timescale was used. This may be due to the higher reaction rates predicted when using the modified chemical timescale, which result in lower densities following combustion. Consequently, to conserve mass the resulting pressure is higher.

Figure 5.16 shows the ratio of the static wall pressure to the secondary flow total pressure (i.e., the engine pressure ratio) along the length of the engine ( $x/L$ ) when the jet stagnation pressure was 400 kPa. Additionally, the geometry of the engine expressed as the engine diameter ratio ( $D/D_{jet}$ ) is shown. As can be seen, both chemical timescales produced results that generally agree with the trends observed in experiment. One notable exception is the decrease in pressure observed experimentally near the exit of the mixing tube, which differs from the computational results. When the modified chemical timescale was used it resulted in higher pressures in the mixing tube and diffuser which more closely matched the mean experimental values than the default timescale. However, the results of both timescales agreed within experimental uncertainty. Near the exit of the diffuser, inside the combustion chamber, and the engine exit nozzle, both timescales resulted in similar pressure ratios which agree well with experiment.

Table 5.4 shows the predicted thrust and entrainment for the default and modified chemical timescales as well as from experiment. When the jet stagnation pressure was 200 kPa, a large variation in the thrust and entrainment was observed experimentally which is reflected in the large uncertainty value. At this pressure, both timescales were within experimental uncertainty but were lower than the average experimental values for thrust and entrainment. However, the modified timescale predicted a thrust closer to the average experimental value. In contrast, the default timescale provided a slightly better match to the average experimental entrainment. For the 400 kPa case, both timescales again predicted entrainment and thrust values that agreed within experimental uncertainty, however the modified timescale results were closer to the average experimental values. For the thrust, compared to the average experimental value, it was observed that the default timescale under-predicted it while the modified one over-predicted it. Lastly, for the 900 kPa case only the default chemical timescale was used since no combustion was observed so the choice of timescale is irrelevant. For this pressure entrainment was well-predicted, with only a 2.2% difference from the mean experimental value. However, thrust was found to differ significantly with an error of 34.9%. Note that for this case, the AIS did not produce net forward thrust which is reflected in the negative thrust value.

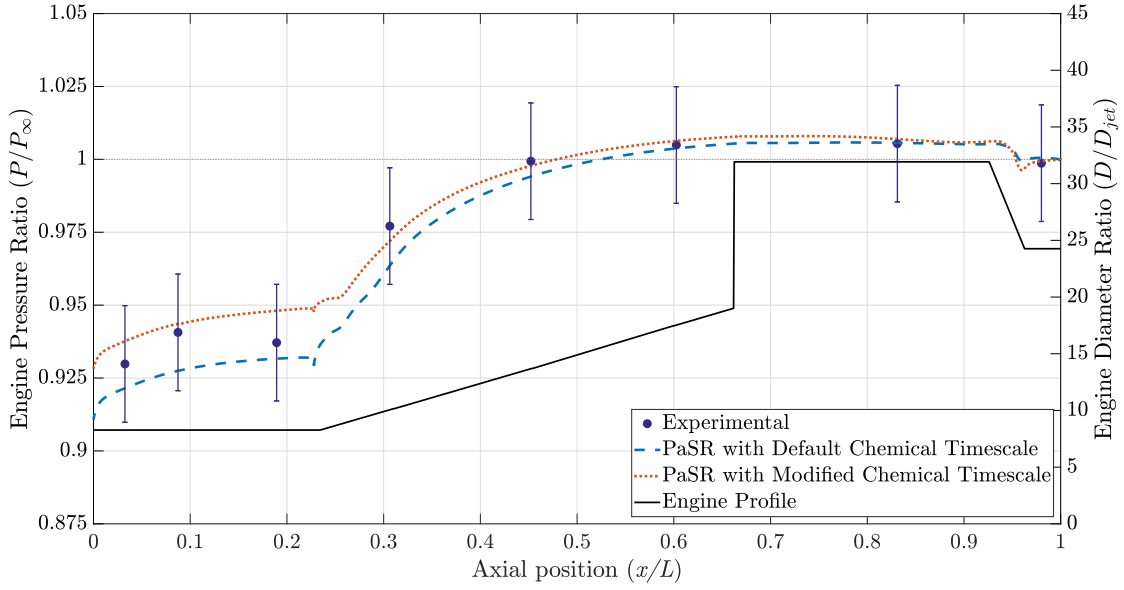


Figure 5.16: Engine pressure ratio along the length of the AIS ejector ramjet. Modified from Long et al. (2022).

Table 5.4: Comparison of reactingPimpleCentralFOAM results obtained with the default PaSR chemical timescale available in OpenFOAM and a modified chemical timescale from Akerblom (2022) to experiment (Long, 2024) for various jet stagnation pressures. Experimental results consist of a mean value with the corresponding 95% confidence interval. For the reactingPimpleCentralFOAM results, the percentages in parentheses show the absolute relative error in comparison to the mean experimental values.

$P_{o,jet}$	$\psi$	Experimental	Default Timescale	Modified Timescale
200 kPa	$\omega$	$25.9 \pm 21.7$	19.9 (23.2%)	19.5 (24.7%)
	$F_{AIS}$ (N)	$4.86 \pm 4.69$	3.4 (30.6%)	3.8 (22.4%)
400 kPa	$\omega$	$19.4 \pm 11.0$	20.8 (7.2%)	18.8 (3.1%)
	$F_{AIS}$ (N)	$13.90 \pm 5.46$	10.9 (21.6%)	15.8 (13.7%)
900 kPa	$\omega$	$13.40 \pm 6.55$	13.2 (2.2%)	-
	$F_{AIS}$ (N)	$-15.20 \pm 3.64$	-9.9 (34.9%)	-

A possible reason for the discrepancy in AIS thrust for the 900 kPa case is an over-prediction of the velocity in the recirculation zone in the combustion chamber. As seen in Fig. 5.17, the recirculation zone was much larger when the jet stagnation pressure was 900 kPa compared to when it was 400 kPa. This suggests recirculation is more significant for the 900 kPa case compared to the cases with combustion. Shahi

et al. (2015) found that the axial velocity profile in the recirculation zone following a backward facing step was overestimated when the  $k - \omega$  SST turbulence model was used. For the 900 kPa case, with its larger recirculation zone, this over-prediction of the axial velocity could lead to a larger exit velocity for the engine. With a larger exit velocity there would be a larger forward force on the engine, leading to a over-prediction (less negative value) of the thrust.

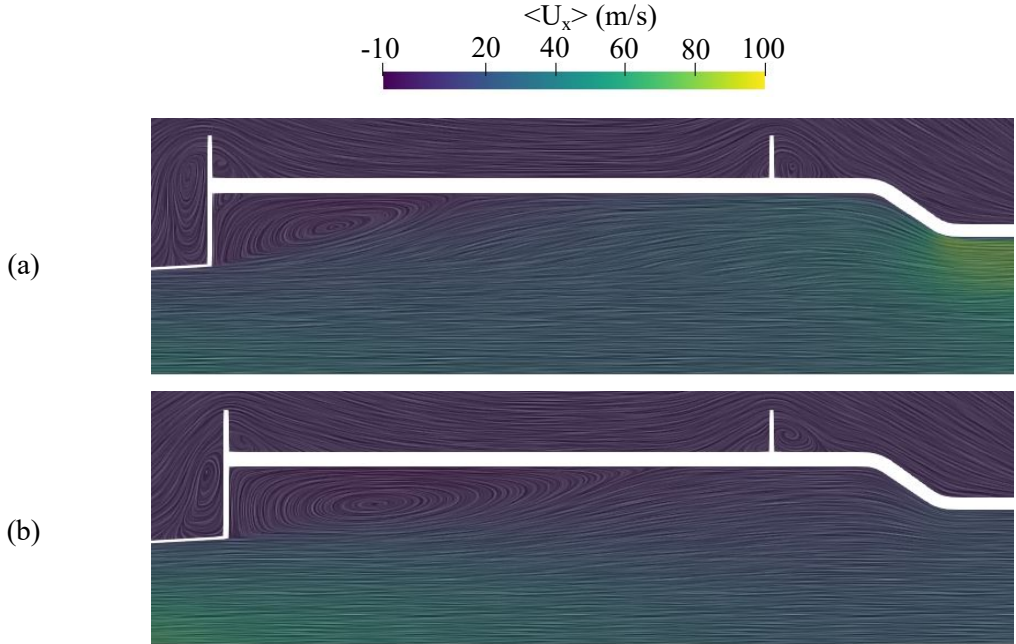


Figure 5.17: Recirculation zone in the combustion chamber for (a) 400 and (b) 900 kPa jet stagnation pressures. Both cases used the default chemical timescale with the PaSR combustion model, however combustion did not occur for the 900 kPa case.

## 5.4 Chapter Summary

A CFD validation study was done for the compressible reactive third-party OpenFOAM solver reactingPimpleCentralFOAM. The first case considered was a one-dimensional laminar flame for propane and methane reacting in air. It was found that the laminar flame speeds obtained with reactingPimpleCentralFOAM agreed reasonably well to the flame speeds obtained with Cantera for simple global reaction mechanisms, but the flame speeds were significantly under-predicted for more detailed mechanisms at higher equivalence ratios. This was observed in previous work by Cloney et al. (2018), indicating reactingPimpleCentralFOAM performs similarly to other available OpenFOAM models.

A second validation case compared results from reactingPimpleCentralFOAM with RANS turbulence

modelling, the PaSR combustion model, and a 2-step reaction mechanism to experimental data available for a bluff-body stabilized premixed propane–air flame. A reasonable match between experimental and CFD results was obtained for the axial velocity when a modified mixing timescale was used, however the transverse velocity profiles were found to differ and the velocity fluctuations were generally over-predicted. Results obtained with LES by Ghani et al. (2015) saw marginally better agreement. However, given the substantial increase in computational cost required for LES, RANS turbulence modelling was used for the remainder of this work. Additionally, the temperature profiles were over-predicted at later axial positions, which could be due to the simplified reaction mechanism not accounting for radical formation as the reaction progresses.

The final validation case considered in this work compared computational results obtained with reactingPimpleCentralFOAM to experimental data available for the AIS when operating under static conditions with fuel jet stagnation pressures of 200, 400, and 900 kPa. RANS turbulence modelling was used with the PaSR combustion model and a 42-step reaction mechanism for methane and air combustion. Two chemical timescales were used and compared: the default definition used in OpenFOAM and a modified timescale modified from Akerblom (2022). Both timescales provided entrainment and thrust values that agreed within experimental uncertainty, but the modified timescale was found to better match the average experimental thrust. However it generally did not improve the prediction of entrainment. When the fuel jet stagnation pressure was 900 kPa combustion was found to not occur which agrees with experimental observations, however the thrust was found to differ significantly from the experimental value. This may be caused by the over-prediction of axial velocity in the recirculation zone following the stepped flame-holder in the combustion chamber.

## Chapter 6

# Analysis of the Performance Impacts of Preheating the Fuel Jet of an Ejector Ramjet

### 6.1 Changes in Operating Conditions and Performance

In Section 2.1 the previous analysis of the AIS was discussed. This included the work of Wilson (2017) regarding the change in performance when some of the heat from combustion was used to preheat the fuel jet. In particular, it was found that increasing the fuel jet stagnation temperature increased entrainment, increased specific impulse, and decreased exergy destruction leading to improved engine performance. However, that analysis used a control-volume approach and was not verified with CFD or experimental results. Therefore, in this work CFD was used to study the changes in engine performance, namely thrust, entrainment, and specific impulse, when a fraction of the heat from combustion was used to increase the stagnation temperature of the fuel jet.

An additional 4 cases with increased fuel jet stagnation temperatures were simulated to compare to the previous results with an unheated jet. Given its reasonable match to experimental results for the validation cases discussed in Chapter 5, the same computational model was used. In particular, this includes the reactingPimpleCentralFoam solver with the  $k - \omega$  SST turbulence model and the PaSR combustion model. The same 42-step reaction mechanism from Zettervall et al. (2017) that was used for the AIS validation case was also used here. Due to its better match to experimental results, the modified mixing timescale

(defined in Eq. 3.80) was used for the PaSR combustion model. For the chemical timescale, while both the default and modified definitions provided results that agreed within experimental uncertainty, the modified definition (defined in Eq. 3.78) more closely matched the mean experimental values for thrust and was therefore used for the remainder of this work.

The boundary conditions used for these preheated cases is shown in Fig. 6.1. They are identical to the validation case discussed in Section 5.3, with the exception that a region near the wall of the combustion chamber now has a specified heat transfer rate ( $q_{HX}$ ), which is shown in red. In this region a volumetric heat sink was used to remove a fraction of the heat released during combustion. This heat sink models the heat exchanger that would be used in the actual engine. In the axial direction, this region began 4 cm after the start of the combustion chamber and ended at the start of the exit nozzle. In the radial direction it extended from the wall 1 cm towards the center of the engine. The 4 cm gap from the start of the combustion chamber and the volumetric heat sink is due to the low velocity near the vertical wall of the stepped flame holder. In this area, due to this low velocity, there would be limited convective heat transfer. Consequently, if a heat sink was used from the start of the combustion chamber it would lead to unrealistically low temperatures near the flame holder. By moving the start of the volumetric heat sink 4 cm downstream, it was instead in a region of higher velocity (although part of the volumetric heat sink was still in the flame holder's recirculation zone).

The same procedure that was used with the modified chemical timescale previously was also used here, namely the final reaction rates for each species were set equal to a fraction of the reaction rates predicted from the PaSR combustion model. Once stable combustion was observed this fraction was increased until it was equal to 1, indicating the reaction rate was equal to that predicted from the PaSR combustion model. Additionally,  $q_{HX}$  was set equal to 0 (indicating no heat transfer) until the flame filled the combustion chamber.

Two different fuel jet stagnation temperatures were used, 586 and 879 K, which correspond to two and three times the stagnation temperature for the non-preheated case. To allow for a direct comparison of engine performance, the fuel jet stagnation pressure was set to 400 and 900 kPa, which are two of the pressures that were used for the non-preheated case. To determine an appropriate  $q_{HX}$  value, the NASA JANAF polynomial for  $C_p/R$  (defined in Eq. 3.18) was integrated from its starting stagnation temperature ( $T_0$ , 293 K) to its final temperature ( $T_f$ ), and then multiplied by  $R$  and the mass flow rate of the fuel jet ( $\dot{m}_{jet}$ ) as shown in Eq. 6.1. This is equal to the heat required to take the fuel jet from its initial stagnation temperature to its final value. Note however that this assumes the heat exchanger operates with 100% efficiency.

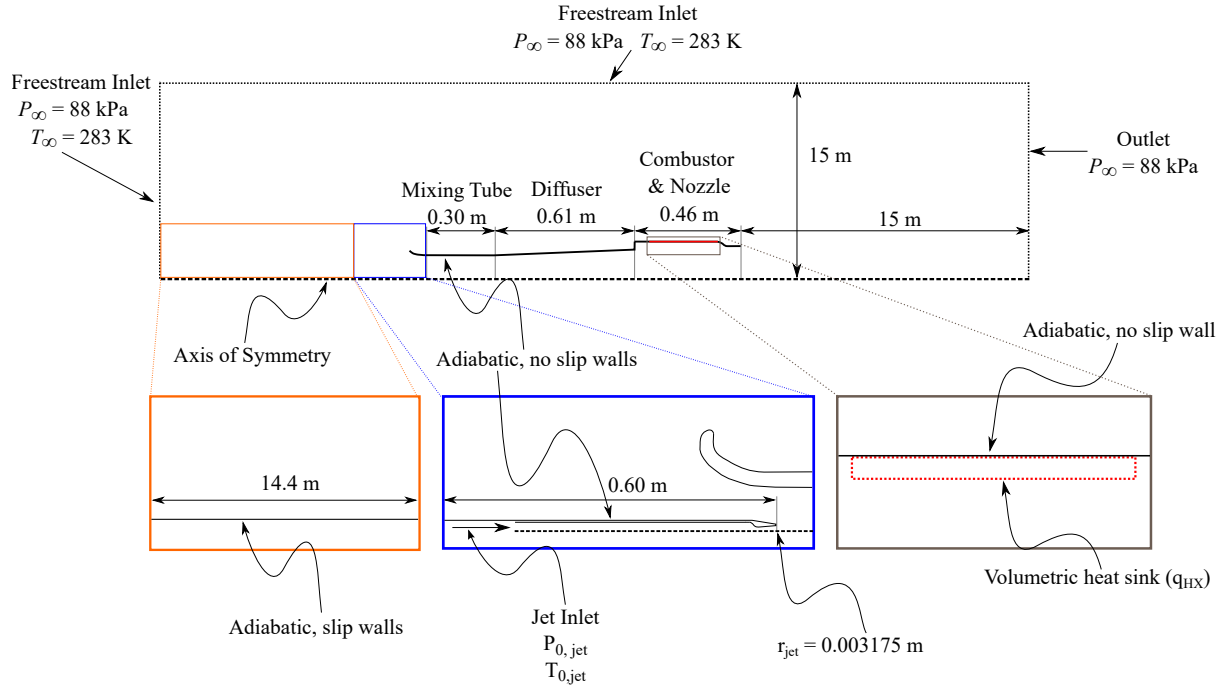


Figure 6.1: Domain and boundary conditions for the AIS when a fraction of the heat from combustion is used to preheat the fuel jet, not to scale.

$$q_{HX} = \int_{T_0}^{T_f} \dot{m}_{jet} C_p dT = \dot{m}_{jet} R \int_{T_0}^{T_f} \frac{C_p}{R} dT \quad (6.1)$$

It was observed that combustion was not sustained when the jet stagnation temperature and pressure were 879 K and 400 kPa, respectively. Here the entrainment ratio was approximately 34, which is slightly lower than the entrainment of 35.43 that results in a fuel-air ratio corresponding to the lower flammability limit for methane (Long et al., 2022). Therefore, this case was excluded from further analysis since it would not be a realistic operating condition for the AIS as you would not be able to extract heat from the combustion chamber to preheat the fuel jet if combustion did not occur.

Fig. 6.2 shows the averaged temperature, pressure, velocity magnitude, and progress variable in the combustion chamber for the preheated cases where combustion occurred. Furthermore, Figs. B.1 to B.4 show the same variables along the centerline of the ejector ramjet. Due to the heat sink being partially in the recirculation zone of the flame holder, a region of lower temperature fluid was observed near the front of the combustion chamber for all three cases. This is most clear when the jet stagnation temperature was 879 K, which required the largest value of  $q_{HX}$ . Additionally, the temperature following combustion was highest when the jet stagnation temperature and pressure were 586 K and 900 kPa, respectively. This is due

to this case being closest to stoichiometric conditions for combustion with an equivalence ratio of 0.97. In contrast, the other two cases had leaner combustion. When the jet stagnation temperature and pressure were 586 K and 400 kPa, respectively, the equivalence ratio was 0.65, while it was 0.76 when the jet stagnation temperature was 879 K. Furthermore, because of the higher temperature following combustion, the engine exit velocity was largest when the jet stagnation temperature was 586 K and the stagnation pressure was 900 kPa.

Table 6.1 shows the global equivalence ratio, entrainment ratio, AIS thrust, total thrust ( $F$ ), ISP, and combustion efficiency ( $\eta_c$ ) for both the preheated jet cases (excluding the case with no combustion) and the previous simulations where no preheating was used (see Section 5.3). The total thrust is the sum of the thrust from the AIS and the fuel jet; ISP was calculated from the total thrust. In this work the combustion efficiency was calculated as shown in Eq. 6.2. Here  $\dot{m}_0$  and  $\dot{m}_f$  is the mass flow rate of methane entering and exiting the combustion chamber, respectively.

$$\eta_c = 1 - \frac{\dot{m}_f}{\dot{m}_0} \quad (6.2)$$

Table 6.1: Comparison of global equivalence ratio ( $\phi$ ), entrainment ratio ( $\omega$ ), AIS thrust ( $F_{AIS}$ ), total thrust ( $F$ ), ISP, and combustion efficiency ( $\eta_c$ ) for an ejector ramjet when some of the heat from combustion is used to preheat the fuel jet. The non-preheated case used a fuel jet stagnation temperature of 293 K, while the preheated cases had stagnation temperatures of 586 and 879 K.

$T_{o,jet}$	$P_{o,jet}$	$\phi$	$\omega$	$F_{AIS}$ (N)	$F$ (N)	ISP (s)	$\eta_c$
293 K	400 kPa	0.88	18.8	15.8	23.6	199.2	100%
	900 kPa	1.23	13.2	-9.9	9.7	36.4	0%
586 K	400 kPa	0.65	25.6	9.5	19.9	243.6	100%
	900 kPa	0.97	17.3	26.8	45.8	250.5	92.5%
879 K	400 kPa	-	-	-	-	-	-
	900 kPa	0.76	21.8	23.2	42.0	284.9	94.5%

As seen in Table 6.1, increasing the stagnation temperature of the fuel jet led to an increased entrainment ratio for both the 400 and 900 kPa jet stagnation pressures. This is due to the higher velocity of the fuel as it exits the fuel nozzle when the stagnation temperature is higher which is shown in Fig B.3. This higher velocity leads to a lower pressure at the primary fuel nozzle outlet area, improving the suction of the secondary fluid consequently increasing the entrainment per unit mass of fuel used (Ping et al., 2023).

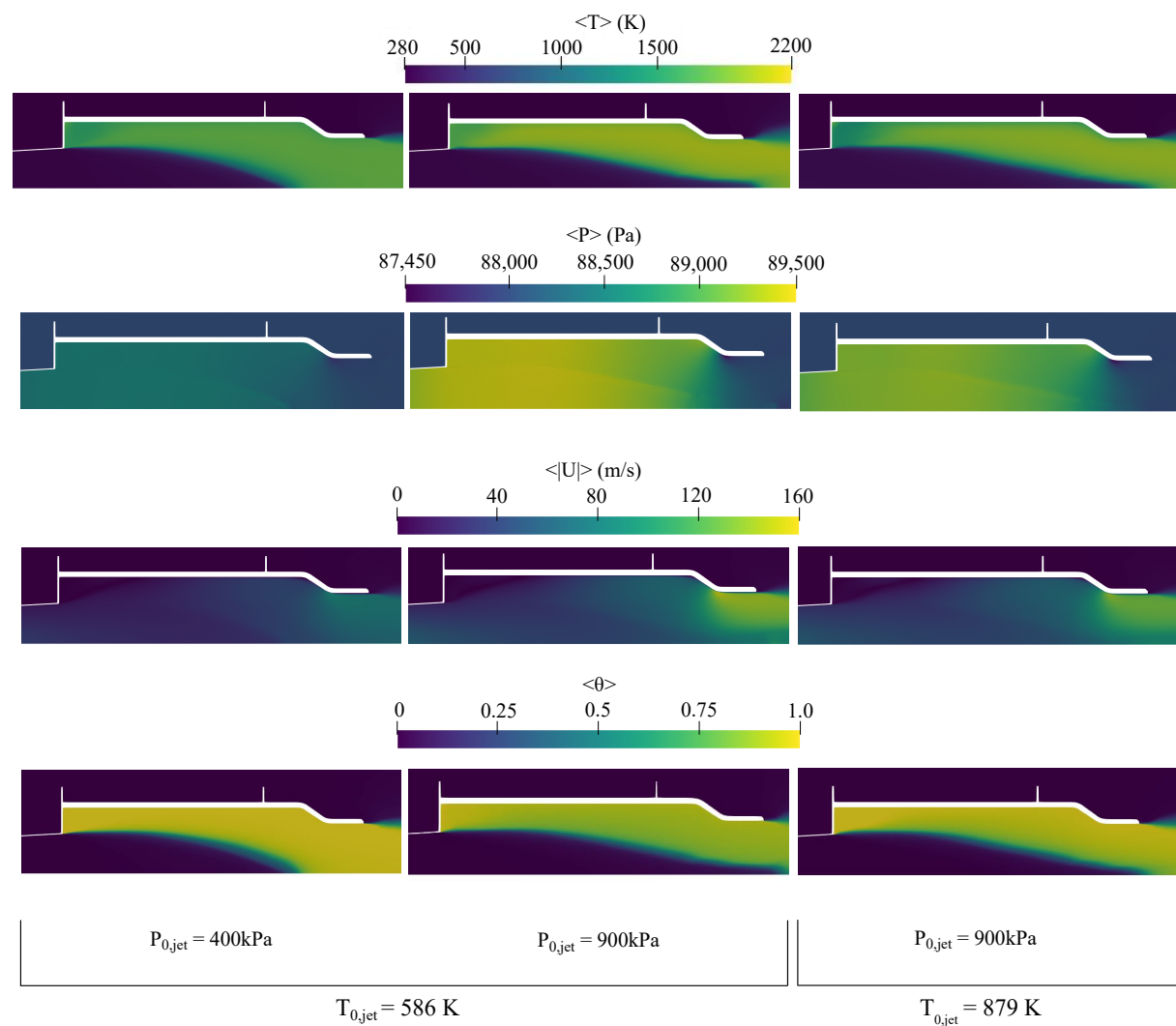


Figure 6.2: Averaged temperature, pressure, velocity magnitude, and progress variable in the combustion chamber when the fuel jet was heated with a fraction of the heat released during combustion.

Furthermore, as seen in Fig. B.1, increasing the jet stagnation temperature increased the temperature of the mixture before combustion. This higher temperature would lead to an increase in reaction rate. It is therefore expected that increasing the jet stagnation temperature would widen the flammability limits of the engine as well as improve the combustion efficiency. This may be the reason for the slight increase in combustion efficiency observed between the 586 and 879 K jet stagnation temperatures when the jet stagnation pressure was 900 kPa.

As discussed previously (see Section 2.1), using a control volume approach Wilson (2017) found that specific impulse increased with increasing fuel jet stagnation temperatures. While this is generally observed here as well, a notable exception is when the fuel jet stagnation temperature and pressure were 879 K and 400 kPa, respectively. For this case, combustion did not occur due to the fuel-air ratio being too low. This lower fuel-air ratio is due to two factors. The first is the increase in entrainment caused by increasing fuel jet stagnation temperatures leading to increased air flow (per unit mass of fuel used) into the engine. The second is a lower fuel mass flow rate through the primary fuel nozzle due to the increased stagnation temperature. When the jet stagnation pressure was 900 kPa, the fuel mass flow rate decreased from 27.2 g/s when the jet stagnation temperature was 293 K, to 18.7 and 15.0 g/s when it was 586 and 879 K, respectively. Furthermore, for cases with global equivalence ratios less than unity, when the jet stagnation pressure was held constant the AIS thrust was observed to decrease as the stagnation temperature was increased. For these cases, as the equivalence ratio decreases due to jet preheating, combustion becomes increasingly lean. Consequently, the temperature following combustion is lower leading to a lower flow velocity at the engine exit and lower resulting thrust. However, during engine operation this lower thrust could be overcome by increasing the mass flow rate through the engine, accomplished by increasing the stagnation pressure of the jet.

Increasing the jet stagnation temperature was observed to significantly improve engine performance when the jet stagnation pressure was 900 kPa. Here, as the stagnation temperature increased from 293 K to 586 K, the engine operating point went from non-combusting to combusting. Therefore, if the equivalence ratio is rich before preheating, then heating the jet brings the equivalence ratio closer to unity. This leads to increases in the thrust for the same jet stagnation pressure, in addition to a higher entrainment ratio and a higher specific impulse.

## 6.2 Chapter Summary

Using the computational model validated previously in this work, a CFD study was done to assess the performance impacts when a fraction of the heat from combustion was used to preheat the fuel jet for the

AIS when operating under static conditions. Two fuel jet stagnation pressures were considered, 400 and 900 kPa, along with stagnation temperatures of 586 and 879 K. However, when the stagnation pressure and temperature were 400 kPa and 879 K, respectively, combustion did not occur so this case was excluded from further analysis. Through comparison to non-preheated cases, when the fuel jet stagnation pressure was held constant increasing the stagnation temperature of the fuel jet for cases with lean combustion was found to increase entrainment and ISP but decrease AIS thrust. However, for cases where the equivalence ratio is higher than unity, preheating the fuel jet was found to increase AIS thrust, entrainment, and ISP. Furthermore, increasing the jet stagnation temperature is expected to widen the flammability limits of the engine as well as improve the combustion efficiency.

# Chapter 7

## Conclusion

Through a CFD validation and verification study of three different cases it was shown that a compressible reactive third-party OpenFOAM solver, reactingPimpleCentralFOAM, was capable of accurately modelling the physics relevant for combustion. The first case considered was a one-dimensional laminar flame for propane and methane reacting in air. It was found that the laminar flame speed obtained with reactingPimpleCentralFOAM agreed reasonably well to the flame speed obtained with Cantera for simple global reaction mechanisms, but the flame speed was significantly under-predicted for more detailed mechanisms at higher equivalence ratios. With more detailed chemical mechanisms, a more complete treatment of the transport properties may lead to a more accurate determination of the flame speed, but at substantially increased computational cost. This was observed in work by Cloney et al. (2018), indicating reactingPimpleCentralFOAM performs similar to other available OpenFOAM models.

The second validation and verification case compared results from reactingPimpleCentralFOAM with RANS turbulence modelling, the PaSR combustion model, and a 2-step reaction mechanism to experimental data available for a bluff-body stabilized premixed propane-air flame. A reasonable match between experimental axial velocities and those predicted from reactingPimpleCentralFOAM was obtained when a modified mixing timescale was used, however the transverse velocity profiles were found to differ and the velocity fluctuations were generally over-predicted. The results from reactingPimpleCentralFOAM were also compared to LES results from Ghani et al. (2015). The LES results saw better agreement, suggesting LES turbulence modelling could improve prediction of RMS and transverse velocities. Additionally, the temperature profiles were over-predicted at later axial positions, which could be due to the simplified reaction mechanism not accounting for radical formation as the reaction progresses.

The final validation case simulated an ejector ramjet operating at static conditions. Computational results

obtained with reactingPimpleCentralFOAM with RANS turbulence modelling, the PaSR combustion model with the modified mixing timescale, and a 42-step reaction mechanism for methane-air combustion were compared to experimental results. Additionally, the default chemical timescale for the PaSR combustion model in OpenFOAM was compared to a modified version to assess its accuracy. For both timescales it was found that the predicted thrust, entrainment ratio, and pressure profile along the engine agreed within experimental uncertainty. However, the modified timescale provided results that were closer to the mean experimental values for the thrust and the pressure profile along the walls of the mixing tube and the diffuser.

With the computational model assessed, the effects of regeneratively heating the fuel jet with an idealized heat exchanger in the combustor were studied. The same boundary conditions were used as the final validation case discussed previously, however a volumetric heat sink was used to model the heat exchanger between the combustion chamber and fuel jet. Furthermore, the same 42-step reaction mechanism was used, along with RANS turbulence modelling, and the PaSR combustion model with the modified chemical and mixing timescales. The results show that, while keeping the jet stagnation pressure constant, increasing the stagnation temperature of the fuel led to an increased entrainment ratio. For cases with rich global equivalence ratios, this increase in entrainment ratio was found to lead to increases in thrust, combustion efficiency, and specific impulse. In contrast, when the global equivalence ratio is less than unity, increasing the fuel's stagnation temperature while keeping its stagnation pressure constant was found to decrease the AIS thrust but still improve the engine's specific impulse. Furthermore, it may lead to combustion not occurring if the resulting equivalence ratio is below the flammability limit for the engine.

# References

- Akerblom, A. (2022), Turbulence-chemistry interaction in openfoam and how to implement a dynamic pasr model for les of turbulent combustion, *in* H. Nilsson, ed., ‘Proceedings of CFD with OpenSource Software’.
- APAN (2018), ‘Model validation for propulsion (mvp) workshop: Validation cases’.  
**URL:** <https://community.apan.org/wg/afrlcg/mvpws/p/cases>
- Baidya, R., Pesyridis, A. and Cooper, M. (2018), ‘Ramjet nozzle analysis for transport aircraft configuration for sustained hypersonic flight’, *Applied Sciences* **8**(4).
- Barrett, R. and Gluhareff, I. (2008), Gluhareff pressure jet engine: Past, present and future opportunities, *in* ‘46th AIAA Aerospace Sciences Meeting and Exhibit’.
- Bartosiewicz, Y., Aidoun, Z. and Mercadier, Y. (2006), ‘Numerical assessment of ejector operation for refrigeration applications based on cfd’, *Applied Thermal Engineering* **26**(5), 604–612.
- Berglund, M., Fedina, E., Fureby, C., Tegnér, J. and Sabel’nikov, V. (2010), ‘Finite rate chemistry large-eddy simulation of self-ignition in supersonic combustion ramjet’, *AIAA Journal* **48**(3), 540–550.
- Berglund, M. and Fureby, C. (2007), ‘Les of supersonic combustion in a scramjet engine model’, *Proceedings of the Combustion Institute* **31**(2), 2497–2504.
- Besagni, G. and Inzoli, F. (2017), ‘Computational fluid-dynamics modeling of supersonic ejectors: Screening of turbulence modeling approaches’, *Applied Thermal Engineering* **117**, 122–144.
- Biferi, G., Giacomelli, F., Mazzelli, F. and Milazzo, A. (2016), ‘Cfd modelling of the condensation inside a supersonic ejector working with r134a’, *Energy Procedia* **101**, 1232–1239. ATI 2016 - 71st Conference of the Italian Thermal Machines Engineering Association.
- Bilger, R. W. (1975), ‘A note on favre averaging in variable density flows’, *Combustion Science and Technology* **11**(5-6), 215–217.

- Bosschaart, K. and de Goey, L. (2004), ‘The laminar burning velocity of flames propagating in mixtures of hydrocarbons and air measured with the heat flux method’, *Combustion and Flame* **136**(3), 261–269.
- Bredberg, J. (2000), On the wall boundary condition for turbulence models, *in* ‘Internal Report 00 / 4’.
- Bösenhofer, M., Wartha, E., Jordan, C. and Harasek, M. (2018), ‘The eddy dissipation concept—analysis of different fine structure treatments for classical combustion’, *Energies* **11**(7).
- Candler, G., Peterson, D. D. and Drayna, T. (2012), Detached eddy simulation of a generic scramjet inlet and combustor, *in* ‘47th AIAA Aerospace Sciences Meeting including The New Horizons Forum and Aerospace Exposition’.
- CERFACS (2017), ‘Cantera users guide – methane/air combustion’.
- URL:** <https://www.cerfacs.fr/cantera/>
- Choi, J., Ma, F. and Yang, V. (2005), ‘Combustion oscillations in a scramjet engine combustor with transverse fuel injection’, *Proceedings of the Combustion Institute* **30**(2), 2851–2858.
- Chomiak, J. and Karlsson, A. (1996), ‘Flame liftoff in diesel sprays’, *Symposium (International) on Combustion* **26**(2), 2557–2564.
- Chunnanond, K. and Aphornratana, S. (2004a), ‘Ejectors: applications in refrigeration technology’, *Renewable and Sustainable Energy Reviews* **8**(2), 129–155.
- Chunnanond, K. and Aphornratana, S. (2004b), ‘An experimental investigation of a steam ejector refrigerator: the analysis of the pressure profile along the ejector’, *Applied Thermal Engineering* **24**, 311–322.
- Cloney, C. T. (2018), Burning Velocity and Lower Flammability Limits of Hybrid Mixtures Containing Combustible Dust and Flammable Gas, PhD thesis, Dalhousie University, Halifax, NS, Canada.
- Cloney, C. T., Ripley, R. C., Pegg, M. J. and Amyotte, P. R. (2018), ‘Laminar burning velocity and structure of coal dust flames using a unity lewis number cfd model’, *Combustion and Flame* **190**, 87–102.
- Daines, R. and Segal, C. (1998), ‘Combined rocket and airbreathing propulsion systems for space-launch applications’, *Journal of Propulsion and Power* **14**(5), 605–612.
- Dirrenberger, P., Le Gall, H., Bounaceur, R., Herbinet, O., Glaude, P.-A., Konnov, A. and Battin-Leclerc, F. (2011), ‘Measurements of laminar flame velocity for components of natural gas’, *Energy & Fuels* **25**(9), 3875–3884.

- Duwig, C., Nogenmyr, K., Chan, C. and Dunn, M. (2011), ‘Large eddy simulations of a piloted lean premix jet flame using finite-rate chemistry’, *Combustion Theory and Modelling* **15**(4), 537–568.
- Ebrahimi, H. (2006), ‘Overview of gas turbine augmentor design, operation, and combustion oscillation’, *42nd AIAA/ASME/SAE/ASEE Joint Propulsion Conference*.
- Ehn, A., Petersson, P., Zhu, J., Li, Z., Aldén, M., Nilsson, E., Larfeldt, J., Larsson, A., Hurtig, T., Zettervall, N. and Fureby, C. (2017), ‘Investigations of microwave stimulation of a turbulent low-swirl flame’, *Proceedings of the Combustion Institute* **36**(3), 4121–4128.
- Ecà, L. and Hoekstra, M. (2014), ‘A procedure for the estimation of the numerical uncertainty of cfd calculations based on grid refinement studies’, *Journal of Computational Physics* **262**, 104–130.
- Fedina, E. and Fureby, C. (2011), ‘A comparative study of flamelet and finite rate chemistry les for an axisymmetric dump combustor’, *Journal of Turbulence* **12**, N24.
- Fox, R. (2003), *Computational Models for Turbulent Reacting Flows*, Cambridge Series in Chemical Engineering, Cambridge University Press.
- Franzelli, B., Riber, E., Gicquel, L. Y. and Poinsot, T. (2012), ‘Large eddy simulation of combustion instabilities in a lean partially premixed swirled flame’, *Combustion and Flame* **159**(2), 621–637.
- Fry, R. S. (2004), ‘A century of ramjet propulsion technology evolution’, *Journal of Propulsion and Power* **20**(1), 27–58.
- Fureby, C. (2012), Les for supersonic combustion, in ‘18th AIAA/3AF International Space Planes and Hypersonic Systems and Technologies Conference’.
- Fureby, C., Nordin-Bates, K., Petterson, K., Bresson, A. and Sabelnikov, V. (2015), ‘A computational study of supersonic combustion in strut injector and hypermixer flow fields’, *Proceedings of the Combustion Institute* **35**(2), 2127–2135.
- Ghani, A., Poinsot, T., Gicquel, L. and Staffelbach, G. (2015), ‘Les of longitudinal and transverse self-excited combustion instabilities in a bluff-body stabilized turbulent premixed flame’, *Combustion and Flame* **162**(11), 4075–4083.
- Golovitchev, V., Nordin, N., Jarnicki, R. and Chomiak, J. (2000), ‘3-d diesel spray simulations using a new detailed chemistry turbulent combustion model’, *SAE transactions* **109**, 1391–1405.
- Gonzalez, M. and Borghi, R. (1991), ‘A lagrangian intermittent model for turbulent combustion; theoretical basis and comparisons with experiments’, *Turbulent Shear Flows* **7**, 293–311.

- Goodwin, D. G., Moffat, H. and Speth, R. L. (2021), Cantera: An object-oriented software toolkit for chemical kinetics, thermodynamics, and transport processes. version 2.5.1.
- Gran, I. and Magnussen, B. (1996), ‘A numerical study of a bluff-body stabilized diffusion flame. part 2. influence of combustion modeling and finite-rate chemistry’, *Combustion Science and Technology* **119**(1-6), 191–217.
- Greenshields, C. J., Weller, H. G., Gasparini, L. and Reese, J. M. (2009), ‘Implementation of semi-discrete, non-staggered central schemes in a colocated, polyhedral, finite volume framework, for high-speed viscous flows’, *International Journal for Numerical Methods in Fluids* **63**(1), 1–21.
- Gu, X., Haq, M., Lawes, M. and Woolley, R. (2000), ‘Laminar burning velocity and markstein lengths of methane-air mixtures’, *Combustion and Flame* **121**(1), 41–58.
- Hannemann, K., Karl, S., Schramm, J. M. and Steelant, J. (2010), ‘Methodology of a combined ground based testing and numerical modelling analysis of supersonic combustion flow paths’, *Shock Waves* **20**, 353–366.
- Hirschfelder, J. O., Curtiss, C. F. and Bird, R. B. (1954), *Molecular Theory Of Gases And Liquids*, John Wiley & Sons.
- Hirsh, C. (2007), *Numerical Computation of Internal & External Flows*, 2nd edn, John Wiley & Sons.
- Huang, B., Chang, J., Wang, C. and Petrenko, V. (1999), ‘A 1-d analysis of ejector performance’, *International Journal of Refrigeration* **22**(5), 354–364.
- Huang, B. J., Jiang, C. B. and Hu, F. L. (1985), ‘Ejector Performance Characteristics and Design Analysis of Jet Refrigeration System’, *Journal of Engineering for Gas Turbines and Power* **107**(3), 792–802.
- Jasak, H. (1996), Error Analysis and Estimation for the Finite Volume Method With Applications to Fluid Flows, PhD thesis, Imperial College London.
- Kee, R., Coltrin, M. E., Glarborg, P. and Zhu, H. (2017), *Molecular Transport*, John Wiley & Sons, Ltd, chapter 11, pp. 371–416.
- Kors, D. (1991), ‘Design considerations for combined air breathing-rocket propulsion systems’, *2nd International Aerospace Planes Conference*.
- Kramer, J. M. and Morton, C. J. C. (2022), Interaction of confined jet recirculation with flow entrainment and compression, in ‘AIAA Aviation 2022 Forum’, Chicago, Illinois.

- Kraposhin, M., Bovtikova, A. and Strijhak, S. (2015), ‘Adaptation of kurganov-tadmor numerical scheme for applying in combination with the piso method in numerical simulation of flows in a wide range of mach numbers’, *Procedia Computer Science* **66**, 43–52.
- Kraposhin, M. V., Banholzer, M., Pfitzner, M. and Marchevsky, I. K. (2018), ‘A hybrid pressure-based solver for nonideal single-phase fluid flows at all speeds’, *International Journal for Numerical Methods in Fluids* **88**(2), 79–99.
- Kuo, K. K. and Acharya, R. (2012), *Fundamentals of Turbulent and Multiphase Combustion*, John Wiley & Sons, Ltd, chapter 1, pp. 1–42.
- Kurganov, A., Noelle, S. and Petrova, G. (2001), ‘Semidiscrete central-upwind schemes for hyperbolic conservation laws and hamilton–jacobi equations’, *SIAM Journal on Scientific Computing* **23**(3), 707–740.
- Kurganov, A. and Tadmor, E. (2000), ‘New high-resolution central schemes for nonlinear conservation laws and convection–diffusion equations’, *Journal of Computational Physics* **160**(1), 241–282.
- Labahn, J., Dovizio, D. and Devaud, C. (2015), ‘Numerical simulation of the delft-jet-in-hot-coflow (djh) flame using conditional source-term estimation’, *Proceedings of the Combustion Institute* **35**(3), 3547–3555.
- Lastiwka, D. K., Korobenko, A. and Johansen, C. T. (2022), Validation and verification of pimplecentralfoam and a 1d-eram solver for analysis of an ejector-ramjet, *in* ‘AIAA Aviation 2022 Forum’, Chicago, Illinois.
- Lastiwka, D., Korobenko, A., Hinman, W. S. and Johansen, C. T. (2023), Thermodynamic cycle analysis of an ejector-ramjet propulsion system - part 1, *in* ‘AIAA SCITECH 2023 Forum’, National Harbor, Maryland.
- Launder, B. and Spalding, D. (1974), ‘The numerical computation of turbulent flows’, *Computer methods in applied mechanics and engineering* **3**(2), 269–289.
- Li, Z. (2019), Sub-grid models for Large Eddy Simulation of non-conventional combustion regimes, PhD thesis, Technische Universität, Darmstadt.
- Li, Z., Ferrarotti, M., Cuoci, A. and Parente, A. (2018), ‘Finite-rate chemistry modelling of non-conventional combustion regimes using a partially-stirred reactor closure: Combustion model formulation and implementation details’, *Applied Energy* **225**, 637–655.
- Li, Z., Tomasch, S., Chen, Z. X., Parente, A., Ertesvåg, I. S. and Swaminathan, N. (2021), ‘Study of mild combustion using les and advanced analysis tools’, *Proceedings of the Combustion Institute* **38**(4), 5423–5432.

- Long, L. (2024), An experimental investigation of ejector ramjet performance at static conditions, Master's thesis, University of Calgary, Calgary, AB, Canada. Thesis in progress.
- Long, L., Javaji, R., Nelson, W., Edwards, J., Ziadé, P., Morton, C. and Johansen, C. (2022), Development of a facility to test an ejector ramjet at static conditions, *in 'AIAA Aviation 2022 Forum'*, Chicago, Illinois.
- Lovett, J., Brogan, T., Philippina, D., Kiel, B. and Thompson, T. (2004), 'Development needs for advanced afterburner designs', *40th AIAA/ASME/SAE/ASEE Joint Propulsion Conference and Exhibit*.
- Ma, K., Zhang, Z., Liu, Y. and Jiang, Z. (2020), 'Aerodynamic principles of shock-induced combustion ramjet engines', *Aerospace Science and Technology* **103**.
- Magnussen, B. (1981), 'On the structure of turbulence and a generalized eddy dissipation concept for chemical reaction in turbulent flow', *19th Aerospace Sciences Meeting*.
- Magnussen, B. and Hjertager, B. (1977), 'On mathematical modeling of turbulent combustion with special emphasis on soot formation and combustion', *Symposium (International) on Combustion* **16**(1), 719–729.
- Magnussen, B. and Hjertager, B. (2005), 'The eddy dissipation concept -a bridge between science and technology', *ECCOMAS thematic conference on computational combustion*.
- Marshall, A., Gupta, A., Lavelle, T. and Lewis, M. (2004), 'Critical issues in tbcc modeling', *40th AIAA/ASME/SAE/ASEE Joint Propulsion Conference and Exhibit*.
- Mathur, S., Tondon, P. and Saxena, S. (1967), 'Thermal conductivity of binary, ternary and quaternary mixtures of rare gases', *Molecular Physics* **12**(6), 569–579.
- Mazzelli, F., Little, A. B., Garimella, S. and Bartosiewicz, Y. (2015), 'Computational and experimental analysis of supersonic air ejector: Turbulence modeling and assessment of 3d effects', *International Journal of Heat and Fluid Flow* **56**, 305–316.
- Menon, S. (1992), 'Active combustion control in a ramjet using large-eddy simulations', *Combustion Science and Technology* **84**(1-6), 51–79.
- Menter, F. (1992), 'Influence of freestream values on k-omega turbulence model predictions', *AIAA Journal* **30**(6), 1657–1659.
- Menter, F. (1993), 'Zonal two equation k-w turbulence models for aerodynamic flows', *23rd Fluid Dynamics, Plasmadynamics, and Lasers Conference*.

- Menter, F. R. (1994), ‘Two-equation eddy-viscosity turbulence models for engineering applications’, *AIAA Journal* **32**(8), 1598–1605.
- Micka, D. and Driscoll, J. (2008), ‘Reaction zone imaging in a dual-mode scramjet combustor using ch-plif’, *44th AIAA/ASME/SAE/ASEE Joint Propulsion Conference*.
- Micka, D. J. and Driscoll, J. F. (2009), ‘Combustion characteristics of a dual-mode scramjet combustor with cavity flameholder’, *Proceedings of the Combustion Institute* **32**(2), 2397–2404.
- Migadel, T. E., Lastiwka, D., Korobenko, A. and Johansen, C. T. (2023), Validation and verification of reactingpimplecentralfoam for ejector ramjet applications, in ‘AIAA SCITECH 2023 Forum’, National Harbor, Maryland.
- Moukalled, F., Mangani, L. and Darwish, M. (2016), *The Finite Volume Method in Computational Fluid Dynamics : An Advanced Introduction with OpenFOAM® and Matlab*, Vol. 113 of *Fluid Mechanics and its Applications*, Springer.
- Munday, J. T. and Bagster, D. F. (1977), ‘A new ejector theory applied to steam jet refrigeration’, *Industrial & Engineering Chemistry Process Design and Development* **16**(4), 442–449.
- Neill, S. M. and Pesyridis, A. (2017), ‘Modeling of supersonic combustion systems for sustained hypersonic flight’, *Energies* **10**(11).
- Nogenmyr, K., Fureby, C., Bai, X., Petersson, P., Collin, R. and Linne, M. (2009), ‘Large eddy simulation and laser diagnostic studies on a low swirl stratified premixed flame’, *Combustion and Flame* **156**(1), 25–36.
- Nordin-Bates, K., Fureby, C., Karl, S. and Hannemann, K. (2017), ‘Understanding scramjet combustion using les of the hyshot ii combustor’, *Proceedings of the Combustion Institute* **36**(2), 2893–2900.
- Nordin, P. (2001), Complex chemistry modeling of diesel spray combustion, PhD thesis.
- Olovsson, S. (1992), ‘Combustion calculations on a premixed system with a bluff body flameholder’, *28th Joint Propulsion Conference and Exhibit*.
- Parente, A., Malik, M., Contino, F., Cuoci, A. and Dally, B. (2016), ‘Extension of the eddy dissipation concept for turbulence/chemistry interactions to mild combustion’, *Fuel* **163**, 98–111.
- Park, O., Veloo, P. S., Liu, N. and Egolfopoulos, F. N. (2011), ‘Combustion characteristics of alternative gaseous fuels’, *Proceedings of the Combustion Institute* **33**(1), 887–894.

- Pichon, T. and Laverdant, A. (2016), ‘Numerical simulation of reactive flows in ramjet type combustors and associated validation experiments’, *Aerospace Lab* .
- Pichon, T., Sabel’nikov, V., Moule, Y. and Cochet, A. (2012), Assessment of a partially stirred reactor combustion model to predict the lean blow-out limit of a ramjet combustor, in ‘18th AIAA/3AF International Space Planes and Hypersonic Systems and Technologies Conference’.
- Ping, Z., Chen, B., Wang, C., Xu, Z. and Wang, L. (2023), ‘High performance ejector enhanced by heat exchanger in solid oxide fuel cell anode recirculation system’, *Applied Thermal Engineering* **221**, 119856.
- Poinsot, T., Candel, S. and Trouv , A. (1995), ‘Applications of direct numerical simulation to premixed turbulent combustion’, *Progress in Energy and Combustion Science* **21**(6), 531–576.
- Poinsot, T. and Lelef, S. (1992), ‘Boundary conditions for direct simulations of compressible viscous flows’, *Journal of Computational Physics* **101**(1), 104–129.
- Poinsot, T. and Veynante, D. (2011), *Theoretical and Numerical Combustion*, 2nd edn, Edwards.
- Pope, S. (2000), *Turbulent Flows*, Cambridge University Press.
- Reichstadt, S., Bertier, N., Ristori, A. and Bruel, P. (2007), ‘Towards les of mixing processes inside a research ramjet combustor’, *18 ISABE Conference* .
- Ristori, A., Heid, G., Cochet, A. and Lavergne, G. (2012), ‘Experimental and numerical study of turbulent flow inside a research sdr combustor’, *35th Joint Propulsion Conference and Exhibit* .
- Roux, A., Gicquel, L. Y. M., Reichstadt, S., Bertier, N., Staffelbach, G., Vuillot, F. and Poinsot, T. (2010), ‘Analysis of unsteady reacting flows and impact of chemistry description in large eddy simulations of side-dump ramjet combustors’, *Combustion and Flame* **157**, 176–191.
- Roux, A., Reichstadt, S., Bertier, N., Vuillot, F. and Poinsot, T. (2008), ‘Comparison of numerical methods and combustion models for les of a ramjet configuration’.
- Rusly, E., Aye, L., Charters, W. and Ooi, A. (2005), ‘Cfd analysis of ejector in a combined ejector cooling system’, *International Journal of Refrigeration* **28**(7), 1092–1101.
- San Diego Mechanism web page, Mechanical and Aerospace Engineering (Combustion Research), University of California at San Diego (2012), ‘Chemical-kinetic mechanisms for combustion applications’.
- URL:** <http://combustion.ucsd.edu>

- Schonfeld, T. and Rudgyard, M. (1999), ‘Steady and unsteady flow simulations using the hybrid flow solver avbp’, *AIAA Journal* **37**(11), 1378–1385.
- Shabanian, S. R., Medwell, P. R., Rahimi, M., Frassoldati, A. and Cuoci, A. (2013), ‘Kinetic and fluid dynamic modeling of ethylene jet flames in diluted and heated oxidant stream combustion conditions’, *Applied Thermal Engineering* **52**(2), 538–554.
- Shahi, M., Kok, J. and Pozarlik, A. (2015), ‘On characteristics of a non-reacting and a reacting turbulent flow over a backward facing step ( bfs)’, *International Communications in Heat and Mass Transfer* **61**, 16–25.
- Sjunnesson, A., Henrickson, P. and Lofstrom, C. (1992), ‘Cars measurements and visualization of reacting flows in a bluff body stabilized flame’, *28th Joint Propulsion Conference and Exhibit*.
- Sjunnesson, A., Nelsson, C. and Max, E. (1991), ‘Lda measurements of velocities and turbulence in a bluff body stabilized flame’.
- Slotnick, J., Khodadoust., A., Alonso, J., Darmofal, D., Gropp, W., Lurie, E. and Mavriplis, D. (2014), Cfd vision 2030 study: A path to revolutionary computational aerosciences.
- Smith, G. P., Golden, D. M., Frenklach, M., Moriarty, N. W., Eiteneer, B., Goldenberg, M., Bowman, C. T., Hanson, R. K., Song, S., Jr., W. C. G., Lissianski, V. V. and Qin, Z. (1999), ‘Gri-mech 3.0’.
- Spalart, P. R. and Rumsey, C. L. (2007), ‘Effective inflow conditions for turbulence models in aerodynamic calculations’, *AIAA Journal* **45**(10), 2544–2553.
- Spalding, D. (1971), ‘Mixing and chemical reaction in steady confined turbulent flames’, *Symposium (International) on Combustion* **13**(1), 649–657. Thirteenth symposium (International) on Combustion.
- Sriveerakul, T., Aphornratana, S. and Chunnanond, K. (2007), ‘Performance prediction of steam ejector using computational fluid dynamics: Part 1. validation of the cfd results’, *International Journal of Thermal Sciences* **46**(8), 812–822.
- Stoldt, H. H., Korobenko, A., Ziade, P. and Johansen, C. T. (2021), ‘Verification and Validation of High-Fidelity Open-Source Simulation Tools for Supersonic Aircraft Aerodynamic Analysis’, *Journal of Verification, Validation and Uncertainty Quantification* **6**(4).
- Stoldt, H. H. R. (2021), Verification and validation of open-source simulation tools for supersonic aircraft aerodynamic analysis, Master’s thesis, University of Calgary, Calgary, AB, Canada.
- Sutherland, W. (1893), ‘Lii. the viscosity of gases and molecular force’, *The London, Edinburgh, and Dublin Philosophical Magazine and Journal of Science* **36**(223), 507–531.

- Syrakos, A., Varchanis, S., Dimakopoulos, Y., Goulas, A. and Tsamopoulos, J. (2017), ‘A critical analysis of some popular methods for the discretisation of the gradient operator in finite volume methods’, *Physics of Fluids* **29**(12), 127103.
- Sziroczak, D. and Smith, H. (2016), ‘A review of design issues specific to hypersonic flight vehicles’, *Progress in Aerospace Sciences* **84**, 1–28.
- Tashtoush, B. M., Al-Nimr, M. A. and Khasawneh, M. A. (2019), ‘A comprehensive review of ejector design, performance, and applications’, *Applied Energy* **240**, 138–172.
- Tuncer, O. (2012), ‘Combustion in a ramjet combustor with cavity flame holder’, *48th AIAA Aerospace Sciences Meeting Including the New Horizons Forum and Aerospace Exposition*.
- Turns, S. (2000), *An Introduction to Combustion: Concepts and Applications*, 2nd edn, McGraw-Hill.
- Vagelopoulos, C., Egolfopoulos, F. and Law, C. (1994), ‘Further considerations on the determination of laminar flame speeds with the counterflow twin-flame technique’, *Symposium (International) on Combustion* **25**(1), 1341–1347.
- van Leer, B. (1979), ‘Towards the ultimate conservative difference scheme. v. a second-order sequel to godunov’s method’, *Journal of Computational Physics* **32**(1), 101–136.
- Varga, S., Oliveira, A. C. and Diaconu, B. (2009), ‘Numerical assessment of steam ejector efficiencies using cfd’, *International Journal of Refrigeration* **32**(6), 1203–1211.
- Versteeg, H. and Malaasekera, W. (2007), *An Introduction to Computational Fluid Dynamics - The Finite Volume Method*, 2nd edn, Pearson.
- Veynante, D. and Vervisch, L. (2002), ‘Turbulent combustion modelling’, *Progress in Energy and Combustion Science* **28**, 193–266.
- Vincent-Randonnier, A., Sabelnikov, V., Ristori, A., Zettervall, N. and Fureby, C. (2018), ‘An experimental and computational study of hydrogen-air combustion in the lapcat ii supersonic combustor’, *Proceedings of the Combustion Institute* **37**.
- Wartha, E., Bösenhofer, M. and Harasek, M. (2021), ‘Characteristic chemical time scales for reactive flow modeling’, *Combustion Science and Technology* **193**(16), 2807–2832.
- Weller, H. G., Tabor, G., Jasak, H. and Fureby, C. (1998), ‘A tensorial approach to computational continuum mechanics using object-oriented techniques’, *Computers in Physics* **12**(6), 620–631.

- Westbrook, C. K. and Dryer, F. L. (1981), ‘Simplified reaction mechanisms for the oxidation of hydrocarbon fuels in flames’, *Combustion Science and Technology* **27**(1-2), 31–43.
- Whitley, N., Krothapalli, A. and Van Dommelen, L. (1996), ‘A determinate model of thrust-augmenting ejectors’, *Theoretical and computational fluid dynamics* **8**, 37–55.
- Wilcox, D. (2006), *Turbulence Modeling for CFD*, 3rd edn, DCW Industries.
- Wilke, C. R. (1950), ‘A viscosity equation for gas mixtures’, *The Journal of Chemical Physics* **18**(4), 517–519.
- Wilson, S. J. (2017), Assessment and analysis of a novel intake for a ramjet engine, Master’s thesis, University of Calgary, Calgary, AB, Canada.
- Wilson, S. J., Johansen, C. T. and Mravcak, V. (2015), ‘Performance analysis of the atlantis intake system’, *53rd AIAA Aerospace Sciences Meeting*.
- Zettervall, N. and Fureby, C. (2018), ‘A computational study of ramjet, scramjet and dual-mode ramjet combustion in combustor with a cavity flameholder’, *2018 AIAA Aerospace Sciences Meeting*.
- Zettervall, N., Fureby, C. and Nilsson, E. J. K. (2021), ‘Evaluation of chemical kinetic mechanisms for methane combustion: A review from a cfd perspective’, *Fuels* **2**(2), 210–240.
- Zettervall, N., Nordin-Bates, K., Nilsson, E. and Fureby, C. (2017), ‘Large eddy simulation of a premixed bluff body stabilized flame using global and skeletal reaction mechanisms’, *Combustion and Flame* **179**, 1–22.

## Appendix A

# Mesh Sensitivity Study Uncertainty Plots for the Bluff-body Stabilized Flame Validation Case

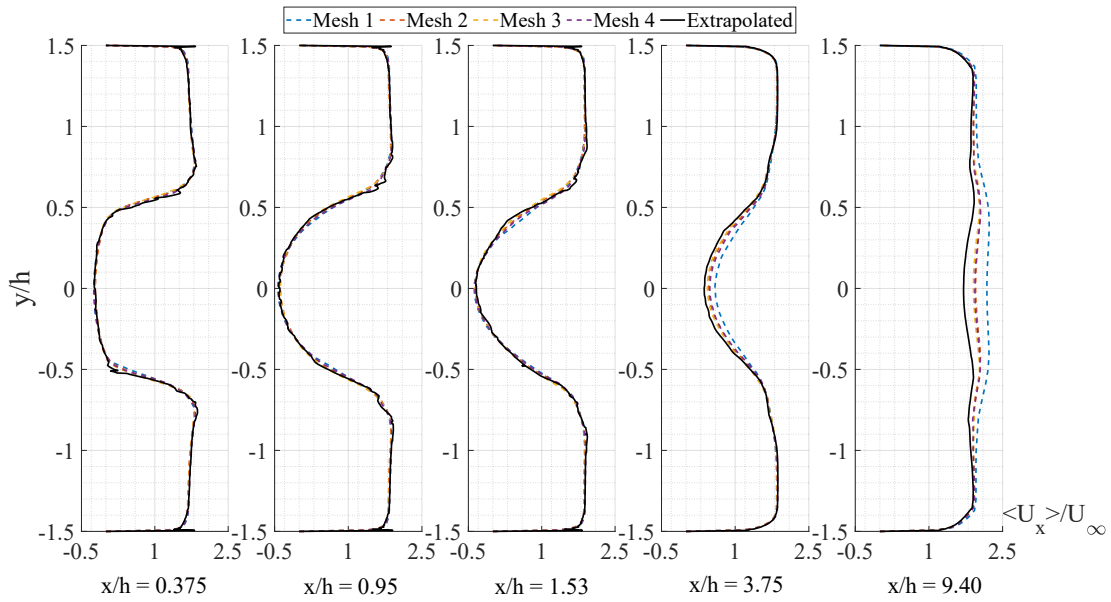


Figure A.1: Time-averaged axial-velocity profiles for various meshes and the resulting extrapolated profile. The velocities have been normalized by the free-stream velocity of 17.3 m/s.

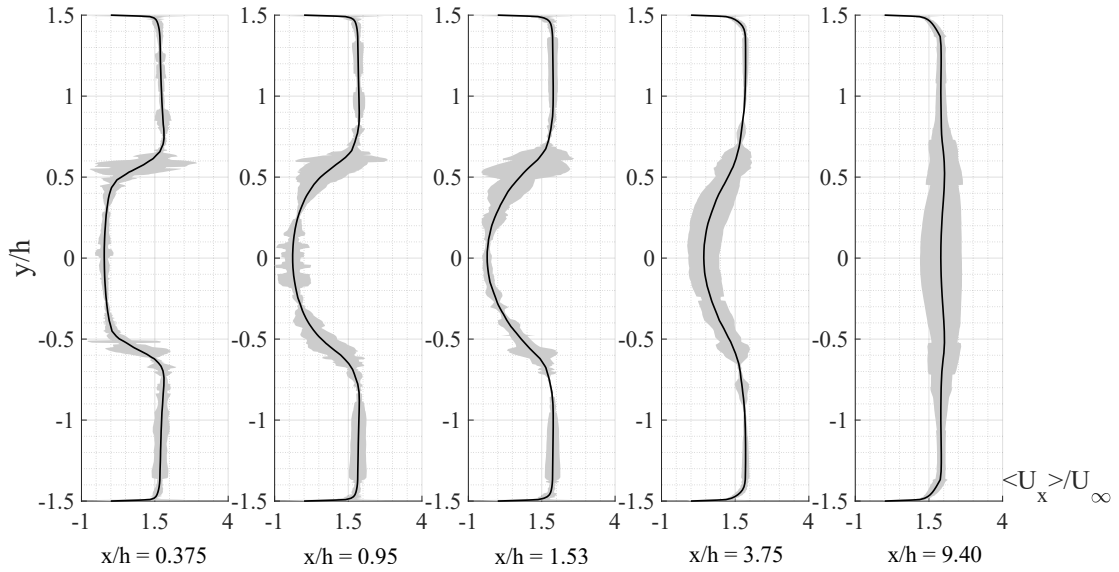


Figure A.2: Time-averaged axial-velocity profiles for Mesh 3 with corresponding uncertainty. The velocities have been normalized by the free-stream velocity of 17.3 m/s.

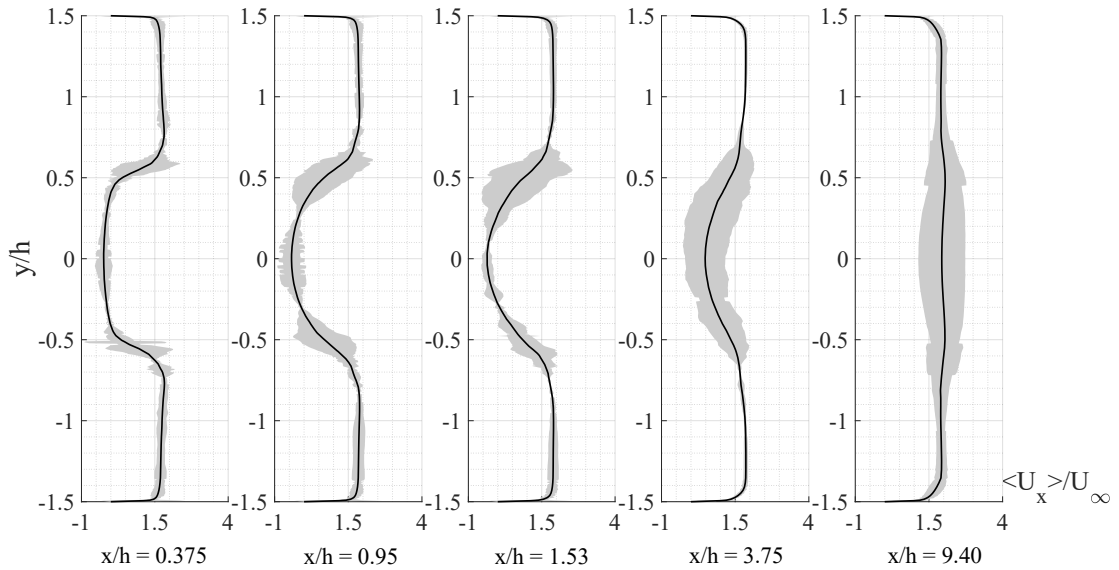


Figure A.3: Time-averaged axial-velocity profiles for Mesh 4 with corresponding uncertainty. The velocities have been normalized by the free-stream velocity of 17.3 m/s.

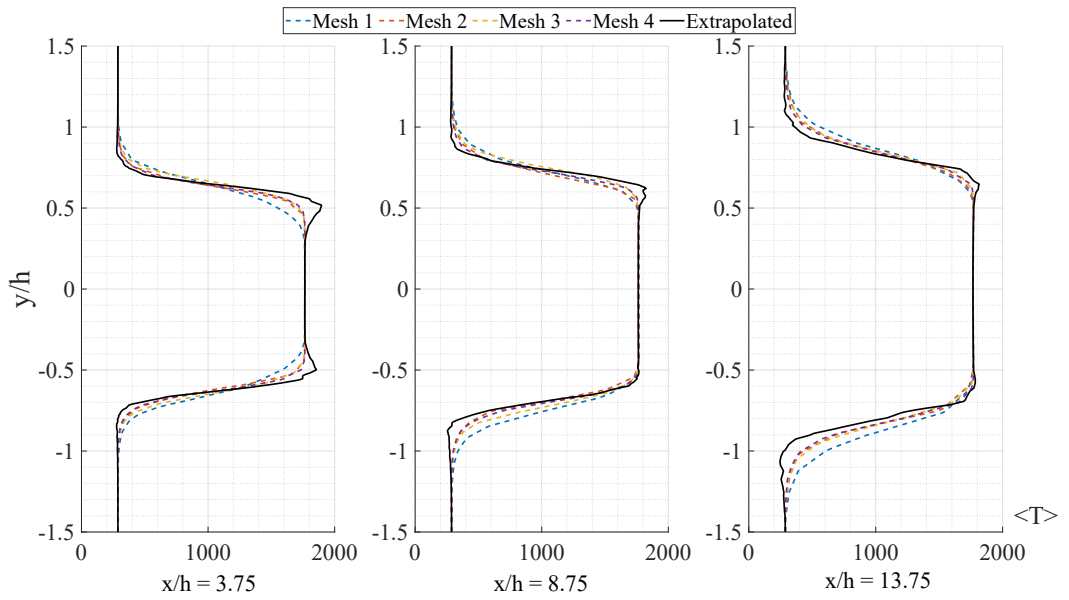


Figure A.4: Time-averaged temperature profiles for various meshes and the resulting extrapolated profile.

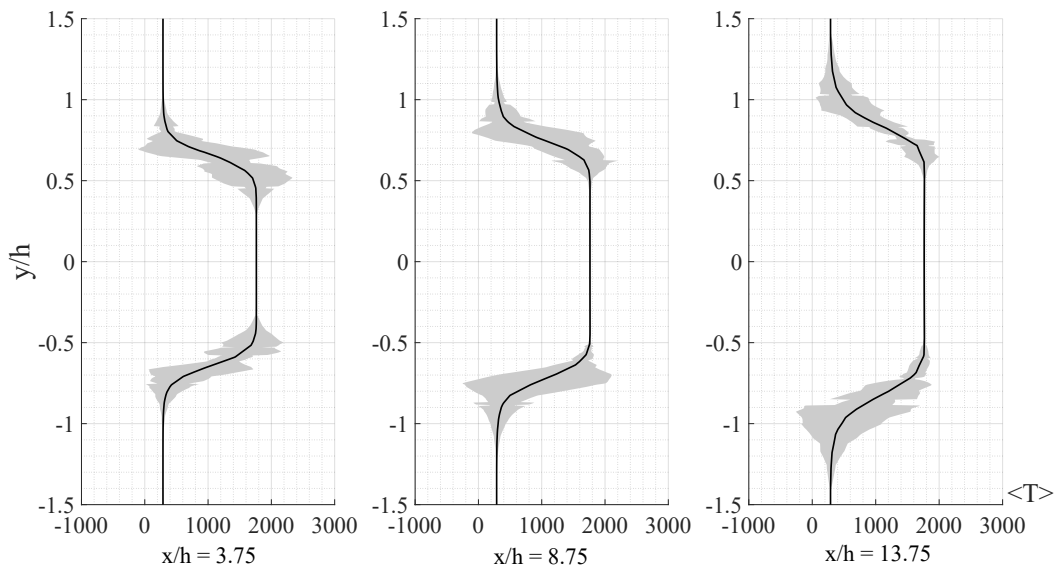


Figure A.5: Time-averaged temperature profiles for Mesh 3 with corresponding uncertainty.

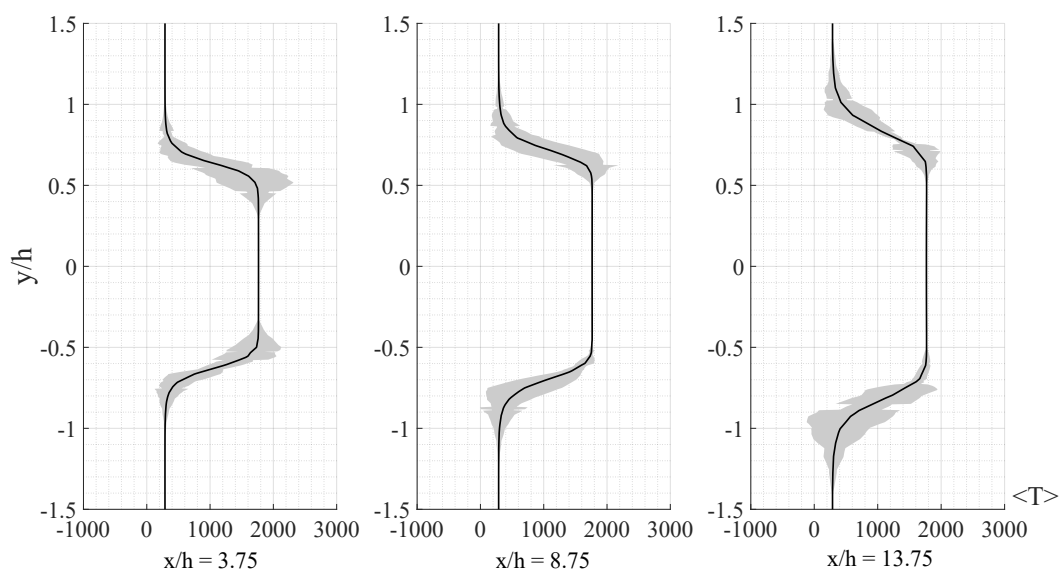


Figure A.6: Time-averaged temperature profiles for Mesh 4 with corresponding uncertainty.

## Appendix B

# Plots Along Centerline of the Ejector Ramjet

Figs. B.1 to B.4 show the averaged temperature, pressure, axial velocity, and progress variable along the centerline of the ejector ramjet. For the 400 kPa stagnation pressure case with no fuel preheating (i.e. stagnation temperature of 293 K), only the results using the modified chemical timescale (defined in Eq. 3.78) are shown.

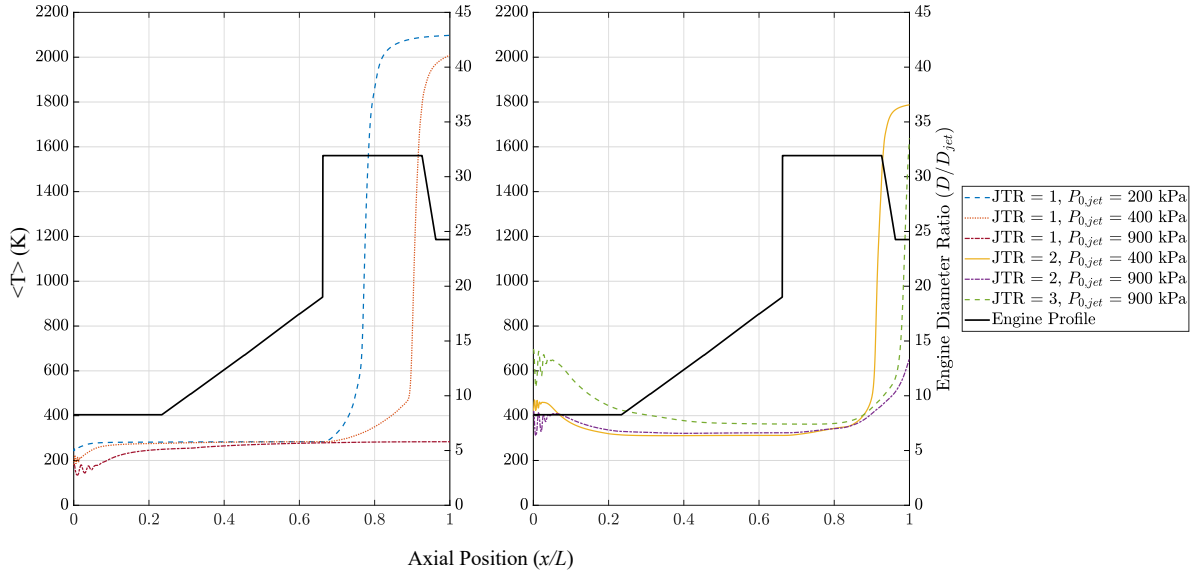


Figure B.1: Average temperature along centerline of the ejector ramjet for various jet stagnation temperatures and pressures.

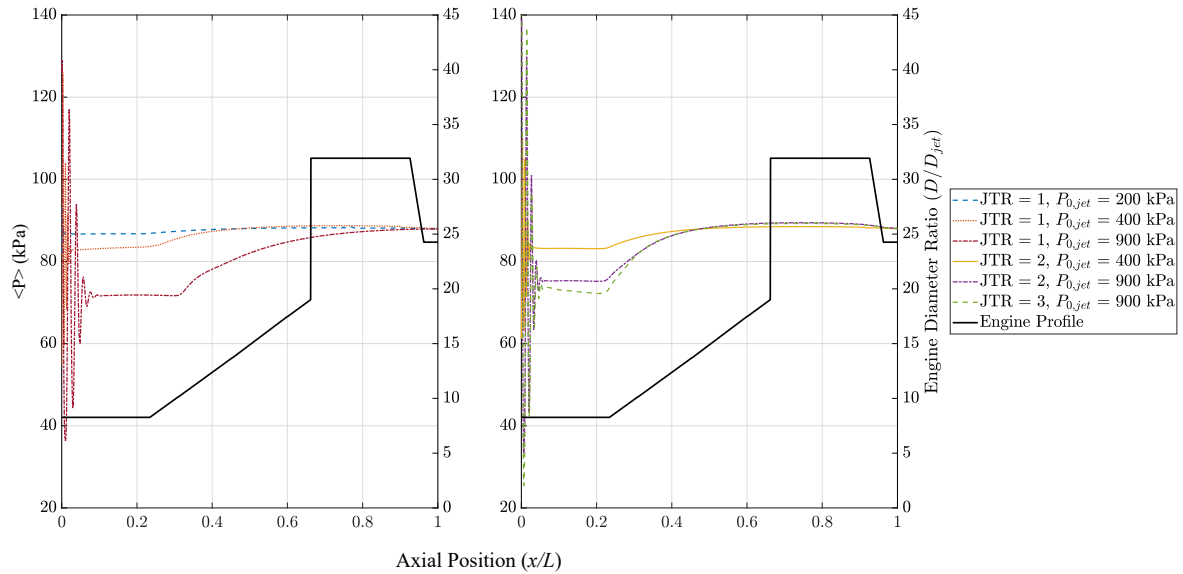


Figure B.2: Average pressure along centerline of the ejector ramjet for various jet stagnation temperatures and pressures.

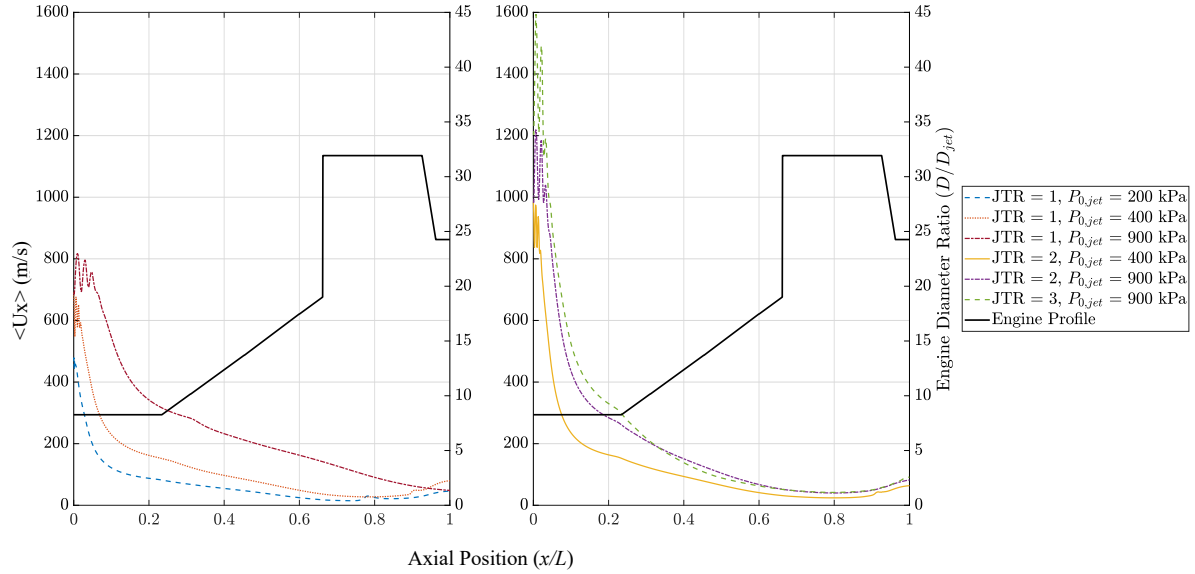


Figure B.3: Average axial velocity along centerline of the ejector ramjet for various jet stagnation temperatures and pressures.

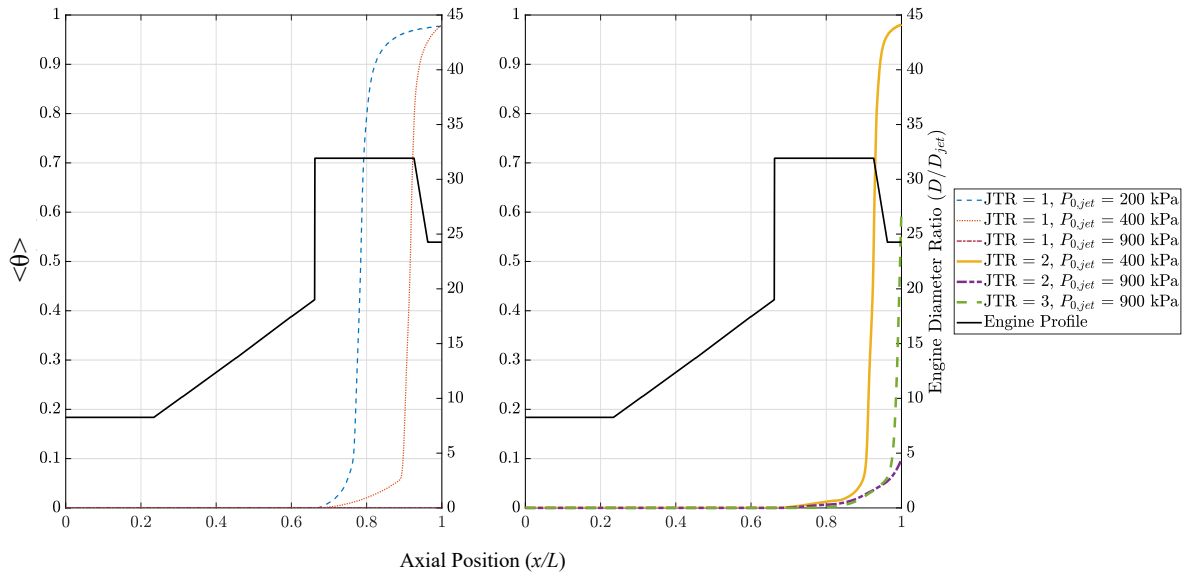


Figure B.4: Average progress variable along centerline of the ejector ramjet for various jet stagnation temperatures and pressures.

## Appendix C

# Mass Flow Rates of Methane and Air for an Ejector Ramjet at Various Operating Conditions

Table C.1 shows the mass flow of the fuel jet (methane) and air into the ejector ramjet for various fuel jet stagnation temperatures and pressures. For the 400 kPa stagnation pressure case with no fuel preheating (i.e. stagnation temperature of 293 K), only the results using the modified chemical timescale (defined in Eq. 3.78) are shown.

Table C.1: Comparison of global equivalence ratio ( $\phi$ ), mass flow of methane ( $\dot{m}_{jet}$ ), mass flow of air ( $\dot{m}_{air}$ ), and entrainment ratio ( $\omega$ ) for an ejector ramjet when some of the heat from combustion is used to preheat the fuel jet. The non-preheated case used a fuel jet stagnation temperature of 293 K, while the preheated cases had stagnation temperatures of 586 and 879 K.

$T_{o,jet}$	$P_{o,jet}$	$\phi$	$\dot{m}_{jet}$ (g/s)	$\dot{m}_{air}$ (g/s)	$\omega$
293 K	400 kPa	0.88	12.1	227.4	18.8
	900 kPa	1.23	27.2	358.9	13.2
586 K	400 kPa	0.65	8.3	212.7	25.6
	900 kPa	0.97	18.7	322.6	17.3
879 K	400 kPa	-	-	-	-
	900 kPa	0.76	15.0	327.6	21.8